Fabrication and optical simulation of periodic nanostructures and their applications

Jia Liu

N° d'ordre NNT : 2016LYSEI027

THESE de DOCTORAT DE L'UNIVERSITE DE LYON

opérée au sein de

l'INSA LYON

Ecole Doctorale ED 160

Électronique, Électrotechnique et Automatique

Spécialité de doctorat: Numerical Simulation and Nanostructure Fabrication

Discipline: Électronique, micro et nanoélectronique, optique et laser

Soutenue publiquement le 31/03/2016, par :

Jia LIU

Fabrication and Optical Simulation of Periodic Nanostructures and their Applications

---

Devant le jury composé de :

LERONDEL Gilles	Professeur (UTT)	Rapporteur
GRANET Gérard	Professeur (UBP)	Rapporteur
SEASSAL Christian	Directeur de recherche CNRS	Examinateur
BESACIER Maxime	Maître de conférences (Polytech Grenoble)	Examinateur
OROBTCHOUK Régis	Maître de conférences HDR (INSA)	Directeur de Thèse

Département FEDORA – INSA Lyon - Ecoles Doctorales – Quinquennal 2016-2020

SIGLE	ECOLE DOCTORALE	NOM ET COORDONNEES DU RESPONSABLE
CHIMIE	**CHIMIE DE LYON** **http://www.edchimie-lyon.fr** Sec : Renée EL MELHEM Bat Blaise Pascal 3e etage secretariat@edchimie-lyon.fr Insa : R. GOURDON	M. Stéphane DANIELE Institut de Recherches sur la Catalyse et l'Environnement de Lyon IRCELYON-UMR 5256 Équipe CDFA 2 avenue Albert Einstein 69626 Villeurbanne cedex directeur@edchimie-lyon.fr
E.E.A.	**ELECTRONIQUE, ELECTROTECHNIQUE, AUTOMATIQUE** **http://edeea.ec-lyon.fr** Sec : M.C. HAVGOUDOUKIAN Ecole-Doctorale.eea@ec-lyon.fr	M. Gérard SCORLETTI Ecole Centrale de Lyon 36 avenue Guy de Collongue 69134 ECULLY Tél : 04.72.18 60.97 Fax : 04 78 43 37 17 Gerard.scorletti@ec-lyon.fr
E2M2	**EVOLUTION, ECOSYSTEME, MICROBIOLOGIE, MODELISATION** **http://e2m2.universite-lyon.fr** Sec : Safia AIT CHALAL Bat Darwin - UCB Lyon 1 04.72.43.28.91 Insa : H. CHARLES Safia.ait-chalal@univ-lyon1.fr	Mme Gudrun BORNETTE CNRS UMR 5023 LEHNA Université Claude Bernard Lyon 1 Bât Forel 43 bd du 11 novembre 1918 69622 VILLEURBANNE Cédex Tél : 06.07.53.89.13 e2m2@ univ-lyon1.fr
EDISS	**INTERDISCIPLINAIRE SCIENCES-SANTE** **http://www.ediss-lyon.fr** Sec : Safia AIT CHALAL Hôpital Louis Pradel - Bron 04 72 68 49 09 Insa : M. LAGARDE Safia.ait-chalal@univ-lyon1.fr	Mme Emmanuelle CANET-SOULAS INSERM U1060, CarMeN lab, Univ. Lyon 1 Bâtiment IMBL 11 avenue Jean Capelle INSA de Lyon 696621 Villeurbanne Tél : 04.72.68.49.09 Fax :04 72 68 49 16 Emmanuelle.canet@univ-lyon1.fr
INFOMATHS	**INFORMATIQUE ET MATHEMATIQUES** **http://infomaths.univ-lyon1.fr** Sec :Renée EL MELHEM Bat Blaise Pascal 3e etage infomaths@univ-lyon1.fr	Mme Sylvie CALABRETTO LIRIS – INSA de Lyon Bat Blaise Pascal 7 avenue Jean Capelle 69622 VILLEURBANNE Cedex Tél : 04.72. 43. 80. 46 Fax 04 72 43 16 87 Sylvie.calabretto@insa-lyon.fr
Matériaux	**MATERIAUX DE LYON** **http://ed34.universite-lyon.fr** Sec : M. LABOUNE PM : 71.70 –Fax : 87.12 Bat. Saint Exupéry Ed.materiaux@insa-lyon.fr	M. Jean-Yves BUFFIERE INSA de Lyon MATEIS Bâtiment Saint Exupéry 7 avenue Jean Capelle 69621 VILLEURBANNE Cedex Tél : 04.72.43 71.70 Fax 04 72 43 85 28 Ed.materiaux@insa-lyon.fr
MEGA	**MECANIQUE, ENERGETIQUE, GENIE CIVIL, ACOUSTIQUE** **http://mega.universite-lyon.fr** Sec : M. LABOUNE PM : 71.70 –Fax : 87.12 Bat. Saint Exupéry mega@insa-lyon.fr	M. Philippe BOISSE INSA de Lyon Laboratoire LAMCOS Bâtiment Jacquard 25 bis avenue Jean Capelle 69621 VILLEURBANNE Cedex Tél : 04.72 .43.71.70 Fax : 04 72 43 72 37 Philippe.boisse@insa-lyon.fr
ScSo	**ScSo*** **http://recherche.univ-lyon2.fr/scso/** Sec : Viviane POLSINELLI Brigitte DUBOIS Insa : J.Y. TOUSSAINT viviane.polsinelli@univ-lyon2.fr	Mme Isabelle VON BUELTZINGLOEWEN Université Lyon 2 86 rue Pasteur 69365 LYON Cedex 07 Tél : 04.78.77.23.86 Fax : 04.37.28.04.48

*ScSo : Histoire, Géographie, Aménagement, Urbanisme, Archéologie, Science politique, Sociologie, Anthropologie

Dedication

To mum, dad and Lili

Acknowledgements

Doing a thesis has been an enormous fruitful journey for me, without the support and encouragement of many people it would have been fruitless. First and foremost, I would like to thank my thesis adviser, Prof. Régis Orobtchouk, for having provided me the opportunity to accomplish my thesis in INL lab. Over these years, his wisdom enlightened my research road. I also would like to thank Prof. Gilles Lerondel, Prof. Gérard Granet, Prof. Christian Seassal, and Prof. Maxime Besacier for devoting their time to serving as my thesis jury.

A sincere acknowledgment has to be given to our local "Photonics in Photovoltaic" team: Prof. Christian Seassal, Prof. Emmanuel Drouard, Prof. Alain Fave, Prof. Fabien Mandorlo, Prof. Hai Son Nguyen, Dr. Loic Lalouat, Dr. Thierry Deschamps, He Ding, Romain Champory, Harouri Abdelmounaim, and Ngoc-vu Hoang. In such a diverse background team, every discussion has been interesting and inspiring. I would like to thank Christian for being supportive when I was confused and frustrated. Also, I would like to thank Emmanuel and Loic for our fruitful discussions and for the hours they spent correcting my paper. I am grateful to Abdou for the hours that we spent inside the clean room and for the coffee outside the clean room.

I would like to thank Prof. Pascal Kleimann and Xichen Yuan for the experimental help and discussions with electrochemical etching and preconcentration chip. I would also like to thank Cécile Jamois for showing me different techniques and proofreading my paper. Besides that I have received great help from our experimental platform (Jean-Louis Leclercq, Joëlle Grégoire and Khaled Ayadi), thanks for providing me the safe and ordered experimental room.

Besides that, I would like to thank all the colleagues and friends, with whom I have

more overlapping on the lab life side. I thank my office mates, Mouhannad, Anton, and Abdul Salam. The office atmosphere was great. I also thank other colleagues with whom I spent time either on the stairs in front of our lab or around the dining table. I, therefore, thank Xuan, Lin, Romain (all of them), Aurélien, Laurent, Mohamed, Daniel, Yao, Stéphanie, and Corina. I enjoyed the time we spent together.

I'd also like to thank all of my other friends outside the lab, thanks for their continuous support and accompany through these years. Special thanks to my former roommate Carlos. Thanks for patiently helping me adapting the new life here in the first year.

On the domestic side, I thank my family for always believing in me and letting me move half a planet away from home without protest. Last and most importantly, I would like to thank Lili for always standing by me with endless love.

Jia LIU

Lyon, France

Abstract

Periodic nanostructures play an important role in the domain of nanotechnology, especially in photon control. While there exist many general purpose techniques for fabrication and optical simulation, we show tailored fabrication and optical simulation methods for periodic structures to accelerate lab-scale prototyping and optical design. In the first part of this dissertation, we describe a low-cost lithographic technique named Laser Interference Lithography (LIL) for fabricating periodic nanostructures. LIL technique is combined with dry-etching, wet-etching and electrochemical etching technique to realize, respectively, cylindrical holes, inverted pyramids and high aspect ratio pore arrays on silicon based substrate. The one-dimensional patterns on glass substrates are also used as nanofilters in realizing low-cost preconcentration chip. In the second part, we first describe Rigorous Coupled-Wave Analysis (RCWA), a rigorous electromagnetic calculation method designed for periodic structures. A detailed derivation is given to explain the numerical method. Then, we combine the RCWA method and a new proposed pseudo-disordered patterns design approach to investigate photon control. As an example, we demonstrate that by adding 'appropriate' engineered fine stripes to each long period the absorption performance of thin silicon slab can be largely enhanced.

Résumé en Français

1. Introduction

La compréhension et la manipulation des propriétés des matériaux conduit à l'évolution de notre civilisation. Il y a quelques centaines d'années, nous avons commencé à construire des matériaux artificiels, tels que la céramique et les matières plastiques avec de nouvelles propriétés extraordinaires. Au siècle dernier, nous avons ouvert l'âge des nanomatériaux. Au cours des dernières décennies, la nanotechnologie a façonnée notre monde énormément. En construisant des structures sur des échelles de longueur de 10-100 fois la taille des atomes individuels, les propriétés des matériaux sont significativement différentes de celles de leur état massif. Les nano-structures périodiques jouent un rôle important, car nous devons considérer à la fois le matériel et sa configuration géométrique.

Fabrication de la nanostructure périodique

Les techniques de lithographie optique, lithographie électronique et nanoimpression ont été largement utilisés pour la fabrication d'objets. La lithographie optique est bien établie pour la fabrication de dispositifs circuit intégré. Mais elle est fondamentalement limitée par la diffraction de Rayleigh pour fabriquer des structures jusqu'au nanomètre. La lithographie électronique peut compenser cette limite pour produire des structures très fines, mais elle souffre d'un faible débit. La nanoimpression est une technique rentable dans la production nano-motifs sur une grande surface. Toutefois, elle ne convient pas pour le prototypage rapide à l'échelle du laboratoire lorsque la réalisation d'un masque est nécessaire dans le processus de fabrication. En tant que tel, une technique alternative nommé Laser Interférences Lithographie (LIL) semble être bien adaptée à l'échelle

du laboratoire pour la réalisation rapide à un faible coût de prototypes. LIL est une technique rapide pour réaliser des structures fines sur une grande surface sans système optique complexe. En combinant d'autres techniques de transfert de motifs, on peut fabriquer des structures périodiques qui peuvent être utilisées en nano-fluidique, et surtout pour le contrôle de photons.

Dans le chapitre 2, nous introduisons la technique LIL et son principe de base. Les avantages et les limites concernant notre configuration spécifique utilisant une configuration interférométrique de type miroir de Lloyd sont décrits et détaillés. Les différents types de formes de motifs qui peuvent être fabriqués sont également présentées. En outre, les techniques structurelles de transfert (de gravure humide et de gravure sèche) à partir de la résine photosensible à motifs sur un substrat de silicium sont explorées et donne lieu à l'obtention de motifs cylindrique et en forme de pyramide inversée.

Dans le chapitre 3, nous décrivons les différentes applications des nanostructures périodiques fabriqués par LIL. Dans la première partie, un réseau de silicium poreux avec une période de 300 nm sur des substrats de tailles supérieures au cm^2 est fabriqué par la combinaison de LIL et gravure électrochimique. La fabrication d'un vaste réseau périodique de pores 2D ayant un fort facteur d'aspect, avec 250 nm de diamètre, sur une profondeur de 5 μm est démontrée. Toutes les étapes du procédé ont été optimisées pour réaliser un réseau de pores avec des parois latérales verticales d'épaisseur 50 nm et un rapport d'aspect de 100 sur des substrats de silicium de type n sur une surface de $2 \times 2\,cm^2$. Dans la deuxième partie de ce chapitre, nous discutons des applications de nanostructures périodiques unidimensionnelles. La réalisation d'un dispositif de pré-concentration, qui utilise une structure périodique unidimensionnelle comme filtre nano-fluidique, est discutée. La combinaison des techniques LIL et xurography nous a permis de fabriquer une puce de pré-concentration simple et à faible coût basé sur phénomène de polarisation de concentration d'ions.

Simulation optique de nanostructure périodique

Même si la LIL est une technique relativement rapide pour le prototypage, les méthodes de simulation électromagnétiques rigoureuses sont encore nécessaires pour accélérer le

processus d'optimisation de conception de dispositifs photoniques, ce qui nous amène à la deuxième partie de la thèse : la simulation électromagnétique rigoureuse et l'optimisation de la structure optique. Dans le cadre de la modélisation optique, des méthodes aux différences finies, aux éléments finis, et des techniques utilisant des décompositions en série de Fourier ont été proposées. Compte tenu des caractéristiques physiques sous-jacentes des structures que l'on est capable de réaliser, à savoir la périodicité, nous avons choisi une méthode basée sur la décomposition en série de Fourier pour effectuer les simulations optiques rigoureuses. La méthode choisie nommé « Rigorous Coupled-Wave Analysis » (RCWA) ou «Fourier Modal Method » (FMM) est très efficace pour calculer rigoureusement les performances optiques des structures périodiques. Comparé à d'autres méthodes couramment utilisées comme des différences finies dans le domaine temporel (FDTD) ou la méthode des éléments finis (FEM), elle est beaucoup plus rapide et fournit les mêmes résultats en termes de précision. Pour les deux méthodes FDTD et FEM, les structures simulées doivent être discrétisée dans une grille régulière ou irrégulière pour effectuer le calcul. Le nombre de points de calcul peut être énorme si la structure est grande ou contient des traits fins. Dans le cas de structures multicouches, les autres couches homogènes doivent également être discrétisées, ce qui pose problème lorsque les épaisseurs de couches deviennent relativement grandes. La technique RCWA utilise une décomposition en onde plane qui permet de modéliser avec le même encombrement mémoire les couches homogènes quel que soit leurs épaisseurs et les couches périodiques sont représentées par une décomposition en série de Fourier, qui, dans la plupart des cas, contient très peu de points, notamment pour des motifs avec des profils verticaux. Le plus grand inconvénient de la méthode RCWA est que seules des structures périodiques peuvent être simulées. La simulation d'objets plus complexes nécessite l'emploi de techniques de super-cellule et l'utilisation de conditions absorbantes sur les bords qui nécessite d'utiliser un nombre d'ondes planes plus important et qui par conséquent réduit l'intérêt de cette technique.

Dans le chapitre 4, la méthode RCWA est introduite et les formulations sont présentées en détail. Une comparaison avec la technique FDTD est donnée en fin de chapitre, afin de valider le code développé lors de ce travail de thèse et de vérifier son exactitude.

Dans le chapitre 5, nous introduisons une nouvelle approche pour construire des structures pseudo-désordonnées unidimensionnelles. La méthode nous permet de sélectionner parmi tous les motifs multi-périodiques possibles, ceux qui sont non redondant en termes de propriétés optiques afin de diminuer le temps de calcul et ainsi pouvoir étudier toutes les combinaisons, ce qui permet de déterminer la meilleure structure là ou souvent d'autres techniques de modélisation et de schéma d'optimisation ne permettent d'étudier qu'un nombre limité de combinaisons. Cette technique mise en place durant ce travail de thèse a été utilisée pour concevoir une couche mince de silicium structurée permettant de maximiser son pouvoir absorbant sur une large bande spectrale pour des applications photovoltaïques.

Dans le chapitre 6, nous concluons en soulignant les apports marquants de ce travail de thèse en en discutant des orientations futures possibles que cette recherche peut prendre.

2. Nanostructure Fabrication en Utilisant Laser Interférences Lithographie

Dans cette section, nous allons d'abord donner un bref aperçu de la lithographie LIL. Le transfert structurel des motifs de résine dans le substrat de silicium par gravure sèche et gravure chimique humide sera ensuite discuté. Nous illustrons les avantageuses et les limites de cette technique avec la fabrication de différents types de motifs périodiques.

Laser Interference Lithographie

Généralement, il existe deux types de configuration pour la lithographie LIL, nommées interféromètre de Mach-Zehnder et miroir interférométrique de Lloyd, respectivement. La première technique, utilisant un interféromètre de Mach-Zehnder, est principalement utilisée comme un outil de production pour exposer des substrats de grande surface. Il permet d'utiliser des angles d'incidences différents pour la réalisation de motifs possédant un angle de blaze, mais nécessite un système asservi de recalage des franges d'interférences. Il doit être également placé sur une table anti-vibration. Il est également

sensible au milieu environnant, comme le débit d'air. La technique mise en œuvre lors de ce travail de thèse utilise un montage interférométrique de type miroir de Lloyd. Comme le miroir est solidaire de l'échantillon, même si le montage vibre, les franges restent localisées au même endroit sur l'échantillon à insoler. Le problème de brouillage des franges est ainsi résolu sans ajout de systèmes coûteux. En contrepartie, il n'est pas possible de réaliser des motifs possédant un angle de blaze directement dans la résine. Toutefois, en utilisant une gravure sèche de type RIE (Reactive Ion Etching) sur un substrat incliné lors de l'étape de transfert des motifs, il est possible de réaliser de telles structures.

Miroir Interférométrique de Lloyd

Le système de lithographie utilisant un miroir interférométrique de la Lloyd est composé de trois parties principales : un laser, un filtre spatial et le porte échantillon. Une illustration schématique de la mise en œuvre de ce montage est représentée sur la Fig. 1. Un laser UV Crylas semi-conducteur ($\lambda = 266\ nm$) est utilisé comme source de lumière. Un filtre spatial est placé entre le laser et le miroir de Lloyd. Son rôle est d'une part de supprimer les irrégularités du faisceau laser (speckles) qui créent des variations d'intensités de lumière localement qui dégrade l'homogénéité des motifs et d'autre part de faire diverger suffisamment le faisceau pour obtenir une tache lumineuse éclairant le miroir de Lloyd homogène assimilable à une onde plane. Le porte échantillon est constitué d'une platine de rotation qui permet de modifier l'angle d'incidence et de par conséquent de modifier la période des interférences, d'un miroir rectangulaire d'aluminium de planéité $\lambda/20$ avec un traitement forte réflectivité UV adapté au laser utilisé placer à 90° du support de l'échantillon. La planéité du miroir est importante pour réduire la distorsion des franges d'interférences et la forte réflectivité du miroir permet d'améliorer le contraste des interférences, ce qui permet d'accroitre l'homogénéité des motifs obtenus.

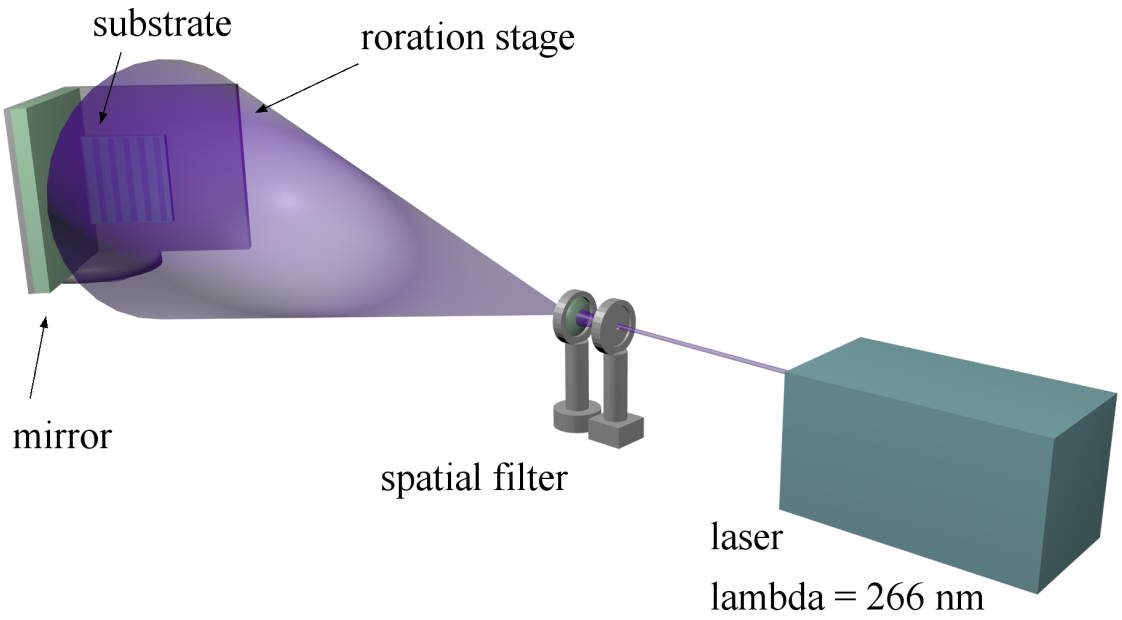

FIGURE 1: Schéma du montage utilisé pour la lithographie interférométrique laser.

Procédé de lithographie LIL

Des substrats de silicium avec une couche de silice de 100 nm sont principalement utilisé dans le processus de lithographie LIL. La couche de silice est déposée sur le substrat de silicium par un procédé PECVD (Plasma Enhanced Chemical Vapor Deposition) et présente deux intérêts majeurs pour les dispositifs que l'on cherche à réaliser. D'une part, la partie réelle de son indice de réfraction à la longueur d'onde d'insolation ($\lambda = 266\ nm$) est proche de celui de la résine, ce qui permet d'obtenir un coefficient de réflexion à l'interface résine/silice quasiment nul. D'autre part, la silice PECVD est absorbante dans cette gamme de longueur d'onde et l'épaisseur de 100 nm suffit pour absorber la totalité de la lumière transmise. Cette couche de silice nous permet d'éliminer le phénomène d'ondes stationnaires à l'origine d'un réseau parasite dans l'épaisseur de résine et ainsi d'améliorer l'uniformité des motifs. Elle joue le même rôle qu'une couche BARC (Back Anti Reflection Coating) dans les procédés de lithographie avancée de la micro-électronique. Le second intérêt est que cette couche de silice sert de masque dur pour le transfert des motifs dans le substrat de silicium. En général, il comprend quatre étapes, à savoir, le nettoyage des substrats, le dépôt à la tournette de la résine

photosensible, l'exposition de la résine, et le développement.

- La première étape est le nettoyage du substrat. L'échantillon est successivement immergé dans de l'acétone, de l'éthanol et de l'eau désionisée (eau DI) pour éliminer la contamination de surface. L'ensemble du processus est exécuté dans un bain à ultrasons, et chaque étape dure 10 minutes.

- Par la suite, le film de polymère de résine photosensible est déposé sur le substrat en utilisant une technique de revêtement par centrifugation pour former un film mince uniforme sur l'échantillon.

- L'exposition se fait en utilisant le montage LIL. Les réseaux unidimensionnels sont obtenus par simple exposition de la résine sensible alors que les réseaux 2D nécessitent une double exposition en tournant l'échantillon de 90° entre les deux expositions. La résine à hautes résolution utilisée est une résine négative à amplification chimique (NEB 22) qui requiert une étape supplémentaire nommée « Post-Exposure Bake » (PEB) doit être effectué après le processus d'exposition.

- Le processus de lithographie se termine par le développement dans une solution basique (MF 702) et un recuit thermique sur plaque chauffante à 110 °C qui permet de durcir la résine et d'améliorer sa résistance aux étapes de gravure suivantes utilisées pour transférer le motif dans le substrat.

La figure 2 montre des images MEB de trois types d'échantillons. Un réseau de traits unidimensionnels, et de réseaux de trous bidimensionnels de diamètres différents. L'évolution du facteur d'aspect des motifs en fonction de la dose d'exposition a fait l'objet d'une étude particulière afin d'obtenir les motifs désirés en fin de procédé suivant l'application visée. Ce point sera détaillé dans les paragraphes suivants.

Transfert des structures

Pour que les motifs soient utilisables, il faut les transférer dans le substrat. Dans cette partie, nous décrivons deux procédés de gravure anisotropes. Le premier est un processus de gravure sèche ionique réactive (RIE pour Reactive Ion Etching). C'est une

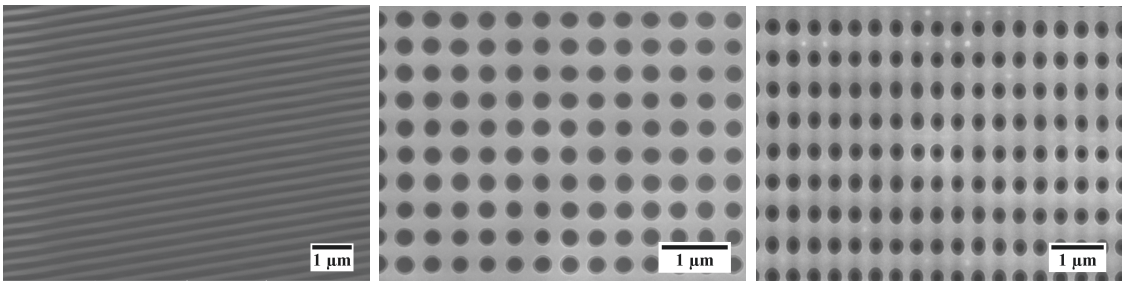

(a) (b) (c)

FIGURE 2: Images MEB d'échantillons fabriqués. (a) Exposition unique. (b) Double exposition avec la même période. (c) Double exposition avec une période et un facteur d'aspect différents.

des techniques les plus couramment utilisée dans l'industrie des semi-conducteurs. En choisissant différents réactifs gazeux de gravure, le procédé RIE permet de transférer des motifs à des échelles nanométriques de façon anisotrope quel que soit l'orientation cristalline du substrat, et donc de conserver une haute résolution. La seconde technique est un procédé de gravure humide. L'hydroxyde de potassium (KOH) ou l'hydroxyde de tétraméthylammonium (TMAH) en tant que solution est utilisée ici. La combinaison de cette technique de gravure avec la lithographie LIL, nous a permis de réaliser des réseaux de pyramides inversées de différentes périodes sur des substrats de relativement grande échelle. Contrairement à la gravure RIE, les gravures KOH ou TMAH sont fortement dépendantes de l'orientation cristalline.

Une recette de gravure avec le mélange de gaz de $CHF_3/SF_6/O_2$ a été optimisée pour réduire la rugosité de surface. La figure 3 montre les résultats de la gravure optimisée. Un mélange approprié de $CHF_3/SF_6/O_2$ (@8/4/12) nous donne une grande homogénéité avec des profils isotropes.

La gravure humide utilise des produits chimiques liquides pour enlever sélectivement une partie du matériau sur le substrat. Les vitesses de gravures dépendent fortement de l'orientation cristalline et modifie fortement l'aspect et la forme du motif initial obtenu après l'étape de lithographie optique. La figure 4 montre des images MEB de pyramides inversées avec différentes périodes pouvant variées de 300 à 600 nm, ce qui démontre clairement la stabilité et la flexibilité du procédé mis au point. Cependant, les temps de gravure utilisés pour la formation complète des pyramides varient fortement avec la

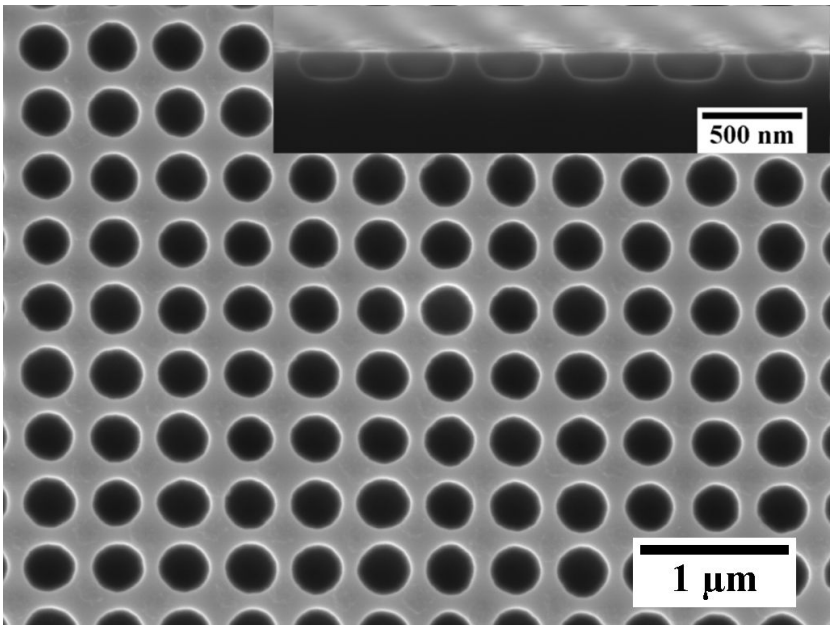

FIGURE 3: Image MEB d'un réseau 2D de cylindres gravés dans un substrat de silicium en vue de dessus et de profil.

période. Les motifs étant plus petits pour les courtes périodes, il semblerait logique de réduire le temps de gravure lorsqu'on diminue la période des motifs. Expérimentalement, un temps de 180 s permet d'obtenir des pyramides complètes sur la totalité de l'échantillon pour des périodes de 600 nm, alors qu'il est de 360 s pour des périodes de 300 nm. Ce comportement inverse peut s'expliquer par le fait que le liquide a du mal à pénétrer et à se renouveler dans les trous de petites dimensions, ce qui ralentit la formation des pyramides même en présence d'ultrason. Le diamètre des trous de 150 nm pour une période de 300 nm est du même ordre de grandeur que la hauteur de silice de 100 nm utilisé comme masque dur. Les doses d'insolation ont été diminuées pour augmenter la taille des trous dans un premier temps de manière à favoriser la pénétration du liquide et ainsi améliorer l'uniformité des motifs. Le problème de cette solution est que le masque de devient fin sur les bords et le phénomène de sous gravure du silicium font que le masque se décolle du substrat de silicium avant la formation complète des pyramides inversées. La deuxième solution envisagée a été de réduire la taille des trous en augmentant la dose d'insolation de manière à accroitre la résistance du masque à la gravure. On a pu ainsi réalisé des trous de diamètres de 100 nm pour des périodes de 300 nm qui résiste à une attaque de KOH ou de TMAH d'une durée de 480 s, ce qui

est largement suffisant pour obtenir des pyramides inversées de tailles homogènes sur la totalité d'un substrat de 2 cm^2.

On peut constater sur la figure 4 que l'anisotropie de la gravure humide a transformé les trous ronds du masque de silice en un réseau carré de 250 nm de côté pour une période de 300 nm. Le phénomène de sous-gravure fait que les pyrmides deviennent pratiquemen jointives.

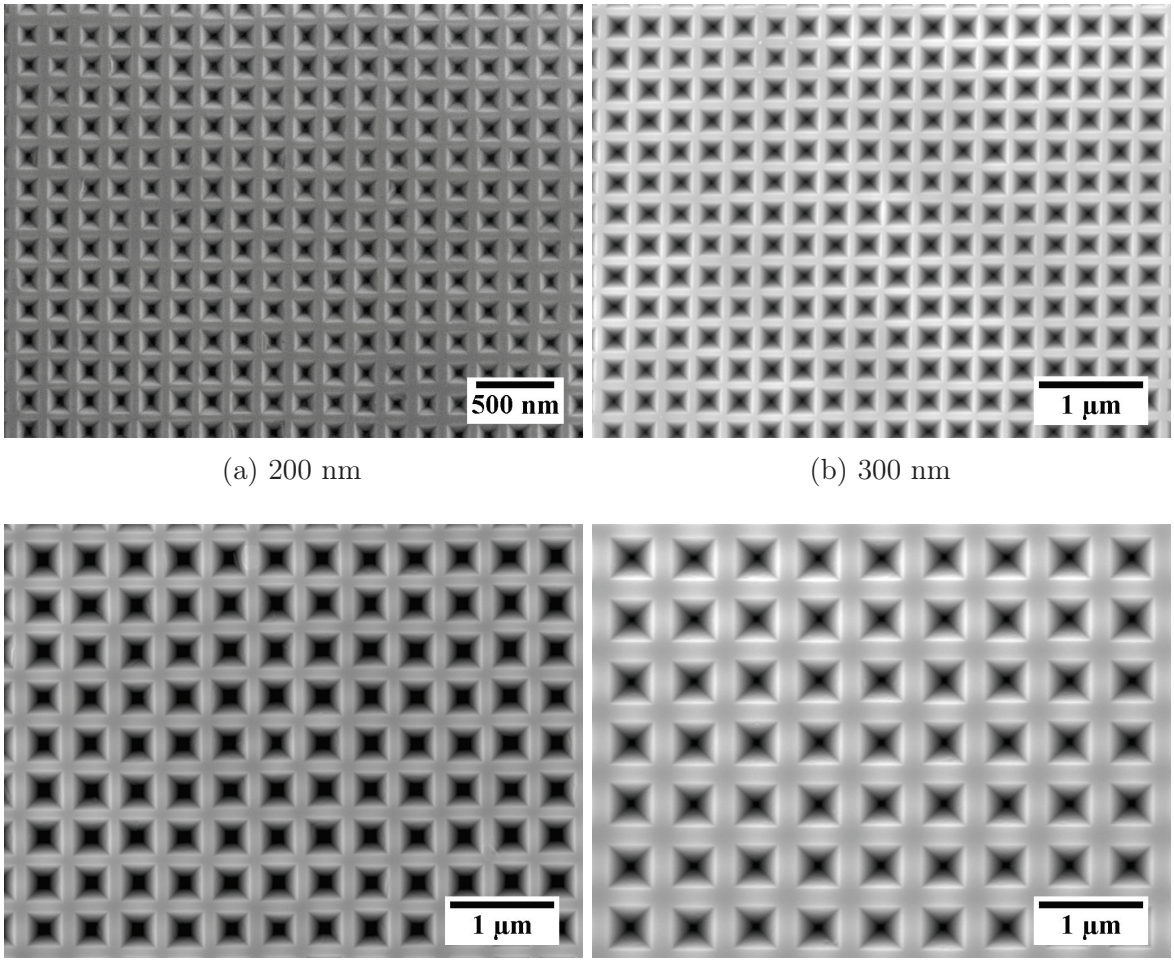

(a) 200 nm (b) 300 nm

(c) 450 nm (d) 600 nm

FIGURE 4: Image MEB des pyramides inversées gravées avec des périodes différentes. (a) 200 nm. (b) 300 nm. (c) 450 nm. (d) 600 nm.

3. Applications de nanostructures périodiques

Le savoir-faire développé dans le chapitre précédent a été utilisé pour la réalisation de dispositifs fluidiques pour de la pré-concentration. Ce travail a fait l'objet d'une collaboration avec Pascal Kleimann de l'équipe Microfluidique et Microsystèmes de l'INL. Deux types de dispositifs ont été réalisés. Un réseau de nano-canaux cylindriques obtenus par gravure électro-chimique du silicium au HF et un réseau de traits unidimensionnels obtenu par gravure RIE d'un substrat de verre.

Fabrication de nano-canaux cylindriques

Des réseaux 2D de pyramides inversées de période 300 nm ont été réalisés sur des substrats de silicium dopés n possédant une résistivité adaptée à la réalisation de pores de 250 nm par gravure électrolytique au HF. La pyramide inversée est un motif particulièrement adapté à ce type de gravure parce qu'il permet d'obtenir un effet de pointe au bout de la pyramide afin de localiser les porteurs à cette endroit et privilégie la gravure au bout de la pointe. L'homogénéité des motifs est primordiale pour préserver les lignes de champs identiques et maintenir une gravure verticale des canaux au bout de la pointe. La combinaison de la lithographie LIL avec les techniques de gravures permet la formation très homogène de pores sub-micrométriques de faibles périodicités de 300 nm et de profondeurs élevées de 5 µm. Toutes les étapes du procédé ont été optimisées pour réaliser les parois latérales verticales d'une épaisseur de 50 nm, ce qui représente un rapport d'aspect de 100 sur des substrats de silicium de type n de $2 \times 2\,\mathrm{cm}^2$. Ces résultats constituent l'état de l'art dans ce domaine de fabrication.

Procédure de fabrication

La procédure de fabrication est illustré schématiquement sur la Fig. 5 et consiste en quatre étapes principales : la lithographie LIL, le transfert des motifs dans un masque de silice par gravure RIE, la formation des nano-pyramides par gravure humide KOH, et la gravure électrochimique. Le paramètre clé qui domine toute l'optimisation des processus est l'uniformité : une grande uniformité des pyramides inversées est absolument crucial pour une gravure réussie des réseaux de pores par gravure électrochimique, ce qui signifie

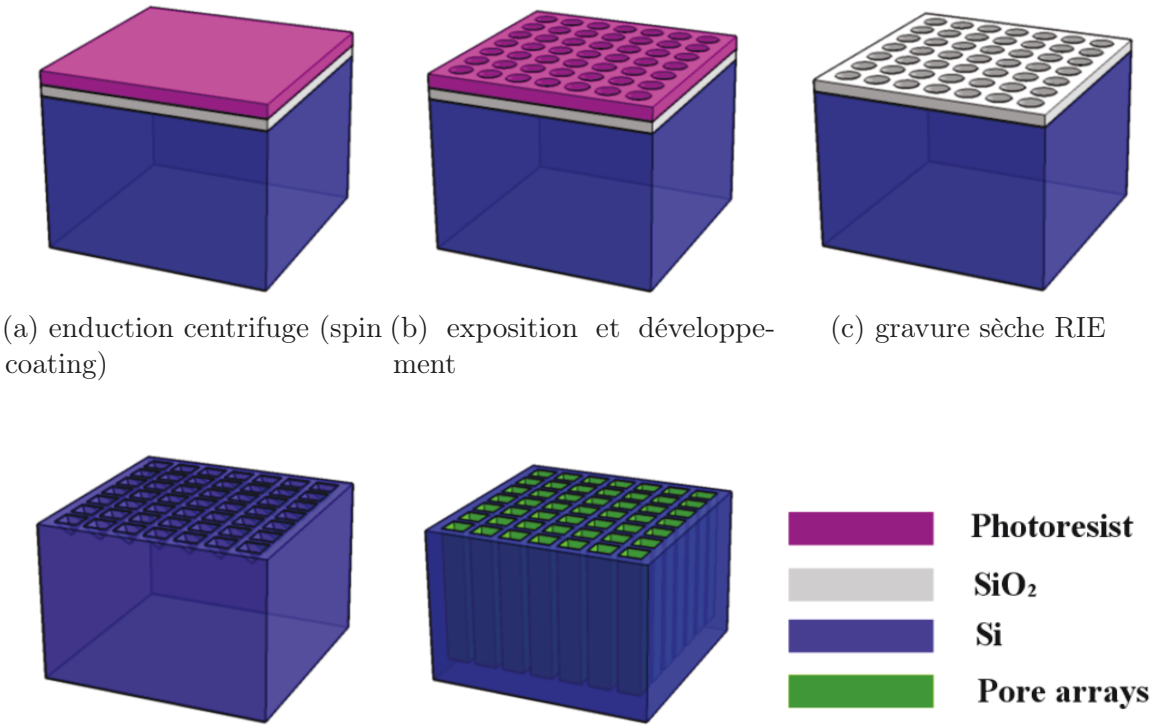

(a) enduction centrifuge (spin coating) (b) exposition et développement (c) gravure sèche RIE

(d) gravure humide KOH (e) gravure électrochimique HF

FIGURE 5: Image schématique du procédé de fabrication de canaux cylindriques : (a) Enduction d'une couche de résine photosensible négative sur l'échantillon. (b) Double exposition LIL et développement. (c) Transfert des motifs dans le masque dur de SiO_2 par gravure sèche RIE avec un mélange gazeux de CHF_3/Ar. (d) Formation des pyramides inversées par gravure humide KOH. (e) Formation du réseau de pores par gravure électrochimique HF du silicium de type n.

que les étapes de procédé précédentes ont été soigneusement et de manière interactive optimisées afin d'obtenir les trous les plus uniformes et plus petite possible dans le masque de silice.

Les images MEB correspondantes de chaque étape de fabrication sont illustrées sur la Fig. 6. Comme nous pouvons le voir, grâce à l'ensemble du processus avant gravure électrochimique l'uniformité des structures montrent peu de variation, ce qui garantit le succès et l'uniformité de gravure électrochimique comme illustré sur la Fig. 6d.

Il est important de souligner que la période de 300 nm démontré ici n'est probablement pas une limite réelle. Cependant, comme l'a souligné dans le document, une nouvelle réduction de la période et le diamètre des pores exigerait la ré-optimisation de toutes les étapes du procédé. En particulier, la composition de l'électrolyte est cruciale pour

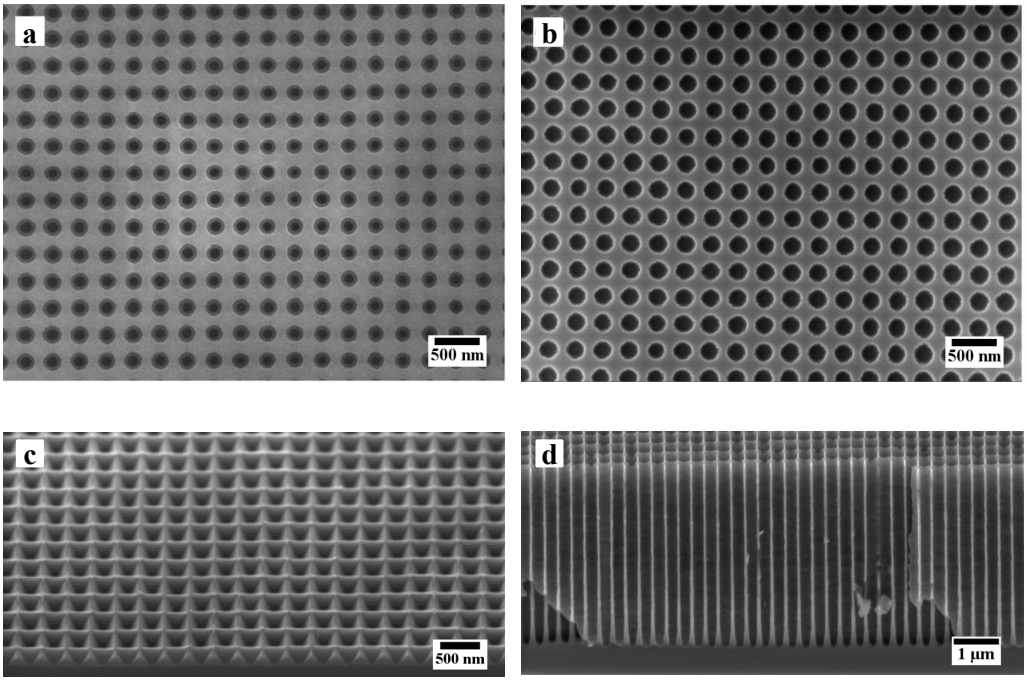

FIGURE 6: Image MEB de la résine photosensible négative développée avec une période de 300 nm. (b) Image MEB de masque dur de SiO_2. (c) Image MEB de pyramides inversées. (d) Image MEB en coupe transversale du réseau de pores.

limiter la dissolution électrochimique au bout des pores. La résistivité du substrat doit être modifiée pour réduire le diamètre des pores. Des études préliminaires indiquent que l'addition d'un tensioactif cationique tel que le chlorure de cétyltriméthylammonium aide à réduire encore le diamètre des pores.

Dispositif de préconcentration unidimensionnel

Dans cette section, nous explorons l'utilisation de structure unidimensionnelle en micro- et nano- fluidique. Ici, nous introduisons une puce simple et à faible coût basé sur le phénomène d'« Ion Concentration Polarization » (ICP). La puce de préconcentration se compose de deux microcanaux pontés par un certain nombre de nanocanaux agissant comme un filtre nanofluidique robuste. Les nanocanaux et microcanaux sont fabriqués séparément par lithographie LIL et xurography. En intégrant ces deux techniques économiques un facteur de préconcentration de 1,600 à 8 minutes a été obtenu.

Fabrication des Puces

La figure 7 illustre schématiquement la puce réalisée. La première couche et la troisième couche sont faites à partir de lames de verre et la couche intermédiaire est constituée d'un film auto-adhésif double face. La lithographie LIL a été employée pour graver des nanocanaux sur l'une des deux lames de verre. La xurography a été utilisée pour découper le modèle pré-conçu sur le film adhésif. La combinaison de deux techniques permet de fabriquer l'appareil à très faible coût.

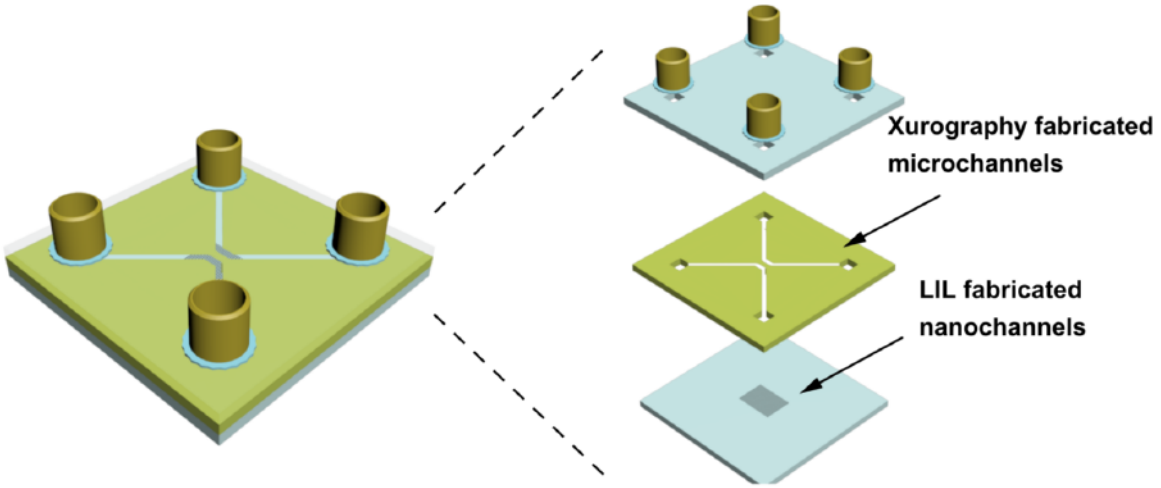

FIGURE 7: Schéma de la puce de préconcentration.

Dans le processus LIL, un substrat de verre (25 mm × 25 mm × 1 mm, Duscher, France) a été exposé à deux reprises pour réaliser les nanocanaux localisées. La plaque de verre est placée sur le porte échantillon du montage LIL et les réseaux unidimensionnels sont exposés sur la totalité de la plaque de verre. La localisation est obtenue grâce à une seconde exposition au travers d'un masque de plastique qui sert à protéger la partie centrale de la plaque de verre. Comme une résine négative a été utilisé, les nanocanaux sont fabriqués uniquement au centre de la plaque de verre par gravure RIE. L'échantillon préparé montre une grande homogénéité, ce qui garantit le succès de processus de pré-concentration (Fig. 8).

Dans le processus xurography, un traceur robotisée a été utilisé pour découper les motifs définis par l'utilisateur dans un film auto-adhésif double face de 110 µm d'épaisseur. La largeur des microcanaux a été fixée à 600 µm. Les deux lames de verre

(a) sur le résine photosensible

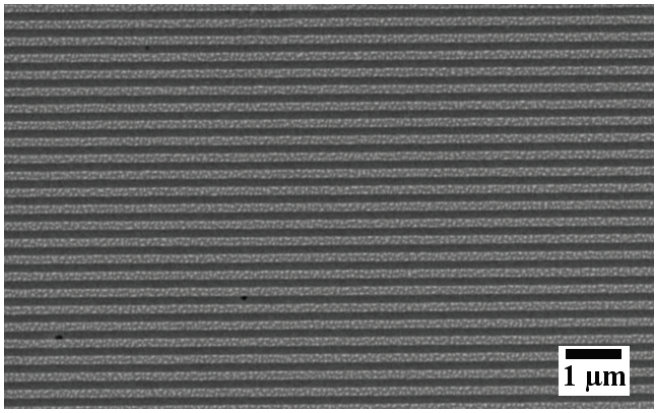

(b) sur le substrat en verre

FIGURE 8: Image MEB des nanocanaux fabriqués (a) sur le résine photosensible, (b) sur le substrat en verre.

et le film double face adhésif sont assemblés en utilisant une machine de presse à 7 bar. Quatre NanoPorts utilisés comme réservoirs ont été alignées et collées sur les quatre trous percés sur le dessus de la lame de verre. La puce de concentration a été finalisée en plaçant quatre fils de platine comme électrodes dans les quatre réservoirs fluidiques. La figure 9 montre le dispositif final.

Résultats et Discussion

La figure 10 montre la performance du dispositif de pré-concentration pour un temps de 400 s. Comme nous pouvons le voir, la fluorescéine se concentre sur les deux côtés du côté haut potentiel microcanaux. La figure 10b montre le processus d'accumulation de la fluorescéine dans le temps sur la branche droite du côté fort potentiel des microcanaux. Au

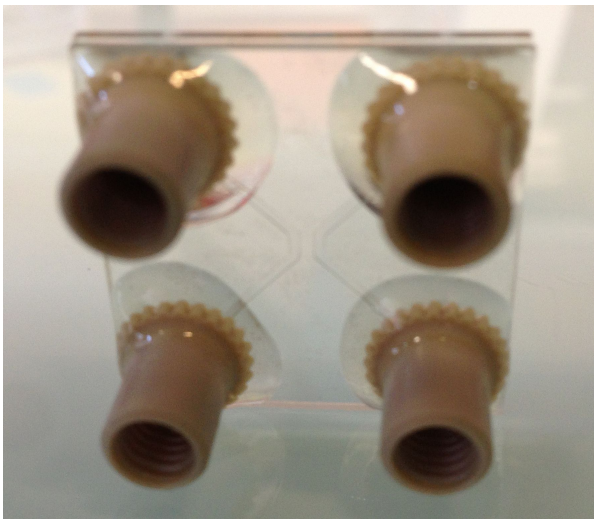

FIGURE 9: Image de la puce de préconcentrateur fabriqué.

cours du temps, la fluorescéine est de plus en plus piégée jusqu'à ce qu'un équilibre entre la diffusion et l'accumulation soit atteint. Enfin, le coefficient global de préconcentration atteint une valeur maximale de 1600 pour un temps de 400 s.

Résumé

Dans ce travail, nous avons développé, un prototypage préconcentration de biomolécules rapide, simple et à faible coût en combinant les procédés LIL et xurography. La préconcentration est limitée par le fait que l'adhésif double face utilisé bouche partiellement les nano-canaux et ne permet d'utiliser des motifs plus petits facilement réalisables par la technique LIL. Malgré ses limites dans la résolution, notre dispositif pourrait être attrayant pour la fabrication de la puce biomolécules préconcentration faible coût. En outre, par l'amélioration de la technique de liaison, les performances du dispositif pourrait être encore améliorée pour atteindre des niveaux de préconcentration record. Quoi qu'il en soit, cette étude a permis pour la première fois au laboratoire de fabriquer des motifs périodiques localisés par la technique LIL.

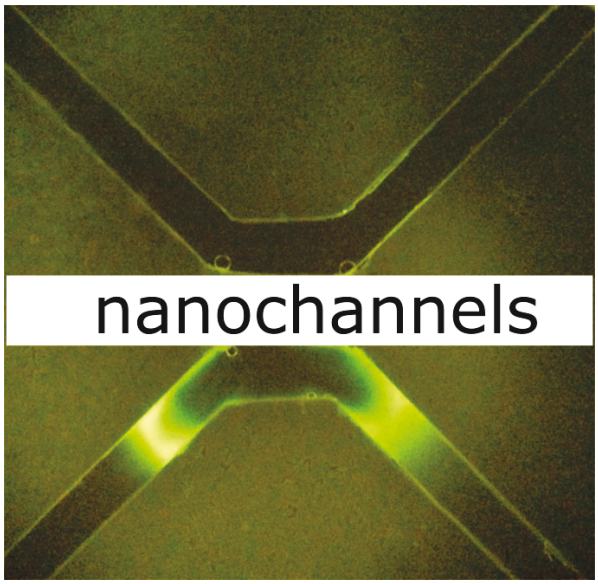

(a)

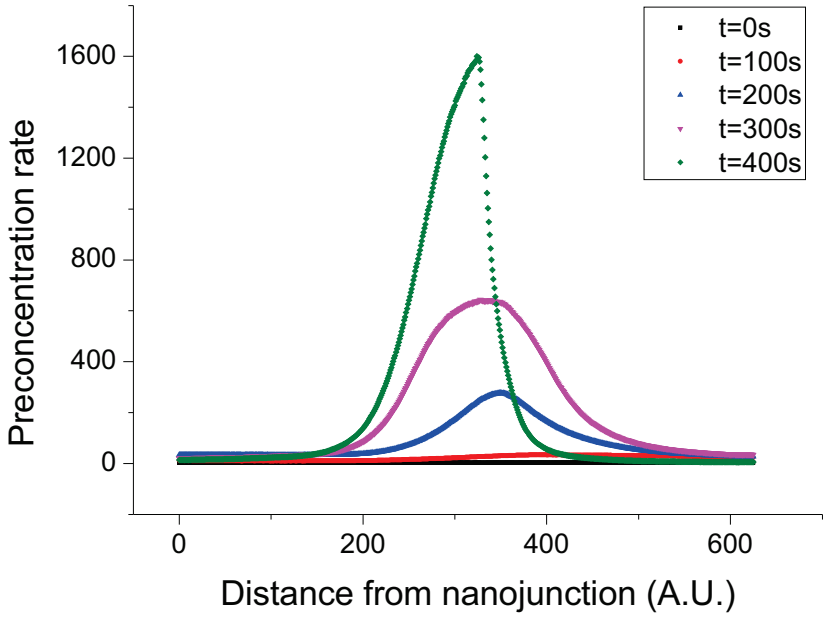

(b)

FIGURE 10: Résultat expérimental du dispositif de pré-concentration.(a) Image de la fluorescéine piégés à 400 s. (b) La performance du dispositif de pré-concentration pour un temps de 400 s

4. Etude des propriétés optique des structures périodiques par RCWA (Rigorous Coupled Wave Analysis)

Dans cette section, nous considérons les propriétés optiques des structures périodiques. Auparavant, nous avons décrit leurs procédés de fabrication. Les méthodes numériques

sont encore nécessaires pour étudier leurs propriétés optiques et ainsi fixer la géométrie des dispositifs en fonction des applications visées. Dans cette partie, une méthode électromagnétique rigoureuse adaptée au calcul sur des structures périodiques est introduite.

Rigorous Coupled Wave Analysis

L'idée de base de la méthode RCWA (Rigorous Coupled wave Analysis) est de calculer le champ électromagnétique dans chaque couche dans l'espace réciproque représenté par une somme d'harmoniques spatiales. Cela transforme l'équation d'onde en un ensemble d'équations différentielles ordinaires qui est ensuite résolu comme un problème de valeurs et vecteurs propres. Les valeurs et vecteurs propres sont représentatifs respectivement de la constante de propagation et l'amplitude des ondes planes diffractées dans chaque couche modulée. Les amplitudes des ondes planes dans les milieux homogènes du dispositif sont obtenues en utilisant les propriétés de continuités des composantes tangentielles du champ électromagnétique aux interfaces entre les différents milieux. Un exemple de dispositif sur lequel sont réalisés les calculs est schématisé sur la figure 11.

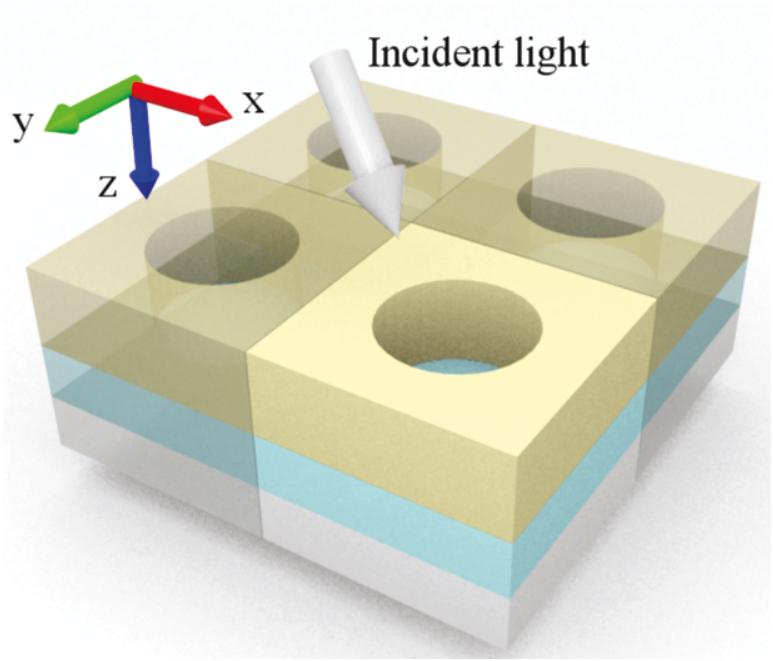

FIGURE 11: Schéma d'un empilement d'une structure périodique bidimensionnelle simulé par RCWA.

La méthode RCWA est une méthode semi-analytique où l'équation d'onde est traitée

analytiquement dans la direction longitudinale. Dans le cas de profils droits invariant suivant la direction z, comme illustré sur la figure 11, cette méthode peut modéliser des structures de longueur arbitraire sans augmenter le temps de simulation. Les dispositifs de formes arbitraires, comme par exemple les pyramides inversées, sont traitées en utilisant une discrétisation suivant z en marche d'escalier, ce qui nécessite d'ajouter un nombre important de couches minces et par conséquent augmente le temps de calcul.

Scattering Matrix

Pour décrire la propagation des ondes planes dans les différents milieux homogènes ou modulés dans le dispositif, deux approches, à savoir les matrices de transfert (matrice T) et « scattering matrices » (matrice S), peuvent être utilisées afin d'obtenir au final les coefficients de transmission et de réflexion. L'algorithme de matrice T requiert une procédure de renormalisation pour éviter les problèmes d'instabilité liées à la nature exponentielle croissante ou décroissante des ondes propagatives et contra-propagatives au sein d'une même couche qui rend le problème matriciel à résoudre mal conditionné du fait de la grande variation des termes contenus dans les matrices. L'algorithme de matrice S est stable par son principe qui consiste à modifier l'écriture des équations pour calculer l'évolution des ondes entrantes dans le dispositif en fonction des ondes sortantes. Dans ce cas les termes exponentiels qui apparaissent dans les matrices sont uniquement exponentiels décroissant et tendent vers 0, ce qui assure la stabilité de la méthode. Le prix à payer de cette stabilité est que la manipulation de matrice est plus complexe au détriment de la rapidité de calcul. Dans ce travail, nous avons choisi la méthode des matrices S compte tenu de sa stabilité numérique. L'implémentation de cette méthode est détaillée dans le manuscrit principal. Ici, nous allons seulement illustrer sur deux exemples la validation du code mis en œuvre et l'utilisation qui en a été faite pour l'optimisation de l'absorption dans une couche photosensible dédiée à des applications dans le domaine du photovoltaïque.

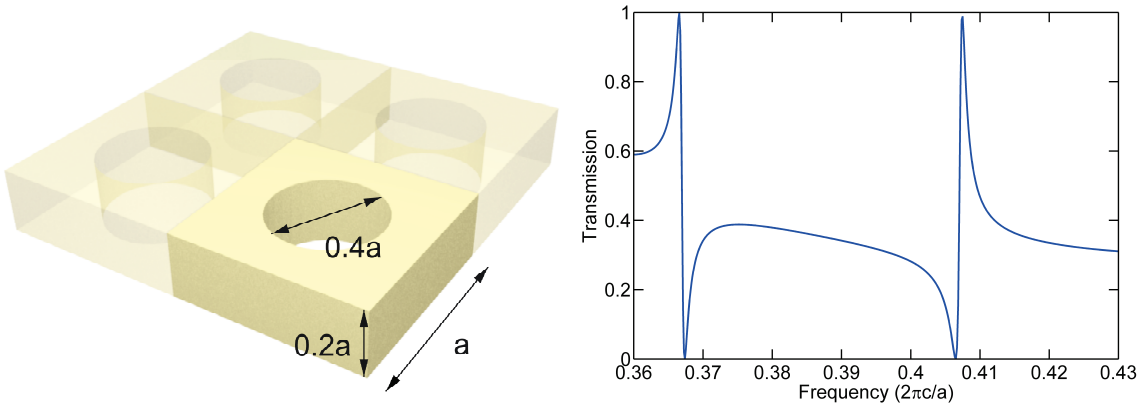

(a) (b)

FIGURE 12: (a) Cristal photonique de silicium ($\epsilon = 12$) constitué d'un réseau carré de trou cylindrique d'air de période a, de rayon $0.2a$ et d'épaisseur $0.5a$. (b)Spectre de transmission en fonction de la transmission.

Validation du Code

La précision de la RCWA est directement liée au nombre de coefficients de Fourier utilisés dans la simulation. Dans le cas de réseaux 1D, si n ordres de diffraction sont considérés les tailles des matrices considérées dans les calculs sont de $2n+1$. Dans le cas de réseaux 2D, elles sont de $(2n+1) \times (2m+1)$ pour prendre en compte les deux directions de l'espace. Contrairement à des méthodes de discrétisation telle que les méthodes aux différences finies, les matrices utilisées sont pleines et le temps de calcul augment de façon spectaculaire avec le nombre d'ordres de diffraction pris en compte. Il est donc nécessaire de limiter ce nombre. Le critère qui est utilisé et de regarder l'évolution des coefficients de réflexion et de transmission en fonction du nombre d'ordres utilisés et de le fixer lorsque la précision est inférieure à une valeur de 10^{-2} qui correspond à la précision avec laquelle on peut mesurer expérimentalement ces coefficients de réflexions et transmissions.

Un exemple de calcul est illustré sur la figure 12 qui représente le spectre de transmission en fonction de la pulsation pour un réseau 2D de période a et d'épaisseur $0.5a$. Le rayon des trous circulaire est de $0.2a$. La courbe de transmission obtenue par la méthode RCWA se superpose exactement avec le même calcul effectué avec un code commercial de FDTD. On constate que la courbe de transmission présente deux résonances de Fano qui sont la signature de la présence de deux modes guidés couplés au

cristal photonique 2D. C'est ce phénomène de couplage vers ces modes guidés que l'on cherche à favoriser dans nos dispositifs parce qu'il va permettre d'accroitre l'absorption de la lumière incidente.

5. Le Contrôle des Photons dans les structures Périodiques

Le problème des structures strictement périodiques et que l'absorption induit par le couplage aux modes guidés du cristal photonique est significatif uniquement pour une gamme de pulsation ou de longueurs d'ondes réduite, comme l'illustre la figure 12a. Un moyen d'élargir le spectre d'absorption est d'utiliser des structures pseudo-désordonnées parce que le couplage de la lumière incidente vers les modes guidés du cristal photonique peut se faire sur plusieurs ordres de diffractions différents, ce qui permet de faire apparaitre plus de résonances dans le spectre.

La simulation des structures pseudo-désordonnées utilise une méthode de super-cellule, qui consiste à utiliser une période plus grande, par exemple de $4a$, constitué de 4 trous. Lorsque les trous sont identiques et parfaitement centrés sur la période, le calcul est identique à celui de la structure représenté sur la figure 12. Le pseudo-désordre peut être introduit soit par déplacement des trous les uns par rapport aux autres, soit par modification des rayons ou bien les deux. Le degré de désordre augmente avec la taille de la super-cellule, ainsi que le nombre de paramètres à ajuster et le nombre d'ordres de diffraction à considérer.

On constate que l'optimisation de telles structures devient rapidement inextricable. Il est nécessaire d'élaboré une stratégie efficace. Pour des raisons de simplicité, nous proposons ici une nouvelle méthode de génération de motifs multi-périodiques unidimensionnels non redondant dans le but de diminuer considérablement de temps de calcul et d'obtenir un optimum global du dispositif. La non redondance est obtenue en définissant une classe de motifs multi-périodiques équivalent en utilisant les propriétés de symétrie d'une super-cellule répétée infiniment. Dans ce cas, toutes les structures appartenant à la classe ont exactement la même réponse optique. Au lieu d'étudier toute les combinaisons

possibles, l'optimisation se réduit à un calcul par classe, ce qui réduit considérablement le temps de calcul. Cette réduction est d'autant plus importante que la super-cellule est grande, ce qui ajoute un intérêt supplémentaire à cette nouvelle technique. A titre d'exemple, nous montrons comment cette approche peut être utilisée pour optimiser globalement et à analyser systématiquement au problème du piégeage large bande de la lumière dans un film mince.

Technique dite du collier

Le procédé de génération des motifs est basé sur une technique d'analyse combinatoire nommée collier. C'est une méthode générale pour construire des modèles uniques qui sont infiniment répétées. Plus précisément, nous nous concentrons sur le problème de collier libre ou un problème de bracelet, ce qui signifie des orientations opposées (images miroir) sont considérées comme équivalentes.

Considérons d'abord une chaîne de n caractères où chaque personnage peut prendre une valeur parmi les possibilités de k, le nombre total de toutes les chaînes possibles est :

$$S_k(n) = n^k \tag{1}$$

Si nous remplaçons la chaîne par un collier, grâce à une symétrie de rotation, le nombre de colliers possibles ou de structure non redondantes se réduit à :

$$B_k(n) = \begin{cases} \frac{1}{2}N_k(n) + \frac{1}{4}(k+1)k^{n/2} & n \text{ even} \\ \frac{1}{2}N_k(n) + \frac{1}{2}k^{(n+1)/2} & n \text{ odd} \end{cases} \tag{2}$$

Nous utilisons un algorithme pour générer de manière efficace tous les bracelets possibles avec différentes longueurs de séquences de code. Ensuite, nous combinons l'algorithme de génération de bracelet avec le calcul rigoureux RCWA pour obtenir la réponse du Cristal Photonique (CP). Comme nous prenons en compte tous les arrangements possibles, la réponse optimale obtenue correspond à un maximum global et non pas local, contrairement aux algorithmes heuristiques (par exemple Algorithmes Génétiques). Notre processus d'optimisation conduit toujours à la meilleure structure

compte tenu des paramètres et de la taille de la super-cellule utilisée, ce qui nous permet également d'étudier l'influence de la taille de la super-cellule.

A titre d'exemple, une épaisse couche de Silicium cristallin (c-Si) 1 µm a été choisi pour étudier le piégeage de la lumière sous incidence normale non polarisée. Tous les modèles ont été générés sur la base de cette seule couche. Pas de revêtement et réflecteur arrière antireflet ont été utilisés pour des raisons de simplicité et de clarté. L'absorption intégrée (I_{abs}) dans une gamme de longueurs d'onde comprise de 300 à 1100 nm a été calculée comme facteur de mérite.

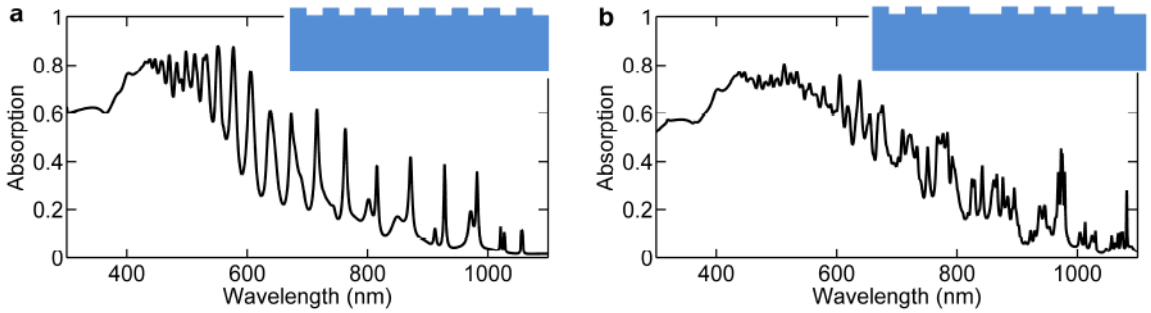

FIGURE 13: Evolution des spectres d'absorption d'une couche épaisse de 1 µm c-Si en fonstion de la longueur d'onde pour une lumière incidente non polarisée et une incidence normale au plan des couches, (a) pour la structure mono-périodique optimisé avec une longueur de réseau de 300 nm (l'encart montre la forme de la modulation) et (b) pour la structure multiples-periodique optimisée avec une longueur de réseau de 2550 nm (l'encart montre la forme de la modulation).

Résultats et Discussion

Dans un premier temps, nous avons utilisé l'algorithme PSO (particle swarm optimization) pour optimiser l'absorption de la couche de c-Si en faisant varier 3 paramètres (période, la profondeur de modulation et la fraction de remplissage) pour un réseau mono-périodique. Le modèle le mieux adapté ayant l'absorption intégrée la plus grande (I_{abs} de 37,7%) est obtenue pour une profondeur de gravure de 100 nm, 300 nm de période, et un facteur de remplissage de 0,5. (Fig. 13a) Ensuite, les modèles multi-périodiques décrits dans le paragraphe précédent ont été générés en conservant la profondeur de gravure identique et une taille de motif élémentaire de 150 nm. Des codes de séquences '1' pour un motif et '0' pour un creux ont été générés en augmentant la période de manière

à obtenir des pseudo-périodes de plus en plus complexes. Les séquences optimisées pour différentes longueurs de codes binaires sont répertoriées dans le Tableau 1. Des absorptions intégrées I_{abs} ($> 40\%$) sont obtenues pour des motifs contenant au moins 12 caractères. Lorsque la période de motif multi-périodique est égale à 2,550 nm (contenant 17 caractères), une valeur de I_{abs} maximale de 42,2% est obtenue (Fig. 13b), ce qui est 11,9% fois supérieur à celle du motif mono-périodique optimisé (Fig. 13a). Dans le manuscrit principal, nous allons étudier en détail comment le modèle multi-périodique améliore l'absorption de sur une large bande spectrale.

Les résultats obtenus ont montré l'efficacité de l'approche originale développée dans ce travail de thèse. Ce concept pourrait être encore plus efficace pour les motifs binaires plus complexes.

TABLE 1: Séquences de codes optimisés avec différentes longueurs de codes binaires (N). Les séquences de codes égalent à zéro ont été exclus. Les motifs avec une longueur de réseau de 2700 nm et 3000 nm ont été optimisés avec la contrainte à 50% de fraction de remplissage en raison de la lourde charge de calcul.

N	Longueur lattice	Séquence de code	I_{abs}
2	300 nm	10	37.7%
4	600 nm	1010	37.7%
6	900 nm	101100	38.8%
8	1200 nm	10101100	39.2%
10	1500 nm	1010101100	39.7%
12	1800 nm	101001100100	40.7%
14	2100 nm	10101101100100	41.1%
15	2250 nm	110010010100100	41.7%
16	2400 nm	10101101001101 00	42.1%
17	2550 nm	10101100101010100	42.2%
18	2700 nm	101010101011001100	41.8%
20	3000 nm	10101011010110010100	42.1%

6. Conclusions et Perspectives

Les structures périodiques jouent un rôle important dans les nanotechnologies. En faisant usage de l'attribut le plus important de ce type de matériel, à savoir la périodicité, des procédés de fabrication sur mesure et une méthode d'optimisation des propriétés

optiques ont été présentés dans cette thèse.

La première partie de la thèse a été axée sur la fabrication. La lithographie LIL disponible au laboratoire a fait l'objet d'une étude systématique afin d'obtenir une variabilité et une homogénéité des motifs accrues. La combinaison de la lithographie LIL avec différentes techniques comme, la gravure sèche, la gravure humide, et la gravure électrochimique, ont permis d'élaborer différents types de dispositifs utilisant des structures périodiques dans le domaine de la fluidique. Des nano-canaux cylindriques de 250 nm de diamètre et de 5 µm de hauteur ont été réalisés dans le but de fabriquer des transistors fluidiques. En outre, une puce de préconcentration à faible coût a également été fabriquée en combinant la lithographie LIL et la xurography.

Dans la deuxième partie, nous nous sommes concentrés sur les propriétés optiques de nanostructures périodiques. Un outil de simulation électromagnétique, basé sur la méthode RCWA a été développé. Nous avons démontré la précision de cette méthode par comparaison avec un outil de FDTD. Un nouvel algorithme d'analyse combinatoire couplé avec la méthode RCWA a été appliqué pour optimiser et comprendre le rôle de motifs pseudo-aléatoire sur le contrôle des photons dans les matériaux absorbants tel que le silicium en couche mince.

Il y a plusieurs sujets qui pourraient faire l'objet de travaux complémentaires.

- Nous avons montré que le réseau de pores avec une période de 300 nm n'était en fait pas la limite de cette technique. Une réduction du diamètre des pores et de la période pourrait faire l'objet de travaux complémentaires.

- La méthode que nous avons développée RCWA n'était pas entièrement fonctionnel. Plusieurs améliorations pourraient être apportées pour réduire le temps de simulation et, dans le même temps, augmenter la précision, tels que la factorisation rapide de Fourier, la moyenne des sous-pixels et etc. En outre, les différentes méthodes numériques de simulation existantes (Méthode des Eléments Finis ou Méthode des Différences finies dans le domaine fréquentiel) pourraient être couplées avec la RCWA d'étudier les couches structurées avec un indice de réfraction élevé ou la structure varie lentement dans la direction z.

- La méthode de génération de modèle unidimensionnel pourrait être combinée avec d'autres méthodes d'optimisation telle que les Algorithmes Génétiques et PSO pour préfiltrer l'espace de recherche. Dans un pool de recherche réduit, ces méthodes d'optimisation traditionnelles pourraient être plus efficaces. De cette façon, les méthodes électromagnétiques intensives de calcul peuvent être directement utilisées pour optimiser de façon rigoureuse sans explosion du temps de calcul.

- Le procédé de génération d'un motif unidimensionnel pourrait être étendu à deux dimensions. Une approche réaliste serait d'étendre le modèle dans l'espace réciproque et ensuite de basculer dans l'espace réel compte tenu de la complicité du problème bidimensionnel.

Contents

List of Figures

List of Tables

Chapter 1

Introduction

The understanding and manipulating of the properties of materials lead to the evolution of our civilization. From Stone Age to Iron Age, our ancestors understood more what Mother Nature can provide us. Few hundred years ago, we started to build artificial materials, such as ceramics and plastics with tremendous new properties. Last century, we opened up the nanomaterial age. Over the last few decades, nanotechnology has been shaping our world enormously. By building structures over the length scales of 10-100 times the size of the individual atoms, materials behave significantly different from their respective bulk properties [1]. In the category of nano-scale materials, periodic nanomaterials play an important role because of the geometric configuration.

1.1 Fabrication of Periodic Nanostructures

In fabrication, optical lithography, Electron-Beam Lithography (EBL) and Nanoimprint Lithography (NIL) have been widely used. Optical lithography is well established to manufacture integrated circuit devices. However, it is fundamentally limited by Rayleigh relation [2] to fabricate structures down to nanometer scale. Even though EBL can compensate the limit to produce very fine structures, it suffers from low throughput [3]. NIL is a cost-effective technique for producing nanopatterns over a large area [4]. But it is not suitable for rapid and flexible prototyping in lab scale since a premade mask is needed in the fabrication process. And most of time this mask is fabricated by other

techniques such as optical lithography or EBL. Fortunately, a significant proportion of applications such as photonic crystal [5], data storage [6, 7], etc.[8], require only periodic patterns. As such, an alternative technique named Laser Interference Lithography (LIL) [9, 10] appears to be well-suited to lab-scale fast prototype at a low cost. LIL is a quick technique for patterning distinct periodic structures on a large surface without complex optical systems. The most remarkable merits are the flexibility, simplicity, and fidelity. This technique is capable of making one-, two- or even three- dimensional structures with high precision and flexible periodicity [11]. In this dissertation, we focus on one- and two- dimensional structures. By combining with other pattern transfer techniques, the LIL fabricated periodic structures can be used to investigate nanofluidics [12], and most importantly photon control in periodic structures [13–15].

In Chapter 2, we introduce LIL technique and its basic principle. Detailed strengths and limitations concerning our particular setup, Lloyd's mirror interferometer, are described. Different shapes of patterns that can be fabricated are also demonstrated. Besides, the structural transfer techniques (wet etching and dry etching) from the patterned photoresist to silicon substrate are explored. Fabricated cylindrical and pyramid-shaped structures with different periods are illustrated.

In Chapter 3, we describe different applications of periodic nanostructures fabricated by LIL. In the first part, a microporous silicon array with the period of 300 nm on a centimeter-scale substrate is made by the combination of LIL and electrochemical etching. We demonstrate the fabrication of wide-area and high-aspect ratio 2D pore arrays with 250 nm diameter and 5 µm depth. All steps of the process have been optimized to achieve vertical sidewalls with 50 nm thickness, providing pore arrays with an aspect ratio of 100 on n-type silicon substrates over an area of $2 \times 2\,\mathrm{cm}^2$. In the second part, we discuss the application of one-dimensional nanostructures. A preconcentration device, which uses the one-dimensional periodic structure as a nanofluidic filter, is discussed. The combination of LIL and xurography enables us to fabricate simple and low-cost preconcentration chips based on ion concentration polarization phenomenon.

1.2 Optical Simulation of Periodic Nanostructures

Even though LIL is a relatively fast technique for prototyping, rigorous electromagnetic simulation methods are still needed to accelerate the optimization and design process, which leads us to the second part of the thesis: rigorous electromagnetic simulation and optimization of optical structures. In the scope of rigorous optical modeling, the finite difference [16–18], finite element [19], and Fourier-based methods [20] have been proposed. To tackle our particular problem, we chose a Fourier-based method to perform rigorous optical simulations. The decision was made by adapting to the common underlying physical characteristic of our structures, namely periodicity. The chosen method named Rigorous Coupled-Wave Analysis (RCWA) or Fourier Modal Method (FMM) is very efficient for rigorously calculating the optical performance of periodic structures. Compared with other widely used methods like Finite-Difference Time-Domain (FDTD) method or Finite Element Method (FEM), we argue that RCWA is more adapted to simulating periodic structures. In both FDTD method and FEM, simulated structures have to be discretized in a regular grid or irregular grid to perform calculations. The number of computing points can be enormous if the structure is large or contains fine features. However, in RCWA method, structures and fields are represented in Fourier basis, which, in most cases, contains very few points. As such, the calculation burden of the RCWA method is not as heavy as that of the other two methods. Also, being a semi-analytical method, the propagation of the eigenmodes in each layer is calculated analytically regardless of the thickness of the layer. Therefore, RCWA is very efficient for computing thick devices. The largest disadvantage of RCWA method is that only periodic structures can be simulated. In this work we only consider periodic structures, RCWA method is therefore preferable.

In Chapter 4, we start to consider the optical properties of periodic structures. The RCWA method is introduced and the formulations are presented in detail. A validation of the developed code is given to verify the accuracy at the end. A comparison between the FDTD and RCWA methods is shown to highlight the calculation accuracy of the RCWA method for periodic structures.

In Chapter 5, we investigate another kind of periodic structures named pseudo-

disordered structures. They seem to be chaos in short range, yet they are periodic based on extending unit cell. This pseudo-disordered design concept enables additional design freedom for photon management, but the benefit comes with a penalty, as the optimization and interpretation are challenging when a large number of degrees of freedom encounters computationally intensive electromagnetic simulation method. Here, we propose a novel one-dimensional multi-periodic pattern generation method to help us squeeze the disorder design space before performing the rigorous calculation, by making use of the periodic attribute of the patterns. Consequently, thanks to the pre-filtered design space, it typically relieves us from the computational burden and enables us to 'globally' optimize and study pseudo-disordered patterns. As an example, we show how this approach can be used to comprehensively optimize and systematically analyze generated disorder for broadband light trapping in thin film.

In Chapter 6, we conclude by providing an overview of the work done in this dissertation and discuss possible future directions this research can take.

Chapter 2

Nanostructure Fabrication by Using Laser Interference Lithography

In this section, we will first provide a brief overview of the Laser Interference Lithography (LIL) technique and its basic principle. And then the structural transfer from the photoresist to the silicon substrate through dry etching and wet chemical etching is discussed. We then illustrate the strengths and limitations of this technique with the demonstration of different kinds of fabricated periodic patterns.

2.1 Interference of Light Waves

LIL is a technique for patterning regular arrays of delicate features, by using two interfering incident beams. Typically, two coherent beams interfere and set up interference patterns that can then be recorded by photoresist. Based on this physical principle, there exist two kinds of interference lithography setups, namely Mach-Zehnder Interferometer and Lloyd's-Mirror Interferometer [9]. The focus of this thesis is the second one.

2.1.1 Periodicity of interference patterns

When two coherent laser beams coincide, an interference pattern is created as illustrated in Fig. 2.1. It can be interpreted as the superposition of two plane waves. For two overlapping plane waves with the intensity of I_1 and I_2, the interfered intensity

distribution I at a given spatial point can be described by

$$I = I_1 + I_2 + 2\sqrt{I_1 I_2}(\hat{e}_1 \cdot \hat{e}_2)\cos\left[\left(\vec{k}_1 - \vec{k}_2\right) \cdot \vec{r}\right] \tag{2.1}$$

where $\hat{e}_1$ and $\hat{e}_2$ are the directions of the two plane waves, $\hat{k}_1$ and $\hat{k}_2$ are the wave vectors of the plane waves, $\hat{r}$ is a given spatial point.

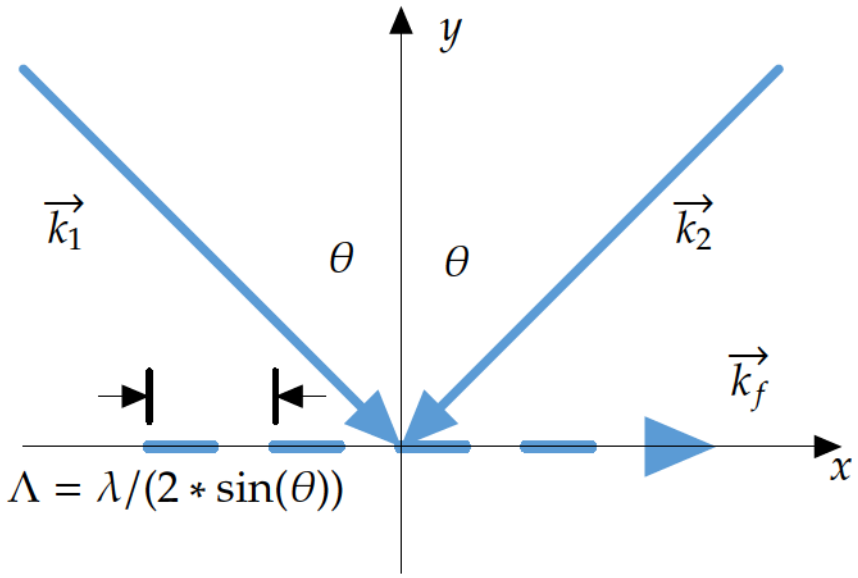

Figure 2.1: The periodicity of the interference pattern is defined in the symmetrical case where bisection of the angle of interference of the beams is perpendicular to the plane of observation of the fringes.

In Eq. 2.1 we do not take into account the phase difference between the two waves because it only shifts the sinusoidal interference pattern. The spatial dependence of this equation occurs only in the phase argument of the cosine. The maxima and minima of this sinusoidal pattern are called fringes, which is the salient feature for most lithography applications. Because of its importance, we use a vector named fringe-vector (k_f) to define it.

$$\vec{k}_f = \vec{k}_1 - \vec{k}_2 \tag{2.2}$$

In our case, the angles of incidences are equal, and the two incident beams have the same wavelength (λ). So in the illustrated coordinate system where $\hat{x}$ axis is in the

same direction as fringe-vector (Fig. 2.1), the fringe-vector will be simplified as

$$\vec{k}_f = 2k_{1x}\hat{x} \tag{2.3}$$

where k_{1x} is the x-component of $\vec{k}_1$. The spatial periodicity Λ of the interference fringes can be calculated as

$$\Lambda = \frac{2\pi}{\left|\vec{k}_f\right|} \tag{2.4}$$

Defining the angle between the two incidence vectors as 2θ, we can easily get

$$\sin\theta = \frac{k_{1x}}{\left|\vec{k}_1\right|} \tag{2.5}$$

Substituting Eqs. 2.5 and 2.3 in to Eq. 2.4 the spatial periodicity can be simply calculated as in Eq. 2.6.

$$\Lambda = \frac{\lambda}{2\sin(\theta)} \tag{2.6}$$

Note that even though the coordinate system was specified to enable the derivation, Eq. 2.6 is valid for any arbitrary coordinate system. The spatial periodicity is only dependent on the interference angle θ, as long as the direction over which the measured fringe period is perpendicular to the bisection of the interference angle.

2.1.2 Visibility of interference patterns

Achieving energy intensity differentiation is the ultimate goal in lithography. In LIL, it is achieved by destructive and constructive interference, which is essentially an energy redistribution process. The visibility of the fringes is closely related to the contrast of the redistributed energy intensity. Compared with that, the absolute intensity of an interference pattern is less crucial since it can be regulated by exposure time. We use parameter V to quantify the contrast or visibility, which is defined in Eq. 2.7

$$V = \frac{I_{\max} - I_{\min}}{I_{\max} + I_{\min}} \tag{2.7}$$

where I_{max} and I_{min} are the maximum and minimum intensity values, respectively.

From our previous discussion, I_{max} and I_{min} can be easily found by setting the value of the cosine term in Eq. 2.1 to 1 and -1, respectively, corresponding to constructive and destructive interference.

$$\begin{aligned} I_{\max} &= I_1 + I_2 + 2\sqrt{I_1 I_2}(\hat{e}_1 \cdot \hat{e}_2) \\ I_{\min} &= I_1 + I_2 - 2\sqrt{I_1 I_2}(\hat{e}_1 \cdot \hat{e}_2) \end{aligned} \tag{2.8}$$

Then the contrast of the interference patterns can be calculated by substituting the above equations into Eq. 2.7, which is given in Eq. 2.9

$$V = \frac{2\sqrt{I_1 I_2}}{I_1 + I_2}(\hat{e}_1 \cdot \hat{e}_2) = \frac{2\sqrt{I_r}}{I_r + 1}(\hat{e}_1 \cdot \hat{e}_2) \tag{2.9}$$

where I_r is the relative intensity equaling to I_1/I_2.

The dot-product is determined by the polarization of the incidence. For this reason, TE (electric field is perpendicular to the plane-of-incidence) and TM (electric field is parallel to the plane-of-incidence) polarizations have to be discussed separately. Note that the superposition of these two modes is sufficient to describe an arbitrarily polarized incidence.

The situation for TE polarization is relatively straightforward, as the dot-product is always equal to unity. Eq. 2.10 can be simplified as

$$V_{TE} = \frac{2\sqrt{I_r}}{I_r + 1} \tag{2.10}$$

Fig. 2.2a shows the relationship between I_r and V_{TE} for TE mode. As we can see, the visibility is maximized when the intensities of the two beams are equal. We also notice that the fringe contrast is tolerant to intensity mismatch, which demonstrates the solidity of the technique.

A more complex situation occurs for TM mode. The dot-product can be expressed with the interference angle θ in the function below.

$$\hat{e}_1 \cdot \hat{e}_2 = -\cos(2\theta) \tag{2.11}$$

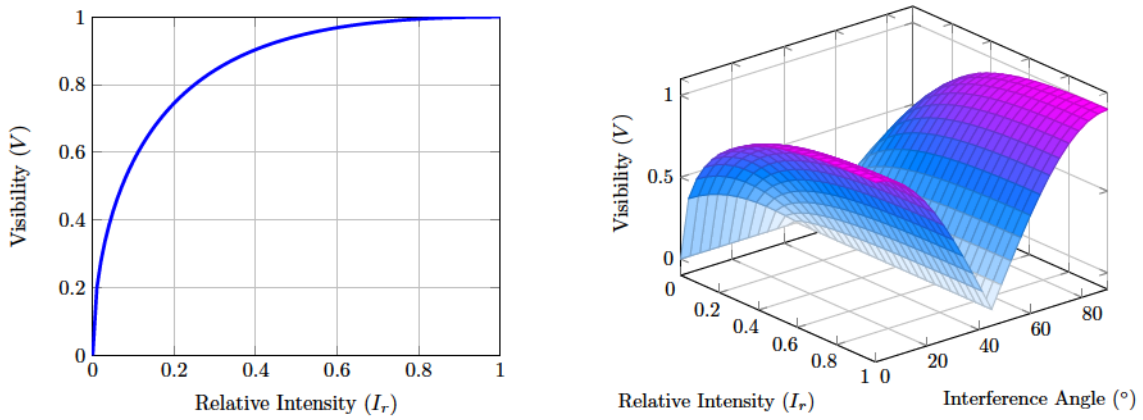

(a) TE mode

(b) TM mode

Figure 2.2: Fringe contrast as a function of the relative intensity of the two interfering beams and their interference angle for both TE and TM modes. (a) TE mode. (b) TM mode.

Substituting the above equation into Eq. 2.9, we get the visibility equation for the TM polarization.

$$V_{TM} = \frac{2\sqrt{I_r}}{I_r + 1} |\cos(2\theta)| \tag{2.12}$$

The visibility is the function of relative intensity and interference angle (θ) which is plotted in Fig. 2.2b. The highest contrast also appears when the intensities of the two beams are equivalent; however, the interference angle also plays an important role. The interference contrast will be high for interference angle close to 0° or 90° indicating the electric fields are parallel or anti-parallel. As such, TE polarization is desirable in LIL in order to achieve high and angular independent exposure contrast.

2.1.3 Standing wave

The interference between two coherent beams creates the periodic pattern on the photoresist. In actual cases, a second interference pattern appears in the vertical direction when the thickness of the photoresist is taken into account. It is caused by the interference entering incoming beam and substrate surface reflection in photoresist, as illustrated in Fig. 2.3. The undesired standing waves become a problem for highly reflected materials such as metals or silicon. The actual profile of the exposed photoresist

is shaped by the adding effect of these two interferences. The visibility of the vertical interference is consistent with Eq. 2.9. As the intensities of the incoming beam and reflected beam are not constant across the photoresist, the visibility is changing in the exposed photoresist. One common way to eliminate the vertical standing wave is to prevent the light from bouncing inside the photoresist layer by adding an anti-reflection layer beneath the photoresist [21]. In our case, a 100 nm thick silica layer is added on the top of the silicon substrate, acting as an anti-reflective layer, to decrease the vertical standing wave. This layer can also be used as a hard mark in the following etching process.

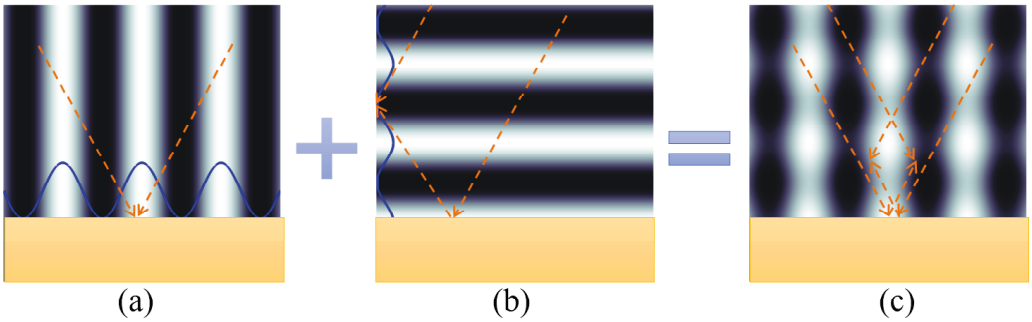

Figure 2.3: Schematic illustration of the formation of standing waves. (a) Two-beam interference pattern. (b) Standing waves created by surface reflection. (c) Combined standing waves.

2.2 Laser Interference Lithography Setup

There are two kinds of LIL setups, named Mach-Zehnder interferometer and Lloyd's Mirror interferometer, respectively. The first one, Mach-Zehnder interferometer, is mainly used as a production tool to expose large area substrate. This system falls short when it comes to lab-scale prototyping mainly because it requires a dedicated set of expensive optical elements and re-alignment of the optical path for different fringe periods. Beyond that, it is also sensitive to surrounding environment, such as airflow [9]. Compared with the first one, the Lloyd's Mirror interferometer is more economical and robust for lab use. It can be easily adjusted to meet applications that require a multitude of different periods. In this thesis, we will focus on the Lloyd's Mirror interferometer.

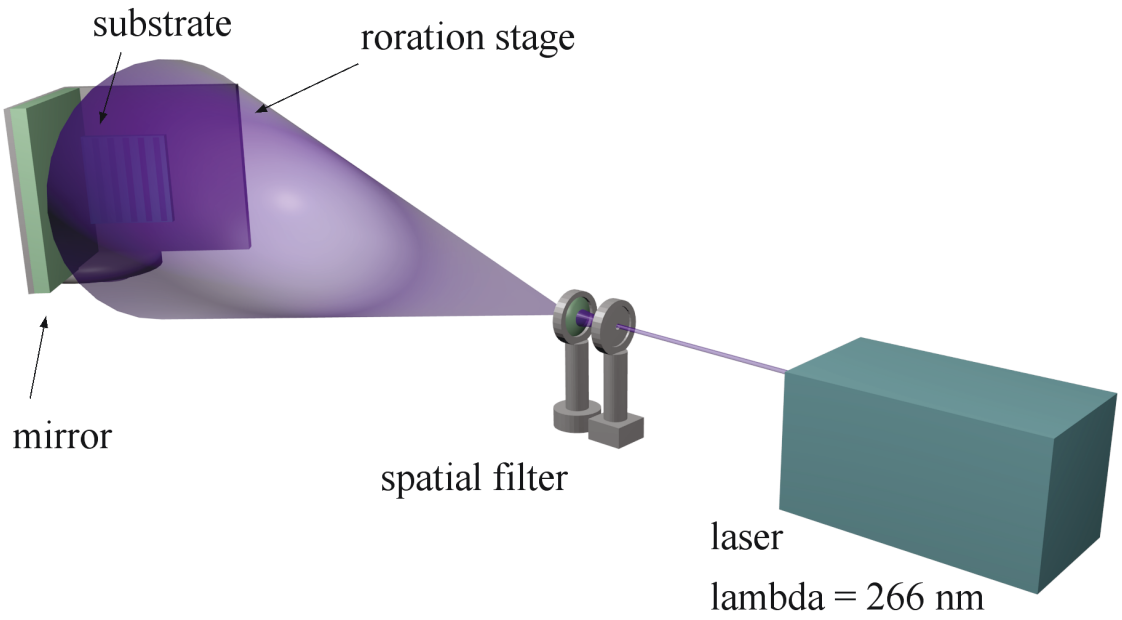

Figure 2.4: Schematic of the Lloyd's mirror interferometer. The beam from a semiconductor laser ($\lambda = 266\ nm$) is spatially filtered and allowed to expand to 2 meters. The mirror and substrate are mounted on a rotation stage for easy adjustment of the fringe period.

2.2.1 Lloyd's Mirror interferometer

The Lloyd's Mirror interferometer is composed of three main parts: a laser, a spatial filter, and an interferometer. A schematic illustration of the implementation of the Lloyd's Mirror interferometer is shown in Fig. 2.4. A semiconductor laser is chosen to be the source. A spatial filter is placed between the laser and the interferometer, providing a "clean" Gaussian profile beam thanks to the speckle effect. The interferometer consists of a station stage, a mirror, and a substrate chuck. It is placed far away from the spatial-filter to ensure a large beam diameter. The increase of the beam diameter creates a homogeneous intensity distribution over the exposed area, which is close to the plane-wave interference approximation. As such, the fabricated fringes are more homogeneous [22].

The elegance of Lloyd's Mirror interferometer is the result of the usage of the mirror. By using the mirror, only one incident source is required, as the mirror provides the other virtual incident beam. Since the mirror is placed perpendicular to the substrate

chuck as shown in Fig 2.5. It should be obvious that a perfectly aligned image source is produced regardless of the real source position. Because of that, two incident lights are always aligned to interfere with each other. So different interference angles can be easily adjusted to realize patterns with different periods by simply rotating the station stage, on the condition that the location of the source is fixed in space.

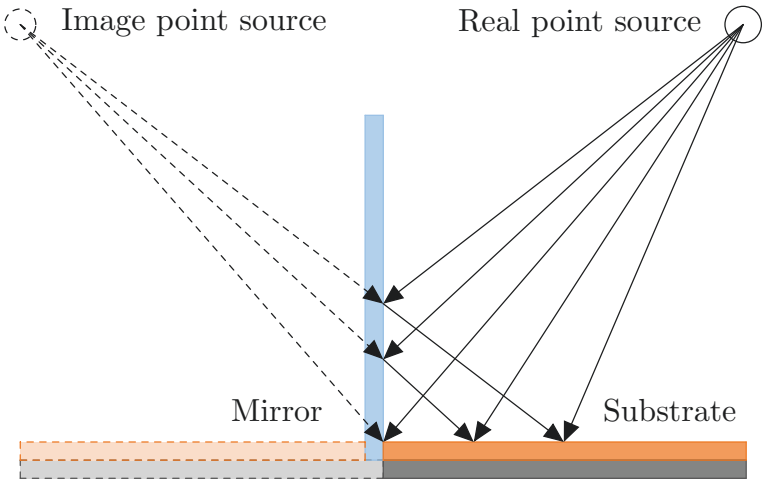

Figure 2.5: The production of image source by using Lloyd's Mirror.

Another advantage of the Lloyd's Mirror is that it is immune to small vibrations. A rigid mechanical connection between the mirror and substrate chuck means that the relative length of the two arms is very stable since variations in arm length can only occur if the mirror moves about the substrate. In general, small vibrations of the assembly or wandering of the incoming beams does not cause fringe drift, as the image source created by the mirror will automatically compensate. The high inherent stability of the system enables long exposure time, which in turn allows either the use of a low power laser or long beam expansion distance.

So far the use of the mirror enables the Lloyd's Mirror to have some benefits such as simple to align, highly robust and easy to configure for different fringe periods. Thus, the choice of the mirror becomes critical for the whole system. The imperfections of the mirror can be roughly divided into four categories. Attention should be paid to each of them when choosing the mirror.

The first is flatness. The roughness of the mirror causes phase error for the reflected

beam, which will then print as a distortion in the interference fringes. Such distortions will be systematic and repeatable as long as the same mirror is used. For this reason, a mirror with high flatness is always preferred.

The second is local surface defects. These could be scratches, fingerprint, dust particles, etc. These defects act as additional coherent point sources. The recorded reference pattern will be the sum interference of the two beams plus the additional point source on the mirror. Large defects will print directly in the fringe due to loss of reflected power. Of course, these are rare cases. Most of the time the defects are very small even not visible to human eyes. The observed exposure will still be a grating but local distorted such as rippling of the line on a large scale. So great care should be taken to keep the mirror clean.

The third is reflectivity. The qualified mirror should be highly reflective regardless of the reflection angles, as a broad range of incidence angles are used to expose different period gratings. Fortunately, the reflectivity is not such strict. In practice, a minimum reflectivity value of 0.85 in the interested wavelength is enough to have a high fringe visibility, as illustrated in Fig. 2.2. We also notice that beams with very different intensities are still able to make a high fringe contrast. It underlines the necessity to prevent coherent scattering.

The fourth is mirror size. The physical size of the mirror affects the fringe formation in two different ways: the uniformity of the fringe and the exposure size. For the first one, it is desirable to have larger expanded beam than the size of the exposure area. It also means that the beam diameter is larger than the mirror size, so diffraction or scattering beam from the edge of the mirror will not affect the fringe. The use of a large mirror will prevent this from happening in most cases. The second impact of the mirror size is the limiting effect on exposure area. Obviously, the interference can only occur in the region where there are two beams. The illumination distance (W) of the reflected beam is a function of the mirror size (L) and incident angle (θ), as shown in Fig. 2.6. The maximum distance W in Eq. 2.13 is the sample size limit.

$$W = L\tan(\theta) \tag{2.13}$$

Considering the angle θ is directly related to the accessible fringe periods, the mirror size limits the exposed area of large period gratings. For small period gratings, the mirror size is not the restricting parameter.

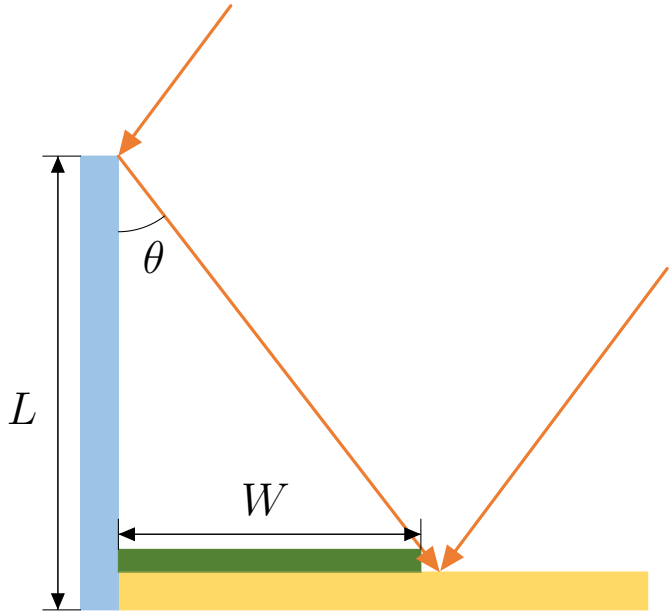

Figure 2.6: Maximum distance W from the wafer for which interference will occur is a function of the incident angle θ and the fringe period.

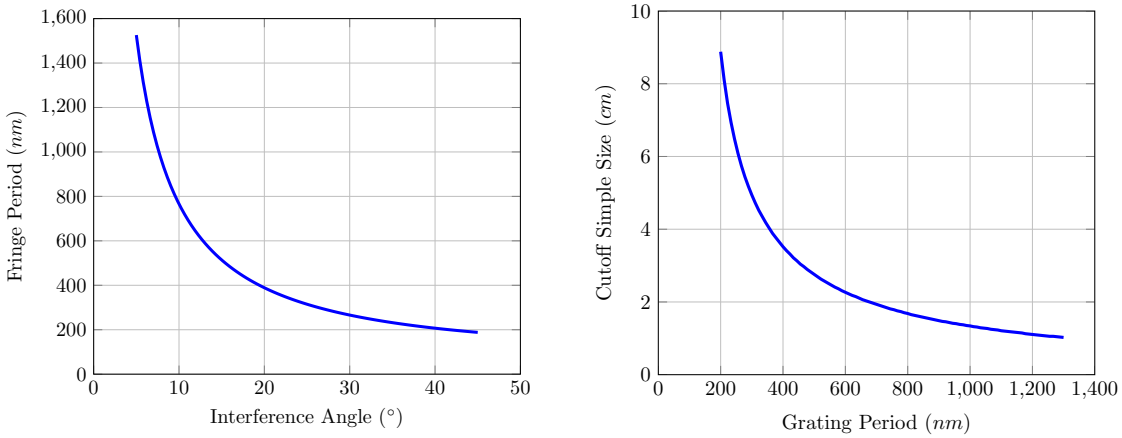

(a) (b)

Figure 2.7: (a)Fringe period is a function of the interference angle for our setup with a laser of wavelength of 266 nm. (b)Maximum distance W is a function the grating period for our setup with a fixed 10 cm side length mirror.

For our specific setup, every component was carefully chosen to satisfy our needs. A laser emitting at 266 nm acts as a light source. As shown in Eq. 2.6, the emission wavelength of the laser source determines the variation range of the available fringe periods. Our setup enables us to fabricate patterns with accurate periods ranging from 150 to 700 nm, as shown in Fig. 2.7a. In a practical case, the minimum available period is also determined by other facts such as the resolution of the photoresist, which will be discussed in Section 2.2.2. Moreover, the upper periodic limit is also constrained by the required sample size, since the physical dimensions of the mirror are fixed. The mirror currently in use is a 10 cm square aluminum mirror with the flatness of $\lambda/20$. The samples that can be fabricated by this setup are summed up in Fig. 2.7b, which clearly shows the accessible fringe periods and the corresponding sample sizes.

2.2.2 Laser interference lithography process

The lithographic process contains four steps: substrate cleaning, spin coating, photoresist exposure, and development.

The first step is substrate cleaning. The sample is immersed consequently in acetone, ethanol, and deionized water (DI water) to remove surface contamination. The whole process is executed in an ultrasonic bath, and each step lasts about 10 minutes. Acetone is used to remove the organic contamination, which will then be cleaned by ethanol. The remaining ethanol and inorganic ions are rinsed away with DI water. Then, a high-temperature process (@100 $^{\circ}$C, 2 minutes) called dehydration bake is used to remove the adsorbed water. An addition of an adhesion promoter named hexamethyldisilazane (HMDS) is spin coated to promote the adhesion to the photoresist. Subsequently, the photoresist polymer film is deposited on the substrate by using the spin-coating technique which is reliable to form a uniform thin film on samples. The dominant spin-coating parameters to control the film thickness are the acceleration rate, velocity, and spin-coating time without taking into account the property of the photoresist. We used a chemically amplified photoresist named NEB-22 in this thesis. For this particular photoresist, we have calibrated the spin-coating parameters to form a very thin film (approximately 150 nm thick) for the next steps. After spin coating, a prebake process

is performed to remove the excess solvent in the photoresist.

The exposure process is done using the LIL setup. Recall from section 2.1.1 that one-dimensional structures are obtained by exposure the photoresist once. Also, the period is defined by the interference angle (Eq. 2.6) which is further controlled by the rotation angle of the interferometer. More complex periodic structures can be fabricated by multiple exposures. For example, cross-exposure of negative photoresist by rotating the sample at 90° enables the formation of arrays of holes. The aspect of double-exposure sample is determined by the periods of two exposures and rotation angle between two exposures. Fig. 2.8 shows the simulated aspects of three kinds of samples. For chemically amplified resists, which we use here, one more step named post-exposure bake (PEB) has to be performed to finish the exposure process. Because PEB creates a solubility differential between exposed and unexposed parts of the photoresist. Also, it helps to reduce the standing wave effect. [23].

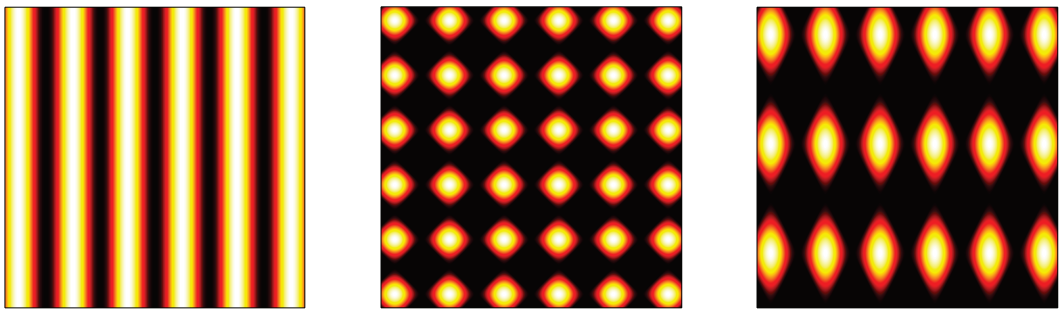

(a) (b) (c)

Figure 2.8: Simulated exposure intensity distribution of three kinds of samples. (a) Single exposure. (b) Double exposure with the same period. (c) Double exposure with different periods.

The whole process is finalized by development and postbake. The development process is the actual step that makes the physical difference between the exposed and unexposed part. We use a developer named MF 702 solution to develop the exposed photoresist. Then the entire sample is rinsed and postbaked (@ 90 °C) to harden the final resist image so that it can withstand the harsh environments of pattern transfer. Fig 2.9 shows the SEM images of three different kinds of samples corresponding to our simulation results in Fig. 2.8. As we can see, the fabricated samples have high

uniformity in both one- and two- dimensional structures, which clearly demonstrates the reliability and utility of our setup.

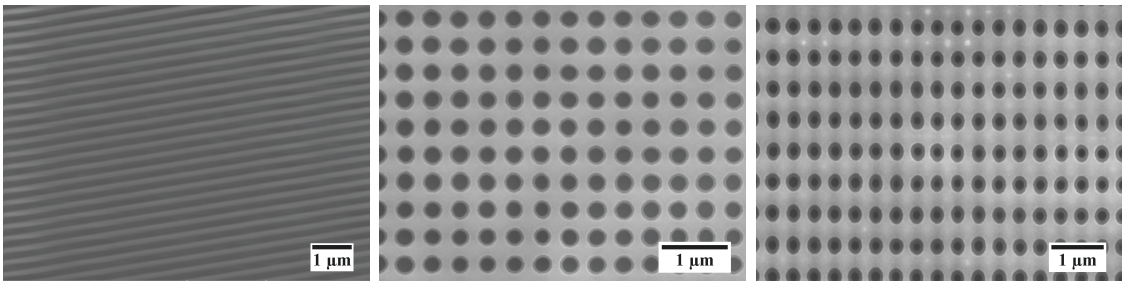

(a) (b) (c)

Figure 2.9: SEM images of fabricated samples that are simulated in Fig. 2.8. (a) Single exposure. (b) Double exposure with the same period. (c) Double exposure with different periods.

2.3 Structure Transfer

The LIL process enables us to draw large-scale periodic structures on a polymer layer. Pattern transfer processes have to be performed to make use of the developed structures. In this part, we talk about two anisotropic etching processes that we use to transfer the photoresist patterns to substrates. The first one is a dry etching process named Reactive Ion Etching (RIE). It is one of the most commonly used pattern transfer techniques in the semiconductor industry. By choosing different etching gases, RIE provides the conveniences of high resolution and anisotropy, which is independent of crystal orientation. The second technique is a wet etching method. Potassium hydroxide (KOH) or tetramethylammonium hydroxide (TMAH) as solutions are used here. In combination with LIL, large-scale inverted pyramids with different periods are fabricated. Compared with RIE, KOH or TMAH etching is also highly anisotropic but of crystal orientation dependence.

2.3.1 Reactive ion etching

RIE uses chemically reactive plasma to remove material deposited on wafers. The plasma is generated under low pressure by an electromagnetic field. High-energy ions

from the plasma attack the wafer surface and react with it. Fig. 2.10 shows a diagram of a common RIE setup. An RIE machine consists of two electrodes that create an electric field meant to accelerate ions toward the surface of the sample. The plasma, generated from the gases, contains both positively and negatively charged ions in equal quantities. In Fig. 2.10a CHF_3 has been pumped into the chamber, making plasma with many Fluorine ions (etching ions). The Fluorine ions are accelerated in the electric field, causing them to collide into the surface of the sample. Fig. 2.10b shows a photoresist mask on silicon dioxide. The etching ions are accelerated into the etching region, where they combine with silicon dioxide and then are dispersed. A hard mask is used to protect certain areas from etching, exposing only the areas desired to be etched. Because the electric field accelerated ions toward the surface, the etching caused by these ions is much more dominant than the etching of radicals-ions traveling in varied directions, so the etching is anisotropic.

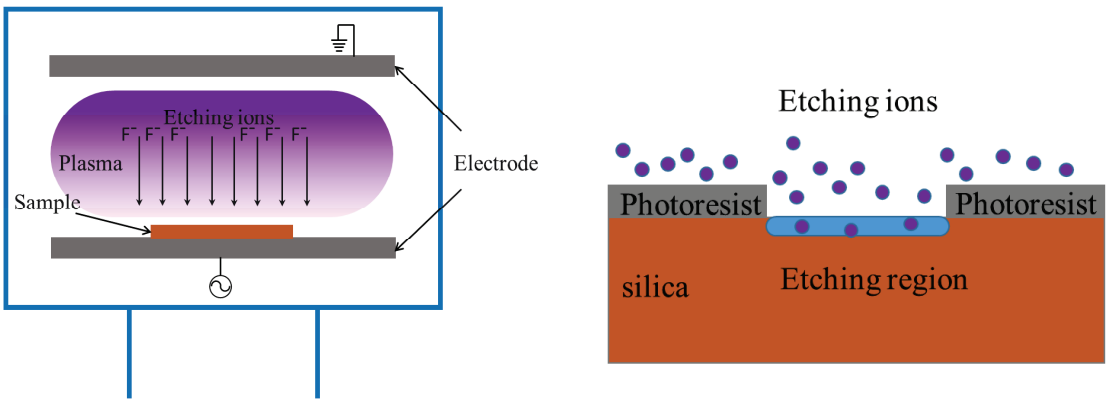

(a) Generation of etching ions (b) Anisotropic etching process

Figure 2.10: Schematic illustration of the working principle of RIE.

Indeed, most of the time silica is used as a hard mask to further etch silicon. An etching recipe with the gas mixture of $CHF_3/SF_6/O_2$ is developed to reduce the surface roughness [24]. The anisotropic etching mechanism is based upon an ion-enhanced inhibitor etching process. This mechanism requires three ingredients: reactive neutral species, inhibitor film forming species, and vertical ion flux to the substrate to prevent growth or etch the inhibitor at the horizontal surface. This mechanism can be approximately and independently controlled by the three etching gases. SF_6 produces

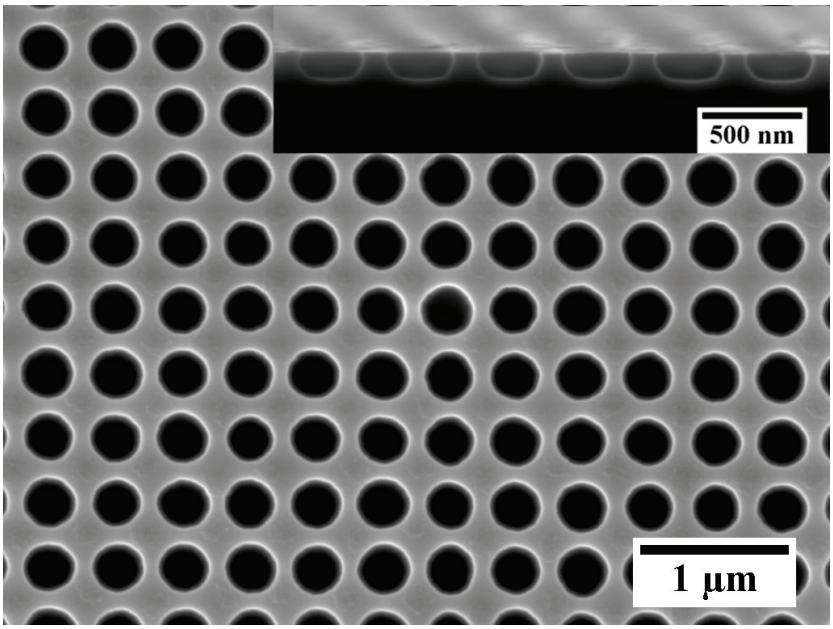

Figure 2.11: Top view SEM image of RIE etched cylinder and cross-section SEM image of the etched cylinder (inset).

the F radical for the chemical etching of silicon. O_2 creates the O radical to passivate the silicon surface by silicon oxide species. CHF_3 produces CF_x ions, in addition to SF_x ions, to surpass the formation of the passivation layer on horizontal surfaces. Because of the hybrid etching mechanism (physical and chemical), the surface roughness is better than pure physical etching (using etchant like Ar). Figure 2.11 shows the optimized etching result. An appropriate mixture of $CHF_3/SF_6/O_2$ (@8/4/12) provides us high homogeneity with anisotropic profile.

2.3.2 Wet etching

Wet etching uses liquid chemicals to remove material from a wafer. Some wet etchants etch crystalline materials at different rates depending on which crystal face is exposed. For this reason, wet etching can be used to form different shapes. The etching patterns are defined by masks on the wafer, crystal face and etchants. In our process, LIL is used to fabricate large-scale two-dimensional patterns that act as the mask. KOH or TMAH are used as etchants to form inverted pyramids on $\langle 100 \rangle$ oriented crystalline silicon substrates. As the etching rate of $\langle 100 \rangle$ plane is much faster than that of $\langle 111 \rangle$ plane. The etched wall is flat and angled. The angle to the surface of the wafer is

54.7° (schematically illustrated in Fig. 2.12). The etched side-wall is on atomic scale smoothness.

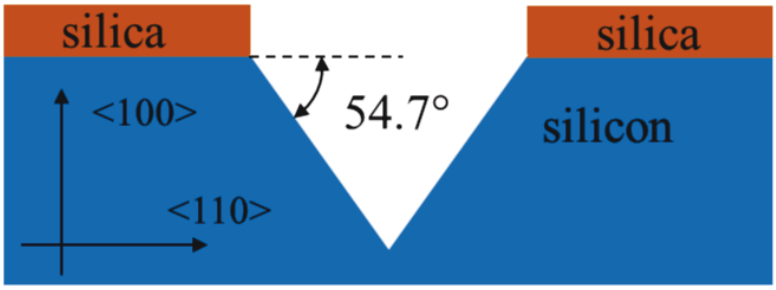

Figure 2.12: Schematic of wet etched pyramid.

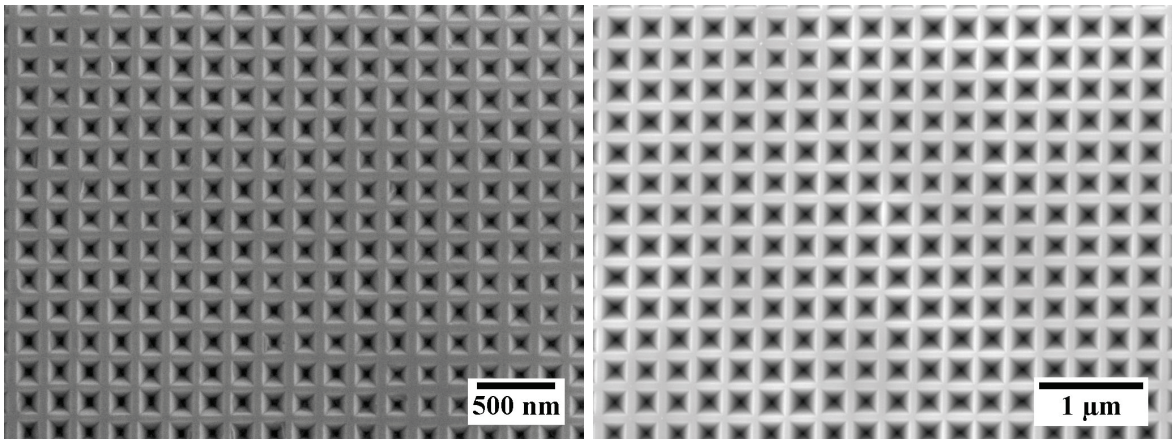

(a) 200 nm (b) 300 nm

(c) 450 nm (d) 600 nm

Figure 2.13: SEM images of the etched inverted pyramids with different periods. (a) 200 nm. (b) 300 nm. (c) 450 nm. (d) 600 nm.

In the etching process, the samples are first patterned using LIL and then etched

through the hard mask (SiO_2) by using RIE, at last, etched with KOH or TMAH at 70 °C to form the inverted pyramids. Compared with KOH, TMAH solution is less aggressive. Especially for TMAH etching, the sample has to be preprocessed to remove the naturally formed SiO_2 on the silicon surface inside the silica mask holes, as a few nanometers of silica could prevent TMAH etching from forming the inverted pyramids. An ultrasonic bath is used to improve the spreading and filling of KOH solution into the silica holes while removing the gas bubbles produced during the etching process. In our process, we have noticed that etching rate was also of the dependence of the etching window (size of the holes). The etching process lasted longer for samples with small etching window than samples with relatively large etching window to get approximately the same filling fraction. Typically, the sizes of etching windows are different for samples with different periods. Inverted pyramids with different periods can be realized by controlling the etching time. As we can see in Fig. 2.13, the inverted pyramids are well formed and have a high degree of uniformity. These images clearly demonstrate the stability and flexibility of our process.

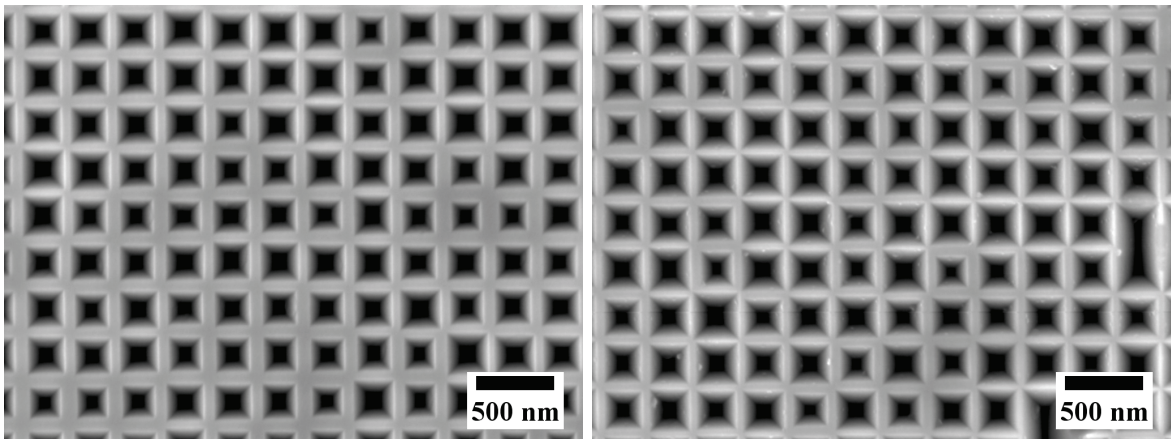

(a) 6 min (b) 8 min

Figure 2.14: SEM images of the etched inverted pyramids with different etching time. The period is 300 nm. (a) 6 min. (b) 8 min.

Even though the proportion of the width and depth of the inverted pyramid is set, the filling fraction of the inverted pyramids on the silicon substrate can still be regulated. Different filling fractions can be realized by simply varying the etching time. As an example, Fig 2.14 shows the realized inverted pyramids with different filling fractions.

We notice that the filling fraction increases with the increase of etching time. Attention has to be paid for long time etching, as we might risk destroying the formed inverted pyramids. We can notice that the inverted pyramids have started to merge with each other for long etching time in Fig 2.14b. The regulation of the filling fraction of inverted pyramids is of importance for the solar cell application as large filling fraction is preferred in this case.

Chapter 3

Periodic Nanostructure Applications

Previously, we described the techniques to pattern substrates with various periods. In this chapter, we focus on the development of different applications based on these periodic structures. In the first section, a porous silicon array with the period of 300 nm on centimeter-scale substrates is fabricated by the combination of LIL and electrochemical etching. Then, in the second section, a preconcentration device based on a one-dimensional periodic structure on the glass substrate is discussed.

3.1 Porous Silicon Fabrication

This section highlights that combining LIL and electrochemical etching (EE) is a cost-effective, efficient method to realize periodic nanopore arrays in silicon with lattice pitch as small as 300 nm on centimeter-scale substrates. The fabrication of wide-area and high aspect ratio 2D pore arrays with 250 nm diameter and 5 μm depth is demonstrated. All the steps of the process have been optimized to achieve vertical sidewalls with 50 nm thickness, providing pore arrays with aspect ratio of 100 on n-type silicon substrates over an area of $2 \times 2\,\mathrm{cm}^2$. These results constitute a technological advance in the realization of ordered pore arrays in silicon with very small lattice parameters, with impact in biotechnology, energy harvesting, or sensors.

3.1.1 Periodic pore arrays

The controlled formation of sub-micrometer nanostructures has been the focus of attention for the last few decades, not only in terms of understanding the fundamental etching or growth mechanisms [25] but also due to their applications in nanoscale electronic and biotechnologies [26]. In particular, silicon pore arrays, an important functional structure, have been thoroughly fabricated and studied at the micrometer scale, for instance in the field of photonics [27], fuel cell [28], microfluidic [29], separation science [30], and templates to form arrays of nanowires [31]. Among them, some applications may need to further increase density of pore arrays such as microfluidic and templates, thus it becomes necessary to scale down pore arrays. Furthermore, new applications might emerge in that scale [26].

EE is a deep-etching technique that has attracted considerable attention since the pioneer works of Lehmann [25, 32], due to its low cost, its simplicity of implementation and its ability to form high aspect ratio silicon microstructures. Continuous efforts have been made in this field to fabricate high aspect ratio microstructures such as pores, trenches, pillars and tubes [33–38]. For more than a decade, ordered macropore formation has been limited to lattice parameters above 500 nm [39]. More recently, we have also fabricated periodic pore arrays with a period of 500 nm using nanoimprint lithography to realize the etching mask; furthermore, we theoretically demonstrated the possibility of forming pore arrays with a period down to 300 nm [40].

In this section, we discuss the successful fabrication of ordered pore arrays in silicon with lattice period as small as 300 nm and a depth up to 5 µm, hence demonstrating that the technological limitations can be overcome for the realization of silicon macropore arrays with very small lattice parameters using EE. This result also validates the theoretical discussion presented in our previous publication [40]. Compared with our previous experimental results (period: 500 nm, pore density: 4 pores/μm^2), this achievement enables to nearly half-reduce the period, while the pore density is more than doubled (pores density: more than 10 pores/μm^2). Our approach is based on the combination of LIL, anisotropic wet etching and EE. The technological advance lies in very accurate optimization of the parameters in both the LIL and the etching

processes to fabricate inverted nanopyramids on a centimeter scale substrate, as well as in adapting them to low-resistivity silicon to ensure a stable pore growth in EE process.

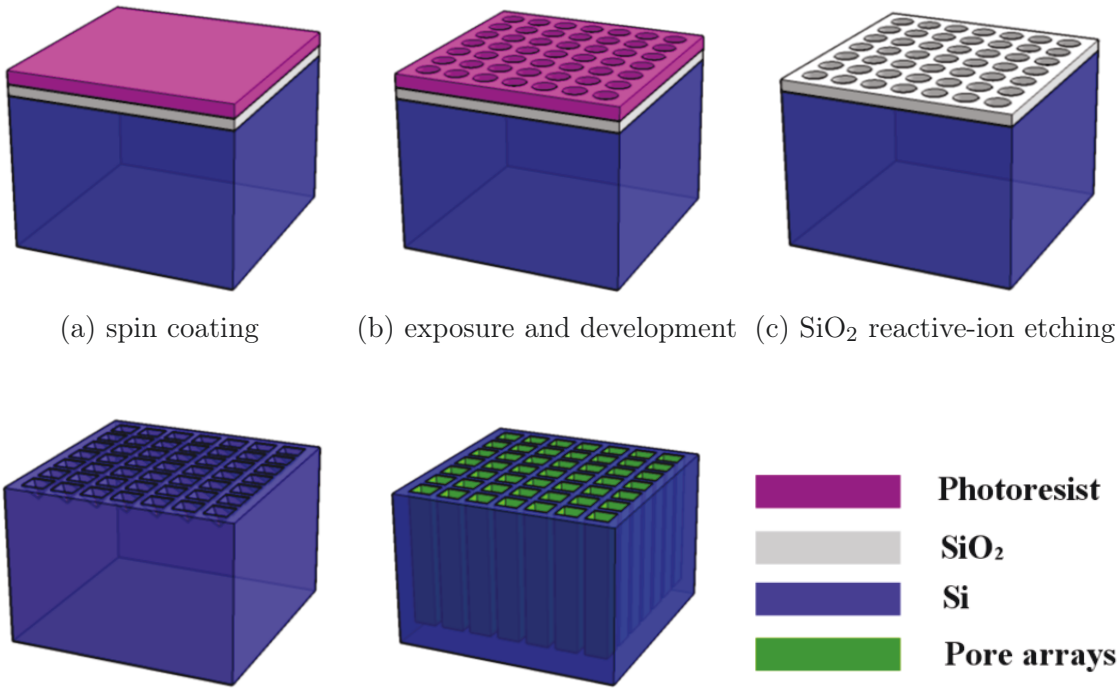

(a) spin coating (b) exposure and development (c) SiO_2 reactive-ion etching

(d) Si wet etching (e) Si electrochemical etching

Figure 3.1: Schematic illustration of fabrication process of silicon pore arrays: (a) Spin coating of a negative-tone photoresist layer on the silicon dioxide side. (b) Double exposure using laser interference lithography, and development. (c) Dry etching by RIE with CHF_3/Ar plasma. (d) KOH wet etching to fabricate inverted nanopyramid. (e) Electrochemical etching to form pore arrays on n-type silicon.

3.1.2 Fabrication procedure

The fabrication procedure is schematically illustrated in Fig. 3.1 and consists in four main steps: LIL, pattern transfer into a silica mask, formation of the nanopyramids by anisotropic wet etching, and EE. The key parameter that dominates the whole process optimization is the uniformity: high uniformity of the inverted pyramids is absolutely crucial for a successful etching of the pore arrays by EE, which means that the preceding process steps have been carefully and interactively optimized in order to obtain the smallest and the most uniform holes as possible in the silica mask. Each step optimization is discussed in the following.

3.1.3 Laser interference lithography process

LIL is employed as a high-resolution, high-throughput and low-cost tool for the fabrication of large-scale patterns with tunable lattice constants [11, 41]. We have highlighted successful realizations of photonic crystals in the photovoltaic area [42, 43] and of finite grating couplers [44] using this technique. A single exposure by LIL gives fringes with a spatial period $\Lambda = \lambda/2\sin(\theta)$, where λ is the wavelength of the laser and θ is the half-angle between the two interfering beams. Our setup is based on a Lloyd's mirror interferometer and uses a semiconductor laser ($\lambda = 266$ nm) as a light source. The periodicity of the pattern can be adjusted from 150 nm to 700 nm (as shown in Fig. 2.7). Circular holes can be generated by two consecutive exposures in negative-tone photoresist with a sample rotation by 90° between the two exposures. A detailed explanation can be found in Chapter 2.

In our LIL process, the negative-tone photoresist (NEB 22) was spin-coated and then baked on ⟨100⟩ oriented n-type silicon substrates with a resistivity of 100 m$\Omega \cdot$cm. Prior to resist spin coating, a 100 nm thick silicon dioxide layer was deposited by pulsed plasma enhanced chemical vapor deposition. Both the silicon resistivity and the deposited silicon dioxide layer have been carefully selected to guarantee the accomplishment of the EE process, which has been systemically demonstrated in reference [40]. Next, the sample was exposed twice to form a 2D array of circular holes (Fig. 3.1b). In order to reach a period of 300 nm, the angle of incidence was adjusted to 26.3°. Figure 3.2a shows the SEM image of the resist pattern having the 300 nm period. The holes in the resist pattern show a good uniformity, which is crucial for subsequent formation of a uniform silicon pore array. Looking into the details of individual holes shown in Fig. 3.2b, a small ring can be observed inside each hole: this vertical radius variation is generated by the vertical standing wave in the LIL exposure process. This phenomenon can be eliminated by using anti-reflective coating [10]. Our approach is simpler, as the next process step, RIE, is a way to economically and efficiently eliminate the vertical radius variation resulting from the standing-wave effect, as discussed in the following.

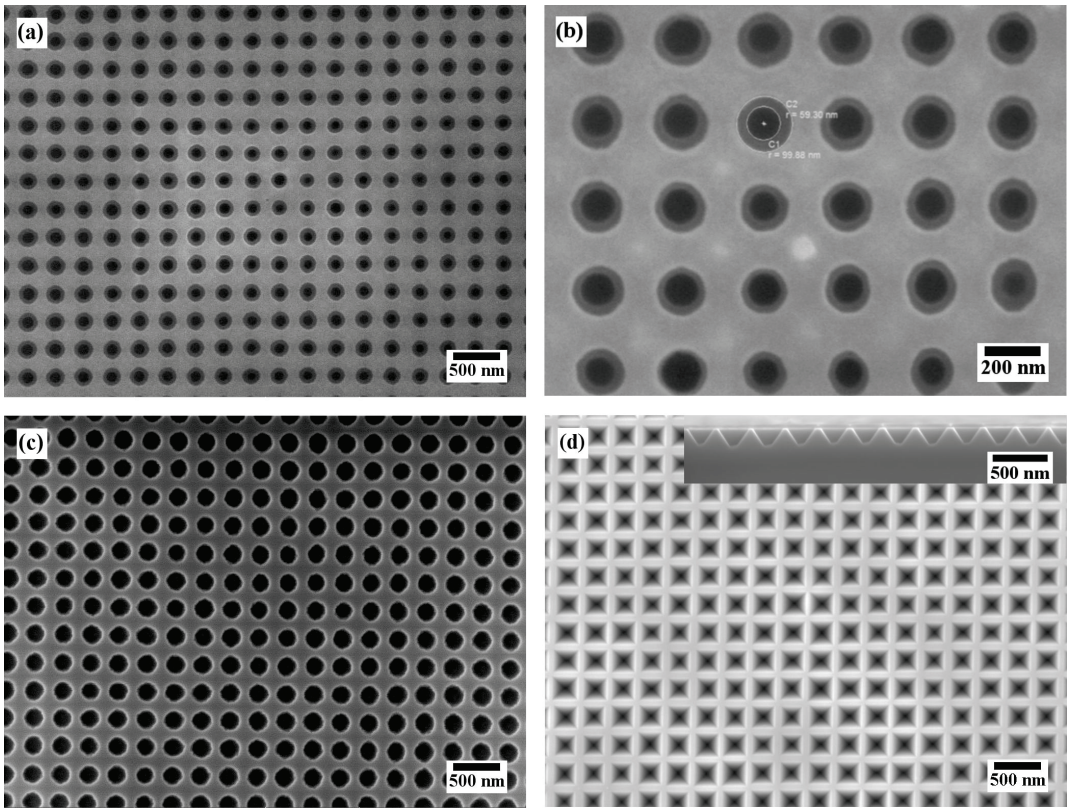

Figure 3.2: (a) Low-magnification SEM image of developed negative photoresist with a period of 300 nm. (b) High-magnification SEM image of developed negative photoresist. (c) SEM image of SiO_2 hard mask. (d) Top view SEM image of inverted pyramids and cross-section SEM image of the pyramids (inset).

3.1.4 Reactive-ion etching

The polymer pattern generated by LIL served as etching mask for RIE transfer into the SiO_2 layer. Before the silica etching process, a short O_2 plasma etching ($\sim$ 15 s, 60 W and 15 mTorr) was applied to remove the residual photoresist at the bottom of the holes and to smooth the inner wall of the holes. As the objective is to obtain homogeneous holes in the silica layer with the smallest possible diameter in order to achieve the highest homogeneity of pore array, the LIL process has been carefully optimized. In particular, the exposure time has been tuned to achieve the smallest possible hole diameter that could be efficiently developed without leaving any extra residual resist that could lead to inhomogeneity during RIE transfer.

RIE was used to pattern the SiO_2 hard mask with a CHF_3/Ar mixture (Fig. 3.1c), and the remaining resist was removed after pattern transfer by subsequent O_2 plasma

etching. After careful optimization of the pattern transfer, the power and pressure of the RIE process have been selected at 60 W and 15 mTorr (self-bias voltage: $\sim$ 120 V), respectively, in order to obtain a very "soft" process yielding a high etching selectivity between silicon oxide and photoresist as well as a good preservation of the hole size. Figure 3.2c shows SEM images of the patterns transferred into the SiO_2 mask. It can be observed that the pattern uniformity remains very high. A statistical [45] study of the hole patterns performed on the same samples before and after RIE etching highlights that the RIE etching process still induces a slight enlargement of the holes diameter while the uniformity is improved. As demonstrated in Fig. 3.3, the mean diameter of the holes after the LIL and after the RIE etching steps are respectively about 89 ± 7 nm and 92 ± 5 nm. A detailed explanation of the statistical analysis is done in Appendix A. The main reason for the uniformity improvement is the smoothing, via the RIE process (O_2 and CHF_3/Ar), of the vertical radius variation in the initial photoresist pattern, which resulted from the vertical standing wave generated in the LIL process.

3.1.5 KOH etching

After RIE, the next process step is anisotropic KOH wet chemical etching in order to form inverted pyramid structures into the silicon substrate (Fig. 3.1d). The etching solution used in this work is typically a 32 wt% KOH solution heated at 70 °C. Fabrication of inverted pyramid arrays with periodicities below 300 nm is very challenging because of the low wettability of the KOH solution, which hinders the penetration of the solution through the small silica holes. This technological hurdle cannot be overcome by an increase of the hole diameter, because the undercutting occurring during the etching step can exfoliate the hard mask or induce the merging of neighboring pyramids that would destroy the periodicity of the pattern.

One of the successfully solutions turned out to be the use of an ultrasonic bath to improve the spreading/ filling of KOH solution into the silica holes while removing the gas bubbles produced during the etching process that could prevent the etching. This procedure enables to achieve complete pyramid formation within 8 min for the 300 nm lattice, which is much slower than in the case of a 500 nm square lattice, where an

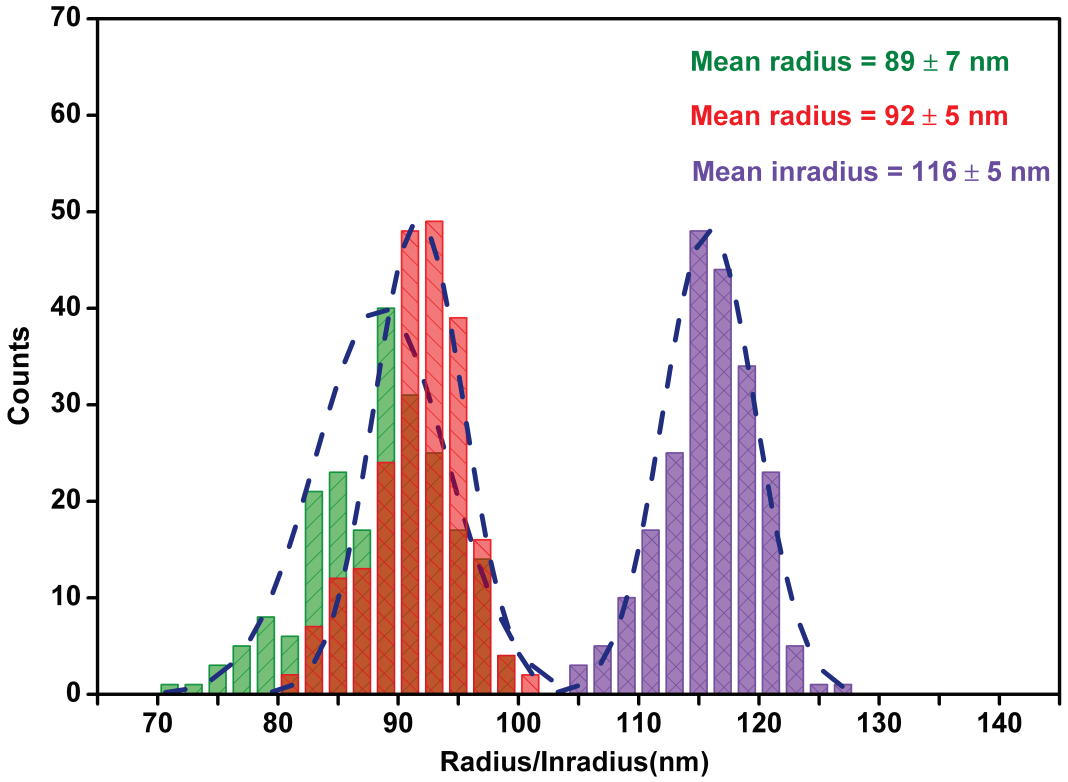

Figure 3.3: Size distributions histogram and corresponding average hole sizes for substrate before (green) after (red) RIE and after (purple) KOH etching. The size distribution functions from Gauss-fit are included for each sample.

etching time of 3 min is sufficient; this large difference highlights the difficulties arising with smaller periods. Figure 3.2d shows SEM images of the resulting inverted pyramids having an inradius of 116 ± 5 nm, obtained on the same sample as in Fig. 3.2a and 3.2b. It can be observed that all the pyramids are well-defined and centered without showing any merging between neighbors. The side view image in Fig. 3.2d (inset) clearly shows all the inverted pyramids are completely formed. Statistically, we can notice that the uniformity of the pattern is increased (Fig. 3.3). This can be explained by the fact that the size of the pyramids does not vary anymore once it is completely formed due to the high anisotropy of the etching velocity in the two different crystallographic directions [46]. This means that, even if the formation of all the pyramids does not start at the same time, the sample stay a sufficient long time in the KOH solution to achieve the formation of all of the pyramids with a uniformity that directly depends on the initial silica mask.

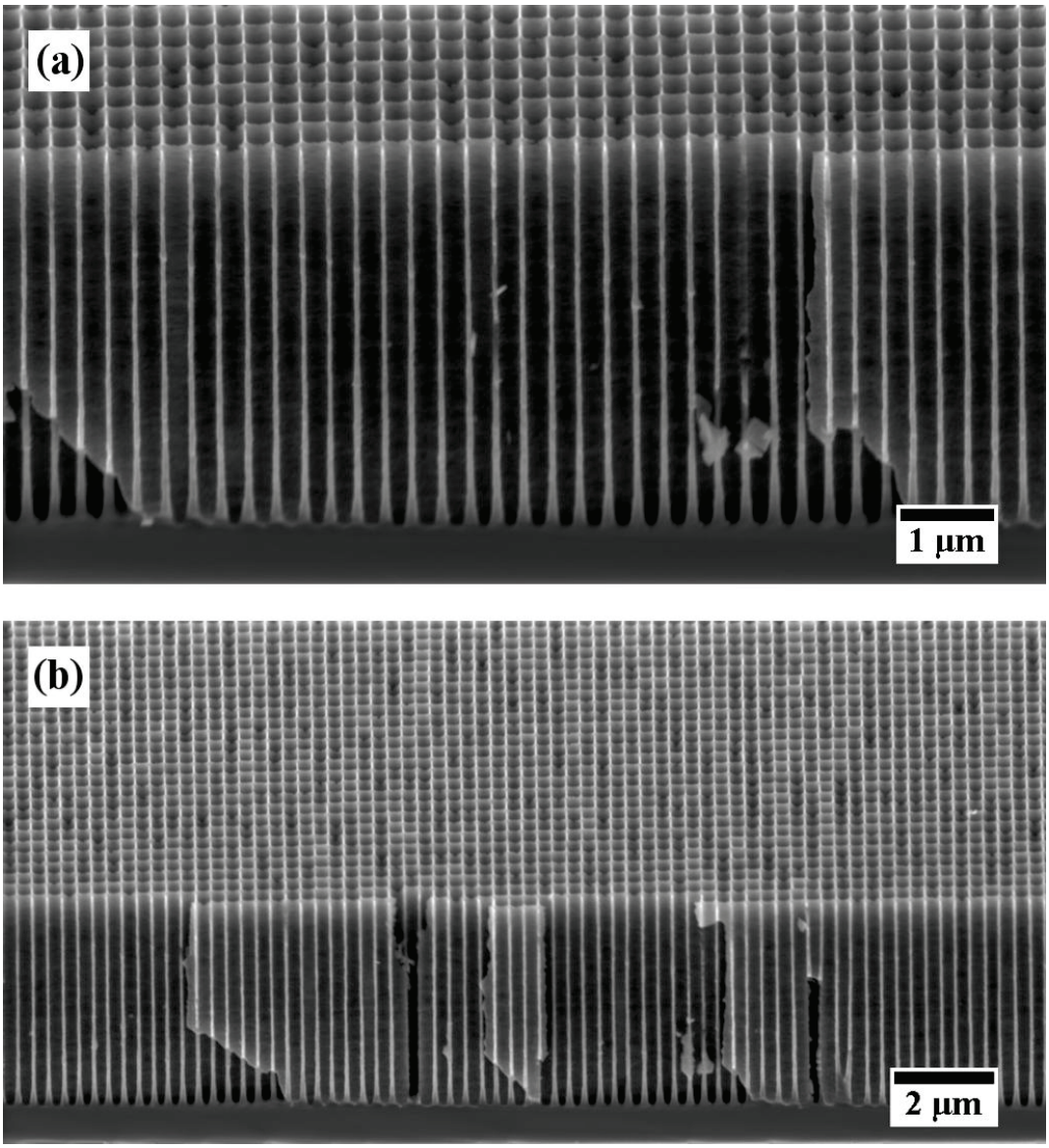

Figure 3.4: (a) High-magnification cross-sectional SEM image of silicon pore arrays. (b) Low-magnification cross-sectional SEM image of silicon pore arrays.

3.1.6 Electrochemical etching

After these preliminary process steps, the last process is the formation of high aspect ratio pore arrays which is carried out by photo electrochemical etching in a HF-containing electrolyte (Fig. 3.1e). Briefly, it is commonly accepted that the high aspect ratio structure formation is ascribed to the deviation of the etching current lines by the electrical field in the space charge region [38]. The size of the structures is then intimately linked to the silicon resistivity and the applied voltage [47]. As already

shown in our previous work [40], in the case of our BHF electrolyte, the minimum pore diameter d_m is linked to the silicon resistivity ρ by the following empirical relation $d_m \approx 450\rho + 200$. However the minimum resistivity is limited to approximately 75 $m\Omega \cdot cm$ due to breakdown phenomena. This means that the minimum pore diameter is around 250 nm. The challenge of our work is the experimental demonstration of this limit with a period of 300 nm. Fig. 3.4a shows SEM images of the formed pores arrays using the following parameters: (i) bath composition: H_2O : Ethanol : BHF (Merck-Ammonium fluoride etchant AF 87.5–12.5) / 30:10:1, (ii) etching parameters: 3.5 V applied voltage, 4.5 mA/cm^2 etching current density, 15 °C bath temperature, 1800 s etching time. Typical depth is about 5 µm and the diameter is about 250 nm. Figure 3.4b illustrates a large area of the sample, which clearly shows the high uniformity of the silicon macropores.

3.1.7 Summary

In summary, we have presented an effective and reliable approach for the preparation of large-scale and periodic nanopore arrays. The combination of LIL, RIE, wet-chemical etching, and EE allows for the highly-homogeneous formation of micrometer-deep pores with periodicity as low as 300 nm. It is important to point out that the 300 nm period demonstrated here is probably not an actual limit. However, as highlighted in the manuscript, further reduction of the period and pore diameter would require intensive re-optimization of all process steps. In particular, the electrolyte composition is crucial to restrict the electrochemical dissolution at the pore tips in order to narrow down the pores. For instance, our preliminary studies indicate that adding a cationic surfactant such as cetyltrimethylammonium chloride helps further reducing the pore diameter [48].

3.2 Preconcentration Chip

In this section, we explore the use of one-dimensional structures in micro- and nanofluidics. Here we introduce a simple, rapid prototyping and low-cost preconcentration chip based on Ion Concentration Polarization (ICP) phenomenon. The preconcentration

chip consists of two microchannels bridged by some nanochannels acting as a robust nanofluidic filter. The nanochannels and microchannels are fabricated separately with LIL and xurography. By integrating these two economic and high-throughput techniques, the LIL based ICP preconcentrator realized a preconcentration factor of 1600 in 8 min.

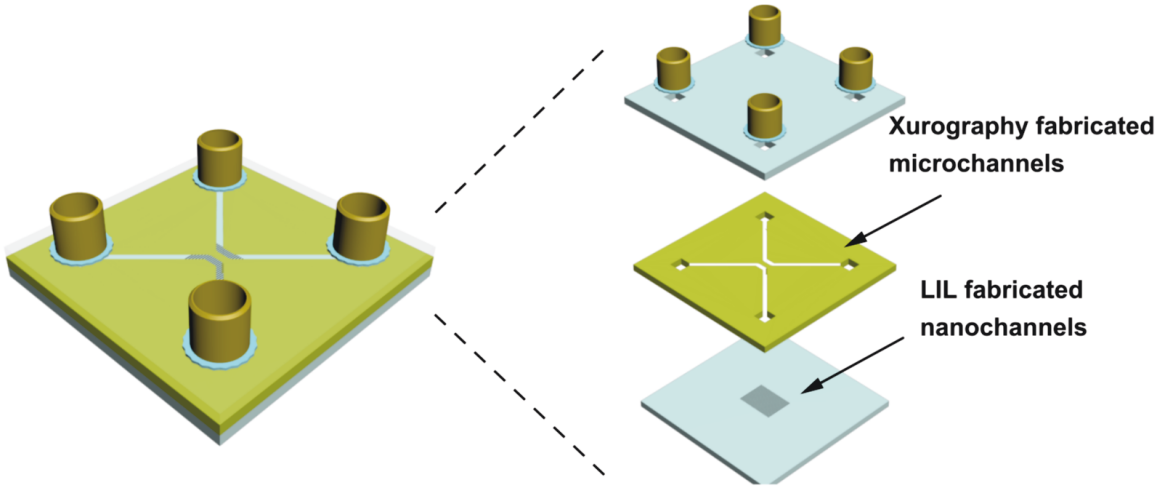

Figure 3.5: Schematic of the preconcentration chip. It is composed by three layers. From top to bottom, the second layer is fabricated by xurography and the third layer is patterned with nanochannels by LIL.

3.2.1 Preconcentrator

Low concentration biomolecule detection is a major issue in biosensing [49]. One of the successful strategies to traverse the detection limit is to concentrate the low-abundance molecules [50]. Also, the preconcentration is even more important in microfluidic sensing systems because of the inherently small channel size, which leads to inefficient use of available target molecules in the samples [51]. Several excellent efforts have been committed to solving the problem, such as field-amplified sample stacking [52], isotachophoresis [53], membrane preconcentration [54], ICP [55, 56], etc. Our preconcentration scheme is based on ICP phenomenon, which could guide any charged biomolecules in the electrolyte to a given location and separate them without suffering from clogging.

In this section, we present a simple and low-cost prototyping technique based on ICP phenomenon by combining LIL and xurography [57, 58]. Figure 3.5 schematically

illustrates the sandwich-structured chip layout. The first and third layers are made of glass slides, and the middle layer is made of a patterned double face self-adhesive film. LIL was employed to etch nanochannels on one of the two glass slides. Xurography was used to cut the pre-designed pattern on the adhesive film. The combination of these two low-cost and high-throughput techniques helps reducing the device cost. Even though low-cost fabrication techniques were adopted, the fabricated prototype still realized a preconcentration factor as high as 1600 in 8 min.

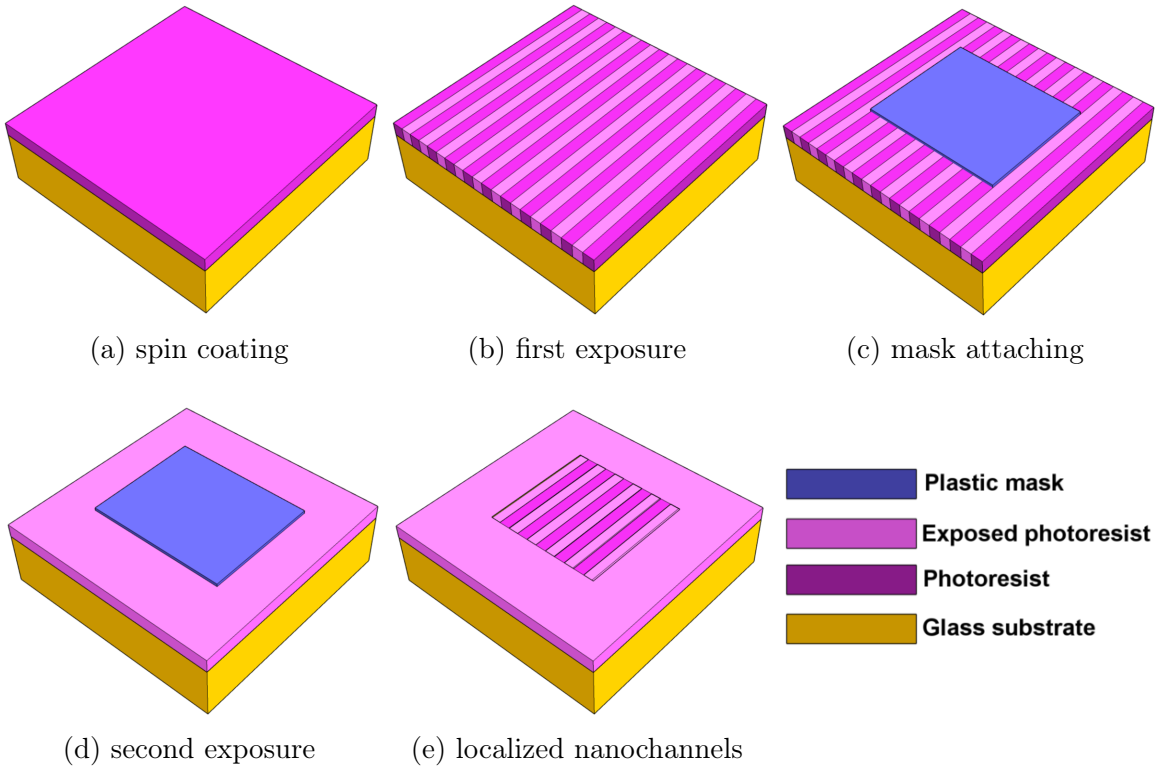

(a) spin coating (b) first exposure (c) mask attaching

(d) second exposure (e) localized nanochannels

Figure 3.6: Schematic illustration of fabrication process of localized nanochannels: (a) Spin coating of a negative-tone photoresist layer on a glass substrate. (b) First exposure using laser interference lithography. (c) Plastic mask attaching. (d) Second exposure of the whole sample. (e) Formation of localized nanochannels on the photoresist.

3.2.2 Chip fabrication

The two essential parts of the device, nanochannels and microchannels were fabricated respectively by LIL and xurography. In the LIL process, a glass substrate (25 mm × 25 mm × 1 mm, Duscher, France) was cleaned and spin-coated the same way as stated in the section 3.1.3. Then the sample was exposed twice to realize localized nanochannels,

as shown in Fig 3.6. The first exposure patterned the sample with one-dimensional structures on the whole sample, and then a pre-fabricated plastic mask was used to cover the desired structured area to execute the second exposure. As the negative-tone photoresist was used, the fabricated nanochannels were only shown in the middle square area. Figure 3.7a shows the fabricated nanochannels on the photoresist. As we can see, we obtained homogeneous nanochannels on the glass substrate. Then, RIE was used to transfer the pattern into the glass substrate with a CHF_3/Ar mixture, and the remaining resist was removed after pattern transfer process subsequently by O_2 plasma etching (Fig. 3.7b). The prepared sample shows high homogeneity, which guarantees the success of preconcentration process. Note that different periods and etching depths can be realized thanks to the flexibility of LIL and etching technique, as stated in section 2.3.1.

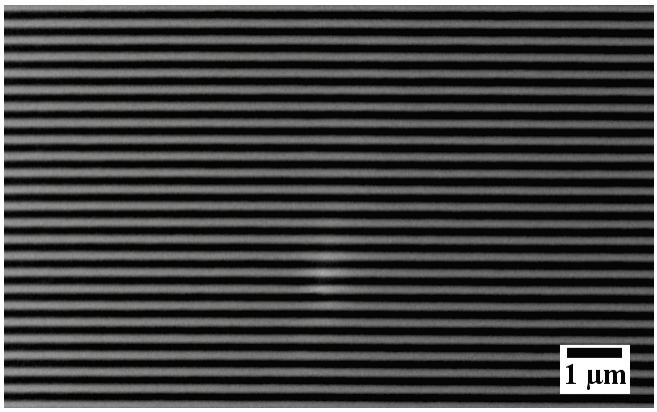

(a) on the photoresist

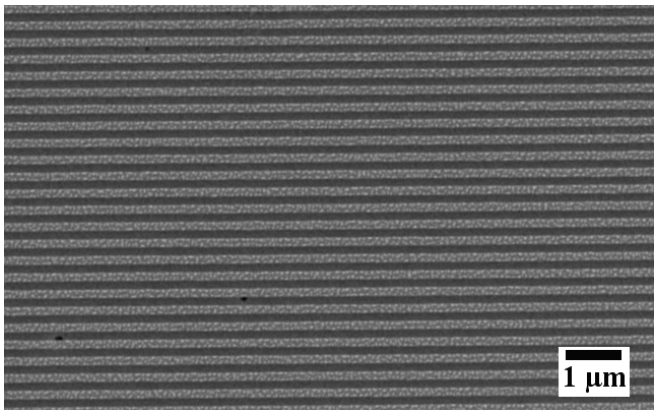

(b) on the glass substrate

Figure 3.7: SEM images of the fabricated nanochannels (a) on the photoresist (b) on the glass substrate.

In the xurography process, a robotic cutting plotter (CE5000-40-CRP, American) was used to cut user-defined features into an 110 µm thick double face self-adhesive film (Plusform, Germany; Tesa, Germany). The design was created with its software package (CoreDRAW Graphic Suite X4). The width of microchannels was set to be 600 µm.

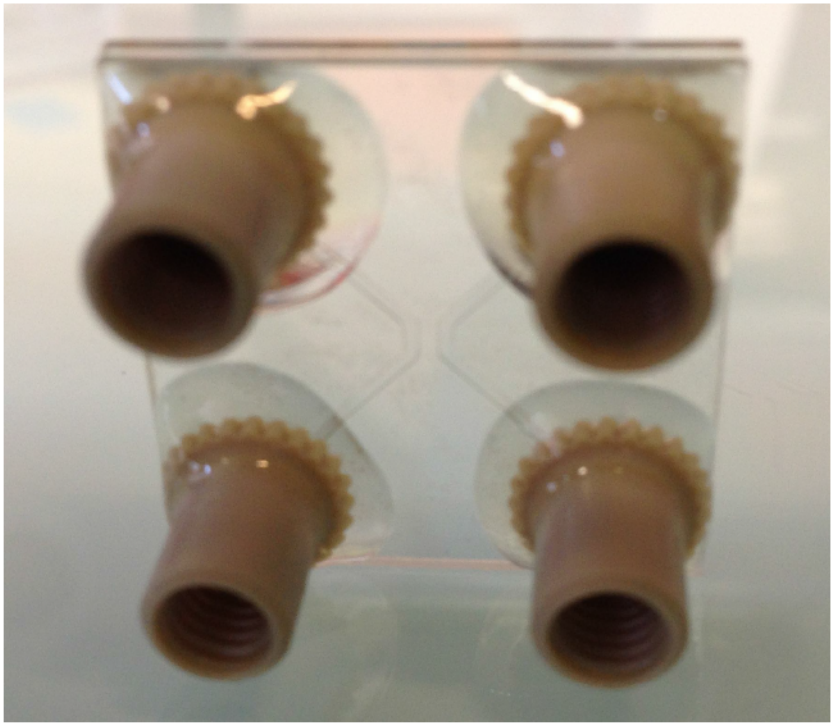

Figure 3.8: Photo of the fabricated preconcentrator chip.

The prepared two glass slides and patterned double face adhesive film were combined by using a press machine at 7 bar. Four NanoPorts (N-333-01 IDEX Health&Science) used as reservoirs were aligned and glued to the four drilled holes on the top of the glass slide. The preconcentration chip was finalized by placing four platinum wires (1 mm in diameter, GoodFellow, Huntingdon, U.K.) as electrodes into the four fluidic reservoirs. The overall dimensions of the device are 25 mm × 25 mm × 2 mm. Each microchannel has an inlet and an outlet to facilitate the electrolyte filling process. Figure 3.8 shows the final device.

3.2.3 Experimental and measurement preparation

For perconcentration experiments, fluorescein (Sigma-Aldrich, St. Quentin Fallavier, excitation at 494 nm and emission at 521 nm, pH dependent, negatively charged) and

KCl electrolyte were used as the tracer and bulk solution, respectively. The pH of KCl buffer solution was fixed at 5 to control experimental environment and the glass surface charge density.

Before starting the measurement, the preconcentrator was washed with DI water. The mixed solution was injected into microchannels. A source meter (Keithley 2400) was used to apply electrical potential through the Pt electrodes on both ends of the microchannels. For the quantification, fluorescent images of preconcentration phenomenon were captured by a CCD camera (12 bits, DFC340 FX, Leica) combined with an inverted microscope (Leica DMI4000 B) equipped with a mercury short arc lamp (HBO 103 W/2, OSRAM). The images were analyzed by ImageJ software [45] to calculate the concentration of fluorescein. The quantified relationship between the gray levels and concentrations of fluorescein had been pre-calibrated. The detailed experiment process can be found in our partner's previous publication [56].

3.2.4 Results and discussion

Figure 3.9 shows a schematic diagram of the ICP-based preconcentrator. When an electric field is applied to the preconcentrator, more cations than anions will migrate across the nanochannels (Fig. 3.9a). It results in net transfer of charges from the high-potential side to the low-potential side, and the concentration near the high-potential side of nanochannels will decrease due to the concentration polarization effect [59]. Since a little amount of liquid generated by electroosmotic flow in the microchannel is allowed to pass through the nanochannels, a backflow, namely feedback pressure driven flow, is generated on both sides [60], which leads to a circulation flow in the microchannel (Fig. 3.9b). Additionally, in the depletion region, the electric field as well as the electrophoretic velocity increase, since the electrical resistance is inversely proportional to the ion concentration. As a result, the negatively charged biomolecules will be trapped in a particular region where the convection and migration force is balanced (Fig. 3.9c). A more detailed explanation can be found in reference [56].

Figure 3.10 demonstrates the performance of the preconcentration device over 400 seconds. As we can see, the fluorescein concentrates on both sides of the high-potential

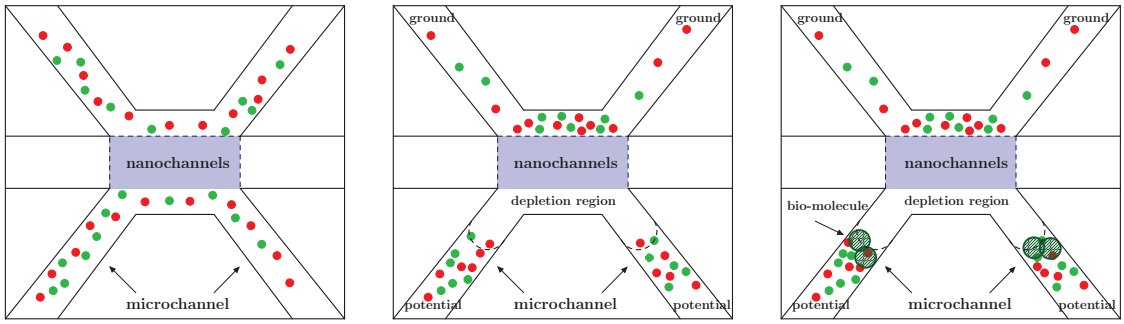

(a) Initial state (b) Electrical potential applied (c) Biomolecules trapping

Figure 3.9: Schematic diagram of the preconcentration device and sepration process.

microchannel side. The U-shape fluorescence is caused by the force balance that we stated previously. Figure 3.10b shows the accumulation process of the fluorescein over time on the right branch of high-potential microchannel side. With the increase of the time, more Fluorescein is trapped until a balance between diffusion and accumulation reaches. Finally, at 400 seconds the overall preconcentration factor reaches 1600.

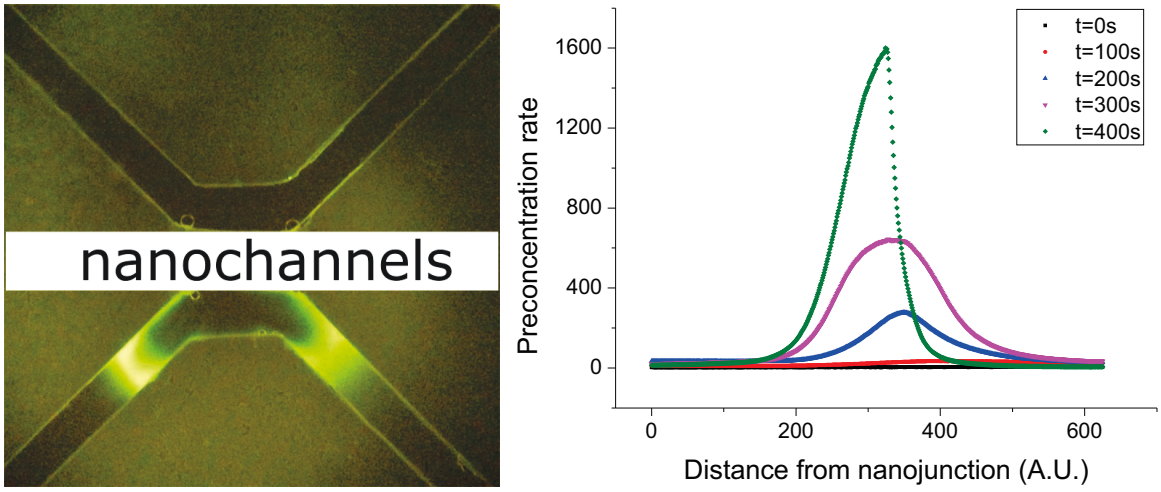

(a) (b)

Figure 3.10: (a) Image of the trapped fluorescein at 400 s. (b) Experimental result of the preconcentration device over 400 s.

Apart from other preconcentrators in the literature, the advantage of using LIL is that the dimensions of the nanochannels could be easily controlled. Based on that, we could easily analyze the size effect of nanochannels to perconcentrator and improve the performance of the chip. Theoretically, nanochannels with smaller size might improve the performance of the chip. However, due to the elasticity of the self-adhesive film,

more diminutive nanochannels might be blocked (e.g. nanochannels with the etching depths of 25 nm and 50 nm). Our experiments for shallower nanochannels ended up failure. We believe that the improvement of bonding technique could further improve the performance of the device.

3.2.5 Summary

In this work, we have developed a simple, rapid prototyping and low-cost biomolecule preconcentration chip by combining LIL and xurography. Despite its limitation in resolution, our device could be attractive for fabricating low-priced biomolecule preconcentration chip. Also, by improving the bonding technique, the device performance could be further improved.

Chapter 4

Periodic Structure and Rigorous Coupled Wave Analysis

In this section, we consider the optical properties of periodic structures. Previously, we described the fast and economic lab-scale fabrication method named LIL. Even though this approach enables us to efficiently fabricate periodic structures, numerical methods still are needed to accelerate the exploration of their optical properties. In this part, a rigorous electromagnetic calculation method is introduced. With the consideration of the primary attribute of our problem, periodicity, a Fourier-based method seems to be the most appropriate choice. In the domain of electromagnetic calculation, the Fourier-based numerical method named Rigorous Coupled-Wave Analysis (RCWA) also known as Fourier Modal Method (FMM), is developed to solved the problem. It is unconditionally stable, full vector, and rigorous in the sense that no approximation is made to Maxwell's equations. We will explore this numerical method for analyzing the optical properties of our periodic structures.

4.1 Rigorous Coupled Wave Analysis

RCWA is an eigenmode expansion method that was originally developed to study optical diffraction efficiencies from volume holographic or surface relief grating [61, 62]. The first stable RCWA method for one-dimensional multilayer gratings was formulated by

Moharam and Gaylord [63]. The extension to two-dimensional structures occurred later with improved computational power and numerical algorithms [64–68] The basic idea of RCWA is to expand the electromagnetic field within each layer into reciprocal space representing by a sum of spatial harmonics. This transforms the wave equation into a set of ordinary differential equations which is then solved as an eigenvalue problem. The eigenvalue and eigenvector separately characterize the propagation and configuration of the spatial harmonics in each layer. The modal expansion coefficients are then related by matching tangential field at the interfaces. As such, structures that are periodic in two dimensions, and piecewise constant in the third, are best suited for analyzing. Figure 4.1 shows an example of such a geometrical construction.

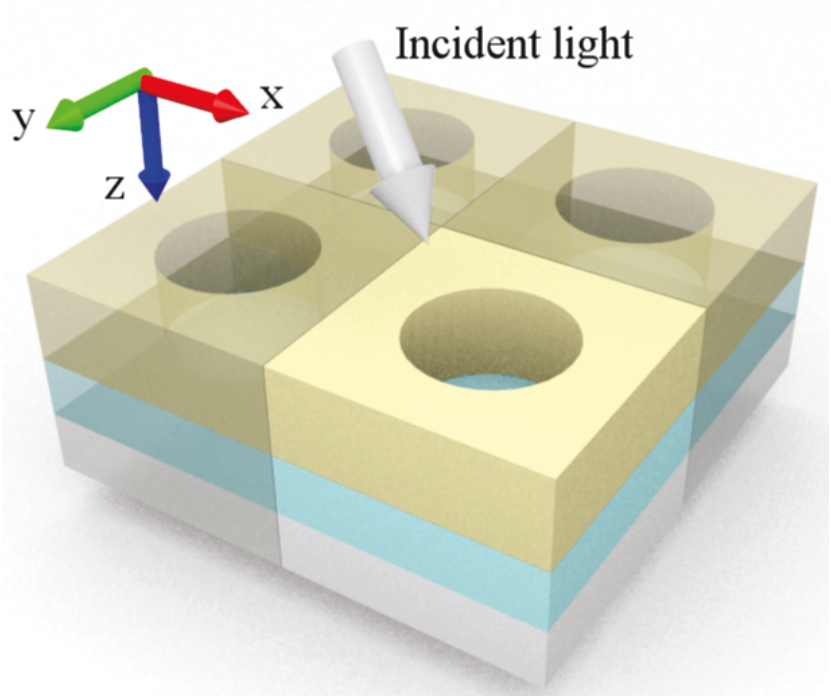

Figure 4.1: Schematic of an typical multilayer stack of two-dimensional periodic structure simulated in RCWA.

Being a semi-analytical method where the wave equation is treated analytically in the longitudinal direction, this approach can model structures of arbitrary length without increasing simulation time. Arbitrarily shaped devices are handled by using staircase approximation to resolve them with many thin layers. However, the RCWA method is best suited to analyze structures with minimal complexity in the z-direction. For

slowly varied structures in the z-direction, the calculation can become computationally intensive because of the increasing number of layers under staircase approximation.

As described above, structures that can be well described by a few number of Fourier components are suitable for the RCWA method due to the eigenmode computation in each layer. For this reason, low to moderate index contrast media can be accurately analyzed. When dealing with high contrast index such as the metallic grating, RCWA suffers from slow convergence, especially under transverse magnetic (TM) polarization [69]. Because many Fourier components are required to describe accurately the structure and field. Lalanne had first proposed a solution to tackle the problem [70]. Lifeng Li identified the actual mathematical problem [71]. Then, several different approaches based on Fast Fourier Factorization (FFF) methods have been proposed [72–74]. Although the FFF can effectively improve the convergence for high contrast index, the use of FFF is beyond the scope of the thesis since we only focus on low to moderate index materials.

In the following sections, we will describe in detail the derivation and implementation of RCWA and then validate the implemented code.

4.2 Geometric Definitions

The coordinate system is oriented such that the z-axis is normal to the layers of a structure, and the structure is assumed to be periodic in the xy-plane, as shown in Fig 4.1. The plane wave source illuminates the structure from the top with arbitrary angles. It is placed in the zeroth layer, where is the reflection region. Then the whole structure is constructed layer by layer beneath the source. Each layer in the structure is assume invariant in the z-direction, as such complex structures could be naturally separated. For some pieces of the structure with the same material but varies in the z-direction, a staircase approximation is used.

Typical problems require solving for transmission, reflection, or absorption spectra of structures. The reflection spectra are calculated in the zeroth layer beneath the source. And the transmission spectra are calculated in the transmission layer, where the device resides. The absorption is obtained by using the law of energy conservation.

4.3 Unit and Conventions

To facilitate the discussion, we clarify the conventions we used here.

- A right-handed orthogonal Cartesian coordinate system is used, as shown in Fig. 4.1.
- The sign convention e^{-jkz} is adopted to describe a wave propagating in the $+z$-direction.
- The bold letters in equations stand for matrices or column vectors.
- Symbols $\mathbf{I}$ and $\mathbf{0}$ stand for two-dimensional identity and zero matrices, respectively. The size of the matrices would be clear in the context.
- SI units are used throughout.

4.4 Maxwell's Equations in a Layer

4.4.1 Equation normalization

We start from Maxwell's equations for source free materials:

$$\nabla \times \vec{E} = -j\omega\mu_0\mu_r\vec{H} \tag{4.1}$$

$$\nabla \times \vec{H} = j\omega\varepsilon_0\varepsilon_r\vec{E} \tag{4.2}$$

For the sake of simplicity and convenience, we normalize the magnetic field in the following manner (see Eq. 4.3) to bring the electric and magnetic fields onto the same scale, which provides better numerical conditioning in implementation.

$$\vec{\tilde{H}} = -j\sqrt{\frac{\mu_0}{\varepsilon_0}}\vec{H} \tag{4.3}$$

In the new term, Maxwell's equations become

$$\nabla \times \vec{E} = k_0\mu_r\vec{\tilde{H}} \tag{4.4}$$

$$\nabla \times \vec{\tilde{H}} = k_0 \varepsilon_r \vec{E} \tag{4.5}$$

where

$$k_0 = \omega \sqrt{\mu_0 \varepsilon_0} \tag{4.6}$$

4.4.2 Fourier expansion

The next step is to take the Fourier transform in x- and y- directions. For a grating layer, the expansions can be written as

$$\vec{E} = \sum_{m=-\infty}^{\infty} \sum_{n=-\infty}^{\infty} S(m,n) e^{-j[k_x(m)x + k_y(n)y]} \tag{4.7}$$

$$\vec{\tilde{H}} = \sum_{m=-\infty}^{\infty} \sum_{n=-\infty}^{\infty} U(m,n) e^{-j[k_x(m)x + k_y(n)y]} \tag{4.8}$$

In a square or rectangular symmetric system, the wave vector components of the spatial harmonics are defined as

$$k_x(m) = k_{x,inc} - m\frac{2\pi}{\Lambda_x} \tag{4.9}$$

$$k_y(n) = k_{y,inc} - n\frac{2\pi}{\Lambda_y} \tag{4.10}$$

In a similar manner, the permittivity and permeability functions can be expanded into Fourier series.

$$\varepsilon_r(x,y) = \sum_{m=-\infty}^{\infty} \sum_{n=-\infty}^{\infty} a_{m,n} e^{j(\frac{2\pi mx}{\Lambda_x} + \frac{2\pi ny}{\Lambda_y})} \tag{4.11}$$

$$\mu_r(x,y) = \sum_{m=-\infty}^{\infty} \sum_{n=-\infty}^{\infty} b_{m,n} e^{j(\frac{2\pi mx}{\Lambda_x} + \frac{2\pi ny}{\Lambda_y})} \tag{4.12}$$

where the Fourier coefficients are calculated as

$$a_{m,n} = \frac{1}{\Lambda_x \Lambda_y} \int_{-\Lambda_x/2}^{\Lambda_x/2} \int_{-\Lambda_y/2}^{\Lambda_y/2} \varepsilon_r(x,y) e^{-j(\frac{2\pi mx}{\Lambda_x} + \frac{2\pi ny}{\Lambda_y})} dxdy \tag{4.13}$$

$$b_{m,n} = \frac{1}{\Lambda_x \Lambda_y} \int_{-\Lambda_x/2}^{\Lambda_x/2} \int_{-\Lambda_y/2}^{\Lambda_y/2} \mu_r(x,y) e^{-j(\frac{2\pi mx}{\Lambda_x} + \frac{2\pi ny}{\Lambda_y})} dxdy \tag{4.14}$$

Using these definitions, each component of Maxwell's equations can be transformed as following:

$$-j\tilde{k}_y(n)U_z(m,n) - \frac{dU_y(m,n)}{d\tilde{z}} = \sum_{p=-\infty}^{\infty}\sum_{q=-\infty}^{\infty} a_{m-p,n-q}S_x(p,q) \tag{4.15}$$

$$\frac{dU_x(m,n)}{d\tilde{z}} + j\tilde{k}_x(m)U_z(m,n) = \sum_{p=-\infty}^{\infty}\sum_{q=-\infty}^{\infty} a_{m-p,n-q}S_y(p,q) \tag{4.16}$$

$$-j\tilde{k}_x(m)U_y(m,n) + j\tilde{k}_y(n)U_x(m,n) = \sum_{p=-\infty}^{\infty}\sum_{q=-\infty}^{\infty} a_{m-p,n-q}S_z(p,q) \tag{4.17}$$

$$-j\tilde{k}_y(n)S_z(m,n) - \frac{dS_y(m,n)}{d\tilde{z}} = \sum_{p=-\infty}^{\infty}\sum_{q=-\infty}^{\infty} b_{m-p,n-q}U_x(p,q) \tag{4.18}$$

$$\frac{dS_x(m,n)}{d\tilde{z}} + j\tilde{k}_x(m)S_z(m,n) = \sum_{p=-\infty}^{\infty}\sum_{q=-\infty}^{\infty} b_{m-p,n-q}U_y(p,q) \tag{4.19}$$

$$-j\tilde{k}_x(m)S_y(m,n) + j\tilde{k}_y(n)S_x(m,n) = \sum_{p=-\infty}^{\infty}\sum_{q=-\infty}^{\infty} b_{m-p,n-q}U_z(p,q) \tag{4.20}$$

where wave vector and distance are normalized as:

$$\tilde{k} = k/k_0 \tag{4.21}$$

$$\tilde{z} = k_0 z \tag{4.22}$$

The set of equations can then be written in matrix form as:

$$-j\tilde{\mathrm{K}}_y\mathbf{U}_z - \frac{d}{d\tilde{z}}\mathbf{U}_y = \boldsymbol{\varepsilon}_r\mathbf{S}_x \tag{4.23}$$

$$\frac{d}{d\tilde{z}}\mathbf{U}_x + j\tilde{\mathbf{K}}_x\mathbf{U}_z = \boldsymbol{\varepsilon}_r\mathbf{S}_y \tag{4.24}$$

$$\tilde{\mathbf{K}}_x\mathbf{U}_y - \tilde{\mathbf{K}}_y\mathbf{U}_x = j\boldsymbol{\varepsilon}_r\mathbf{S}_z \tag{4.25}$$

$$-j\tilde{\mathbf{K}}_y\mathbf{S}_z - \frac{d}{d\tilde{z}}\mathbf{S}_y = \boldsymbol{\mu}_r\mathbf{U}_x \tag{4.26}$$

$$\frac{d}{d\tilde{z}}\mathbf{S}_x + j\tilde{\mathbf{K}}_x\mathbf{S}_z = \boldsymbol{\mu}_r\mathbf{U}_y \tag{4.27}$$

$$\tilde{\mathbf{K}}_x \mathbf{S}_y - \tilde{\mathbf{K}}_y \mathbf{S}_x = j\boldsymbol{\mu}_r \mathbf{U}_z \tag{4.28}$$

We have transformed the Maxwell's Equations into matrix form for a single layer. $\mathbf{S}$ and $\mathbf{U}$ are column vectors presenting complex amplitude coefficients of the truncated spatial harmonics for the electric and magnetic fields. The accuracy of the result is directly connected with the truncation number used in the calculation, which will be discussed later. $\tilde{\mathbf{K}}_x$ and $\tilde{\mathbf{K}}_y$ are diagonal matrices containing wave vector components defined in Eqs. 4.9 and 4.10. The square matrices $\boldsymbol{\mu}_r$ and $\boldsymbol{\varepsilon}_r$ are matrix operator for the convolution operation defined in Eqs. 4.15-4.20. They are constructed by using the Fourier coefficients of the patterned layer. Here we use fast Fourier transform to extract the corresponding Fourier coefficients. Alternatively, an analytical method could also be used to calculate the Fourier coefficients. Compared with analytical method, fast Fourier transform is a general way to solve arbitrary patterned structures. But the analytical solution could be faster in solving regular shaped layers (e.i. circular or rectangular). Regardless of which method we use, the Fourier coefficients can then be used to construct the convolution matrix. The detailed process can be found in Appendix B.

4.4.3 Differential equations

Then we start to form the differential equations for one layer. Eliminating the z components using Eq. 4.25, Eqs. 4.26 and 4.25 become

$$-\tilde{\mathbf{K}}_y \boldsymbol{\varepsilon}_r{}^{-1}(\tilde{\mathbf{K}}_x \mathbf{U}_y - \tilde{\mathbf{K}}_y \mathbf{U}_x) - \frac{d}{d\tilde{z}}\mathbf{S}_y = \boldsymbol{\mu}_r \mathbf{U}_x \tag{4.29}$$

$$\frac{d}{d\tilde{z}}\mathbf{S}_x + \tilde{\mathbf{K}}_x \boldsymbol{\mu}_r{}^{-1}(\tilde{\mathbf{K}}_x \mathbf{U}_y - \tilde{\mathbf{K}}_y \mathbf{U}_x) = \boldsymbol{\mu}_r \mathbf{U}_y \tag{4.30}$$

Or they can be written in block matrix form.

$$\frac{d}{d\tilde{z}}\begin{bmatrix} \mathbf{S}_x \\ \mathbf{S}_y \end{bmatrix} = \mathbf{P}\begin{bmatrix} \mathbf{U}_x \\ \mathbf{U}_y \end{bmatrix} \tag{4.31}$$

$$\mathbf{P} = \begin{bmatrix} \tilde{\mathbf{K}}_x {\varepsilon_r}^{-1} \tilde{\mathbf{K}}_y & \boldsymbol{\mu}_r - \tilde{\mathbf{K}}_x {\varepsilon_r}^{-1} \tilde{\mathbf{K}}_y \\ \tilde{\mathbf{K}}_y {\varepsilon_r}^{-1} \tilde{\mathbf{K}}_y - \boldsymbol{\mu}_r & -\tilde{\mathbf{K}}_y {\varepsilon_r}^{-1} \tilde{\mathbf{K}}_x \end{bmatrix} \tag{4.32}$$

Similarly, eliminating the z components using Eq. 4.28, Eqs. 4.23 and 4.24 become

$$-\tilde{\mathbf{K}}_y {\boldsymbol{\mu}_r}^{-1} (\tilde{\mathbf{K}}_x \mathbf{S}_y - \tilde{\mathbf{K}}_y \mathbf{S}_x) - \frac{d}{d\tilde{z}} \mathbf{U}_y = \varepsilon_r \mathbf{S}_x \tag{4.33}$$

$$\frac{d}{d\tilde{z}} \mathbf{U}_x + \tilde{\mathbf{K}}_x {\boldsymbol{\mu}_r}^{-1} (\tilde{\mathbf{K}}_x \mathbf{S}_y - \tilde{\mathbf{K}}_y \mathbf{S}_x) = \varepsilon_r \mathbf{S}_y \tag{4.34}$$

In block matrix form:

$$\frac{d}{d\tilde{z}} \begin{bmatrix} \mathbf{U}_x \\ \mathbf{U}_y \end{bmatrix} = \mathbf{Q} \begin{bmatrix} \mathbf{S}_x \\ \mathbf{S}_y \end{bmatrix} \tag{4.35}$$

$$\mathbf{Q} = \begin{bmatrix} \tilde{\mathbf{K}}_x {\boldsymbol{\mu}_r}^{-1} \tilde{\mathbf{K}}_y & \varepsilon_r - \tilde{\mathbf{K}}_x {\boldsymbol{\mu}_r}^{-1} \tilde{\mathbf{K}}_y \\ \tilde{\mathbf{K}}_y {\boldsymbol{\mu}_r}^{-1} \tilde{\mathbf{K}}_y - \varepsilon_r & -\tilde{\mathbf{K}}_y {\boldsymbol{\mu}_r}^{-1} \tilde{\mathbf{K}}_x \end{bmatrix} \tag{4.36}$$

From here, we derive our second-order differential semi-analytical wave equation. It is simply done by substituting Eq. 4.31 in Eq. 4.35 . In matrix form, this can be written as

$$\frac{d^2}{d\tilde{z}^2} \begin{bmatrix} \mathbf{S}_x \\ \mathbf{S}_y \end{bmatrix} = \boldsymbol{\Omega}^2 \begin{bmatrix} \mathbf{S}_x \\ \mathbf{S}_y \end{bmatrix} \tag{4.37}$$

where

$$\boldsymbol{\Omega}^2 = \mathbf{PQ} = \begin{bmatrix} \tilde{\mathbf{K}}_x {\varepsilon_r}^{-1} \tilde{\mathbf{K}}_y & \boldsymbol{\mu}_r - \tilde{\mathbf{K}}_x {\varepsilon_r}^{-1} \tilde{\mathbf{K}}_y \\ \tilde{\mathbf{K}}_y {\varepsilon_r}^{-1} \tilde{\mathbf{K}}_y - \boldsymbol{\mu}_r & -\tilde{\mathbf{K}}_y {\varepsilon_r}^{-1} \tilde{\mathbf{K}}_x \end{bmatrix} \begin{bmatrix} \tilde{\mathbf{K}}_x {\boldsymbol{\mu}_r}^{-1} \tilde{\mathbf{K}}_y & \varepsilon_r - \tilde{\mathbf{K}}_x {\boldsymbol{\mu}_r}^{-1} \tilde{\mathbf{K}}_y \\ \tilde{\mathbf{K}}_y {\boldsymbol{\mu}_r}^{-1} \tilde{\mathbf{K}}_y - \varepsilon_r & -\tilde{\mathbf{K}}_y {\boldsymbol{\mu}_r}^{-1} \tilde{\mathbf{K}}_x \end{bmatrix} \tag{4.38}$$

At this point, we have transformed our problem into an analytical problem in matrix form. Obviously, the solution to Eq. 4.37 can be written as:

$$\begin{bmatrix} \mathbf{S}_x \\ \mathbf{S}_y \end{bmatrix} = e^{-\boldsymbol{\Omega}\tilde{z}} \mathbf{S}^+(0) + e^{\boldsymbol{\Omega}\tilde{z}} \mathbf{S}^-(0) \tag{4.39}$$

The first and second terms are proportionality constants corresponding to forward and backward propagating waves. The terms $\mathbf{S}^+(0)$ and $\mathbf{S}^+(0)$ are the initial values for this

differential equation.

The eigenvector and eigenvalue matrices are used to break Eq. 4.39 down to:

$$\begin{bmatrix} \mathbf{S}_x \\ \mathbf{S}_y \end{bmatrix} = \mathbf{W}e^{-\lambda\tilde{z}}\mathbf{W}^{-1}\mathbf{S}^{+}(0) + \mathbf{W}e^{\lambda\tilde{z}}\mathbf{W}^{-1}\mathbf{S}^{-}(0) = \mathbf{W}e^{-\lambda\tilde{z}}\mathbf{C}^{+} + \mathbf{W}e^{\lambda\tilde{z}}\mathbf{C}^{-} \tag{4.40}$$

where $\mathbf{W}$ is the eigenvalue of $\mathbf{\Omega}$, λ is the eigenvector of $\mathbf{\Omega}$ and $\mathbf{C}$ is the product of $\mathbf{W}$ and $\mathbf{S}$.

Similarly, the solution for the magnetic fields can be written as:

$$\begin{bmatrix} \mathbf{U}_x \\ \mathbf{U}_y \end{bmatrix} = -\mathbf{V}e^{-\lambda\tilde{z}}\mathbf{C}^{+} + \mathbf{V}e^{\lambda\tilde{z}}\mathbf{C}^{-} \tag{4.41}$$

To compute $\mathbf{V}$, Eq. 4.41 is differentiated with respect to $\tilde{z}$.

$$\frac{d}{d\tilde{z}}\begin{bmatrix} \mathbf{U}_x \\ \mathbf{U}_y \end{bmatrix} = \mathbf{V}\lambda e^{-\lambda\tilde{z}}\mathbf{C}^{+} + \mathbf{V}\lambda e^{\lambda\tilde{z}}\mathbf{C}^{-} \tag{4.42}$$

Comparing Eqs. 4.42 and 4.35, we get

$$\mathbf{V} = \mathbf{Q}\mathbf{W}\lambda^{-1} \tag{4.43}$$

Then the overall solution for a single layer can be written as:

$$\mathbf{\Psi} = \begin{bmatrix} \mathbf{S}_x \\ \mathbf{S}_y \\ \mathbf{U}_x \\ \mathbf{U}_y \end{bmatrix} = \begin{bmatrix} \mathbf{W} & \mathbf{W} \\ -\mathbf{V} & \mathbf{V} \end{bmatrix}\begin{bmatrix} e^{-\lambda\tilde{z}} & \mathbf{0} \\ \mathbf{0} & e^{\lambda\tilde{z}} \end{bmatrix}\begin{bmatrix} \mathbf{C}^{+} \\ \mathbf{C}^{-} \end{bmatrix} \tag{4.44}$$

In this equation, $\mathbf{W}$ describes the eigenmodes of the electric fields and $\mathbf{V}$ describes the eigenmodes of the magnetic fields. The exponential terms represent the forward and backward wave propagations through the respective layer. The column vectors $\mathbf{C}^{+}$ and $\mathbf{C}^{-}$ are amplitude coefficients of the eigenmodes in the forward and backward directions, respectively.

4.5 Scattering Matrices

At this point, the field propagation through a uniform layer in the z-direction is solved. In reality, most of the devices are composed of several layers or can be approximated with several layers. The next stage is to match the fields at each boundary, and then solve the multilayer problem. Two approaches, namely transfer matrix (T-matrix) method and scattering matrix (S-matrix) method [75], have been widely used. The T-matrix method, could be numerically unstable due to the exponential growing wave amplitudes within layers as pointed by Moharam [63]. The stability of S-matrix method is indeed better than that of the T-matrix method [64]. However, the stability comes with a price as there are more matrix manipulations involving in S-matrix approach. As such, the S-matrix method could be slower than the T-matrix method. In this work, we chose S-matrix method considering the numerical stability.

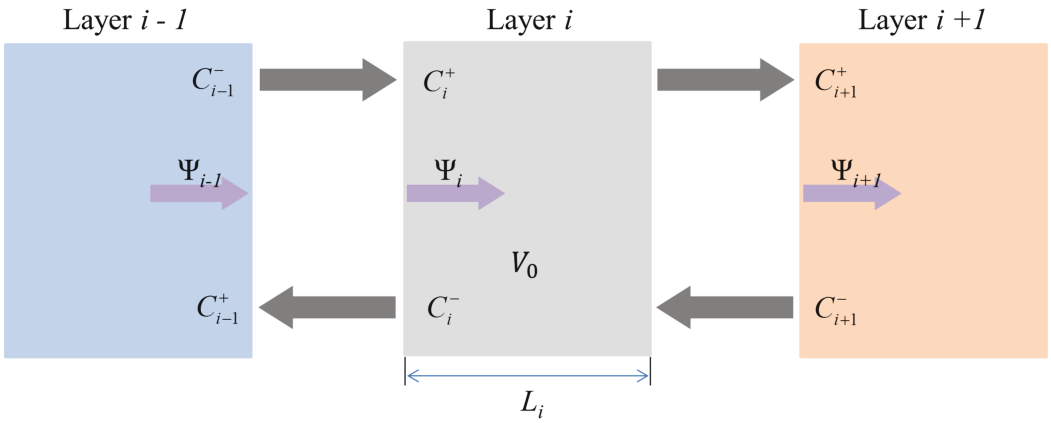

Figure 4.2: Mathematical framework for the scattering matrix of the i^{th} layer. The tangential components of the field are continuous across the first and second interfaces.

4.5.1 Single layer

Figure 4.2 illustrates the mathematical framework of the scattering matrix for the i^{th} layer. Since the tangential components of the field are continuous across the interface, we enforce the boundary conditions at the first and second interfaces, respectively, as in Eqs. 4.45 and 4.46.

At the first interface:

$$\begin{gathered}\mathbf{\Psi_{i-1}} = \mathbf{\Psi_i} \Rightarrow \\ \begin{bmatrix} \mathbf{W}_1 & \mathbf{W}_1 \\ -\mathbf{V}_1 & \mathbf{V}_1 \end{bmatrix} \begin{bmatrix} \mathbf{C}_1^+ \\ \mathbf{C}_1^- \end{bmatrix} = \begin{bmatrix} \mathbf{W}_i & \mathbf{W}_i \\ -\mathbf{V}_i & \mathbf{V}_i \end{bmatrix} \begin{bmatrix} \mathbf{C}_i^+ \\ \mathbf{C}_i^- \end{bmatrix} \Rightarrow \\ \begin{bmatrix} \mathbf{C}_i^+ \\ \mathbf{C}_i^- \end{bmatrix} = \begin{bmatrix} \mathbf{W}_i & \mathbf{W}_i \\ -\mathbf{V}_i & \mathbf{V}_i \end{bmatrix}^{-1} \begin{bmatrix} \mathbf{W}_1 & \mathbf{W}_1 \\ -\mathbf{V}_1 & \mathbf{V}_1 \end{bmatrix} \begin{bmatrix} \mathbf{C}_1^+ \\ \mathbf{C}_1^- \end{bmatrix}\end{gathered} \tag{4.45}$$

At the second interface:

$$\begin{gathered}\mathbf{\Psi_i} = \mathbf{\Psi_{i+1}} \Rightarrow \\ \begin{bmatrix} \mathbf{W}_i & \mathbf{W}_i \\ -\mathbf{V}_i & \mathbf{V}_i \end{bmatrix} \begin{bmatrix} e^{-\lambda_i k_0 L_i} & \mathbf{0} \\ \mathbf{0} & e^{\lambda_i k_0 L_i} \end{bmatrix} \begin{bmatrix} \mathbf{C}_i^+ \\ \mathbf{C}_i^- \end{bmatrix} = \begin{bmatrix} \mathbf{W}_2 & \mathbf{W}_2 \\ -\mathbf{V}_2 & \mathbf{V}_2 \end{bmatrix} \begin{bmatrix} \mathbf{C}_2^+ \\ \mathbf{C}_2^- \end{bmatrix} \Rightarrow \\ \begin{bmatrix} \mathbf{C}_i^+ \\ \mathbf{C}_i^- \end{bmatrix} = \begin{bmatrix} e^{\lambda_i k_0 L_i} & \mathbf{0} \\ \mathbf{0} & e^{-\lambda_i k_0 L_i} \end{bmatrix} \begin{bmatrix} \mathbf{W}_i & \mathbf{W}_i \\ -\mathbf{V}_i & \mathbf{V}_i \end{bmatrix}^{-1} \begin{bmatrix} \mathbf{W}_2 & \mathbf{W}_2 \\ -\mathbf{V}_2 & \mathbf{V}_2 \end{bmatrix} \begin{bmatrix} \mathbf{C}_2^+ \\ \mathbf{C}_2^- \end{bmatrix}\end{gathered} \tag{4.46}$$

By combining Eqs. 4.45 and 4.46 and rearranging the terms, we get the expression in S-matrix form.

$$\begin{bmatrix} \mathbf{C}_1^- \\ \mathbf{C}_2^+ \end{bmatrix} = \begin{bmatrix} \mathbf{S}_{11}^i & \mathbf{S}_{12}^i \\ \mathbf{S}_{21}^i & \mathbf{S}_{22}^i \end{bmatrix} \begin{bmatrix} \mathbf{C}_1^+ \\ \mathbf{C}_2^- \end{bmatrix} \tag{4.47}$$

where

$$\mathbf{S}_{11}^i = (\mathbf{A}_{i1} - \mathbf{X}_i\mathbf{B}_{i2}\mathbf{A}_{i2}^{-1}\mathbf{X}_i\mathbf{B}_{i1})^{-1}(\mathbf{X}_i\mathbf{B}_{i2}\mathbf{A}_{i2}^{-1}\mathbf{X}_i\mathbf{A}_{i1} - \mathbf{B}_{i1}) \tag{4.48}$$

$$\mathbf{S}_{12}^i = (\mathbf{A}_{i1} - \mathbf{X}_i\mathbf{B}_{i2}\mathbf{A}_{i2}^{-1}\mathbf{X}_i\mathbf{B}_{i1})^{-1}\mathbf{X}_i(\mathbf{A}_{i2} - \mathbf{B}_{i2}\mathbf{A}_{i2}^{-1}\mathbf{B}_{i2}) \tag{4.49}$$

$$\mathbf{S}_{21}^i = (\mathbf{A}_{i2} - \mathbf{X}_i\mathbf{B}_{i1}\mathbf{A}_{i1}^{-1}\mathbf{X}_i\mathbf{B}_{i2})^{-1}\mathbf{X}_i(\mathbf{A}_{i1} - \mathbf{B}_{i1}\mathbf{A}_{i1}^{-1}\mathbf{B}_{i1}) \tag{4.50}$$

$$\mathbf{S}_{22}^i = (\mathbf{A}_{i2} - \mathbf{X}_i\mathbf{B}_{i1}\mathbf{A}_{i1}^{-1}\mathbf{X}_i\mathbf{B}_{i2})^{-1}(\mathbf{X}_i\mathbf{B}_{i1}\mathbf{A}_{i1}^{-1}\mathbf{X}_i\mathbf{A}_{i2} - \mathbf{B}_{i2}) \tag{4.51}$$

$$\begin{aligned}\mathbf{A}_{i1} &= \mathbf{W}_i^{-1}\mathbf{W}_1 + \mathbf{V}_i^{-1}\mathbf{V}_1 \\ \mathbf{B}_{i1} &= \mathbf{W}_i^{-1}\mathbf{W}_1 - \mathbf{V}_i^{-1}\mathbf{V}_1 \\ \mathbf{A}_{i2} &= \mathbf{W}_i^{-1}\mathbf{W}_2 + \mathbf{V}_i^{-1}\mathbf{V}_2 \\ \mathbf{B}_{i2} &= \mathbf{W}_i^{-1}\mathbf{W}_2 - \mathbf{V}_i^{-1}\mathbf{V}_2\end{aligned} \tag{4.52}$$

$$\mathbf{X}_i = e^{-\lambda_i k_0 L_i} \tag{4.53}$$

Note that the scattering matrix is not only affected by the material inside itself but also by material outside itself. This fact prevents the S-matrix from having the ability to be interchangeable. In our method, to make each layer interchangeable without recalculating the same layer with different neighboring layers, each layer is separated by free space gap. The device is the stack of different layers with two free space gaps on both sides. As long as the gap has zero thickness, the numerical result will not be changed, and thus, our S-matrix will have interchangeability [67]. For this reason, the S-matrix can be rewritten as:

$$\begin{aligned} \mathbf{S}_{11}^{i} &= \mathbf{S}_{22}^{i} = (\mathbf{A}_i - \mathbf{X}_i\mathbf{B}_i\mathbf{A}_i^{-1}\mathbf{X}_i\mathbf{B}_i)^{-1}(\mathbf{X}_i\mathbf{B}_i\mathbf{A}_i^{-1}\mathbf{X}_i\mathbf{A}_i - \mathbf{B}_i) \\ \mathbf{S}_{12}^{i} &= \mathbf{S}_{21}^{i} = (\mathbf{A}_i - \mathbf{X}_i\mathbf{B}_i\mathbf{A}_i^{-1}\mathbf{X}_i\mathbf{B}_i)^{-1}\mathbf{X}_i(\mathbf{A}_i - \mathbf{B}_i\mathbf{A}_i^{-1}\mathbf{B}_i) \end{aligned} \tag{4.54}$$

$$\begin{aligned} \mathbf{A}_i &= \mathbf{W}_i^{-1}\mathbf{W}_0 + \mathbf{V}_i^{-1}\mathbf{V}_0 \\ \mathbf{B}_i &= \mathbf{W}_i^{-1}\mathbf{W}_0 - \mathbf{V}_i^{-1}\mathbf{V}_0 \end{aligned} \tag{4.55}$$

where $\mathbf{W}_0$ and $\mathbf{V}_0$ are for free space. Another advantage of this arrangement is that the S-matrix becomes symmetric, and half of the scattering parameters do not need to be calculated.

4.5.2 Multilayer structure

For multilayer structures, S-matrices for different layers have to be combined to form a single S-matrix to represent the optical properties of the device. The combination of two S-matrices is realized using the Redheffer star product [76]. It is derived by writing Eq. 4.47 for two-mode coefficients, and then rearranging terms to eliminate the common ports, as a schematic can be found in Fig. 4.3. Mathematically, it is written as:

$$\mathbf{S}^{i+j} = \mathbf{S}^{i} \otimes \mathbf{S}^{j} = \begin{bmatrix} \mathbf{S}_{11}^{i} & \mathbf{S}_{12}^{i} \\ \mathbf{S}_{21}^{i} & \mathbf{S}_{22}^{i} \end{bmatrix} \otimes \begin{bmatrix} \mathbf{S}_{11}^{j} & \mathbf{S}_{12}^{j} \\ \mathbf{S}_{21}^{j} & \mathbf{S}_{22}^{j} \end{bmatrix} = \begin{bmatrix} \mathbf{S}_{11}^{i+j} & \mathbf{S}_{12}^{i+j} \\ \mathbf{S}_{21}^{i+j} & \mathbf{S}_{22}^{i+j} \end{bmatrix} \tag{4.56}$$

where

$$\begin{aligned}
\mathbf{S}_{11}^{i+j} &= \mathbf{S}_{11}^{i} + \mathbf{S}_{12}^{i}[\mathbf{I} - \mathbf{S}_{11}^{j}\mathbf{S}_{22}^{i}]^{-1}\mathbf{S}_{11}^{j}\mathbf{S}_{21}^{i} \\
\mathbf{S}_{12}^{i+j} &= \mathbf{S}_{12}^{i}[\mathbf{I} - \mathbf{S}_{11}^{j}\mathbf{S}_{22}^{i}]^{-1}\mathbf{S}_{12}^{j} \\
\mathbf{S}_{21}^{i+j} &= \mathbf{S}_{21}^{j}[\mathbf{I} - \mathbf{S}_{22}^{i}\mathbf{S}_{11}^{j}]^{-1}\mathbf{S}_{21}^{i} \\
\mathbf{S}_{22}^{i+j} &= \mathbf{S}_{22}^{j} + \mathbf{S}_{21}^{j}[\mathbf{I} - \mathbf{S}_{22}^{i}\mathbf{S}_{11}^{j}]^{-1}\mathbf{S}_{22}^{i}\mathbf{S}_{12}^{j}
\end{aligned} \tag{4.57}$$

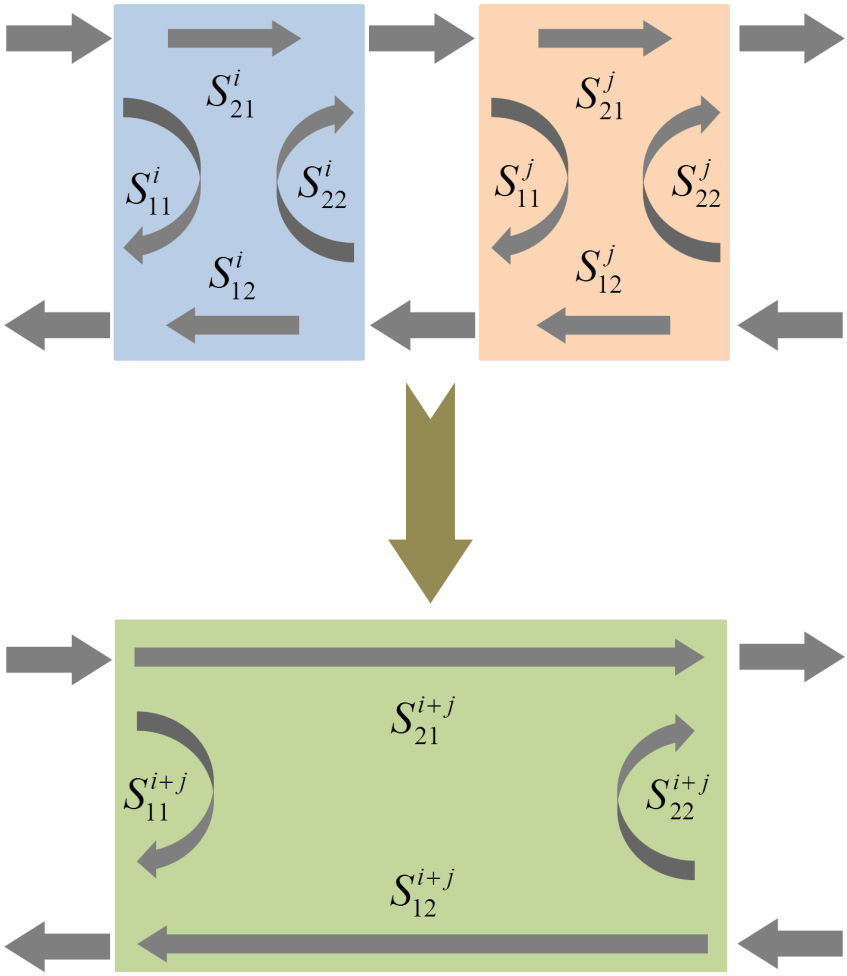

Figure 4.3: Concept of combining scattering matrices with the Redheffer star product.

4.5.3 External regions

By using the procedures we described above, the entire device can be represented as a single S-matrix. By default, the device resides in free space. But it is not the case for real-world problems. To add more flexibility to our method, additional S-matrices

are incorporated to connect the device to other external regions. The reflection and transmission region matrices are calculated in the same way using Eqs. 4.48-4.53. The calculated S-matrices in the reflection region ($\mathbf{S}^{ref}$) and transmission region ($\mathbf{S}^{trn}$) are connected to the overall scattering matrix of the device ($\mathbf{S}^{device}$) to get the global scattering matrix ($\mathbf{S}^{global}$).

$$\mathbf{S}^{global} = \mathbf{S}^{ref} \otimes \mathbf{S}^{device} \otimes \mathbf{S}^{trn} \tag{4.58}$$

4.6 Reflectance and Transmittance

The global S-matrix relates the input incident light with the reflected wave and transmitted wave. The mode coefficients of the reflected and transmitted regions are calculated with Eq. 4.59:

$$\begin{aligned} \mathbf{C}_{ref} &= \mathbf{S}_{11}^{global}\mathbf{C}_{inc} \\ \mathbf{C}_{trn} &= \mathbf{S}_{21}^{global}\mathbf{C}_{inc} \end{aligned} \tag{4.59}$$

The transverse components of the reflected and transmitted fields are derived from:

$$\begin{aligned} \mathbf{r}_T = \begin{bmatrix} \mathbf{r}_x \\ \mathbf{r}_y \end{bmatrix} &= \mathbf{S}_T^{ref} = \mathbf{W}_{ref}\mathbf{C}_{ref} = \mathbf{W}_{ref}\mathbf{S}_{11}\mathbf{C}_{inc} \\ \mathbf{t}_T = \begin{bmatrix} \mathbf{t}_x \\ \mathbf{t}_y \end{bmatrix} &= \mathbf{S}_T^{trn} = \mathbf{W}_{trn}\mathbf{C}_{trn} = \mathbf{W}_{trn}\mathbf{S}_{21}\mathbf{C}_{inc} \end{aligned} \tag{4.60}$$

The longitudinal field components are calculated using the Maxwell's divergence equations.

$$\begin{aligned} \mathbf{r}_z &= -\tilde{\mathbf{K}}_{z,ref}^{-1}(\tilde{\mathbf{K}}_x\mathbf{r}_x + \tilde{\mathbf{K}}_y\mathbf{r}_y) \\ \mathbf{t}_z &= -\tilde{\mathbf{K}}_{z,trn}^{-1}(\tilde{\mathbf{K}}_x\mathbf{t}_x + \tilde{\mathbf{K}}_y\mathbf{t}_y) \end{aligned} \tag{4.61}$$

where

$$\begin{aligned} \tilde{\mathbf{K}}_{z,ref}^{-1} &= -(\sqrt{\mu_{r,ref}\varepsilon_{r,ref}\mathbf{I} - \tilde{\mathbf{K}}_x^2 - \tilde{\mathbf{K}}_y^2}) \\ \tilde{\mathbf{K}}_{z,trn}^{-1} &= -(\sqrt{\mu_{r,trn}\varepsilon_{r,trn}\mathbf{I} - \tilde{\mathbf{K}}_x^2 - \tilde{\mathbf{K}}_y^2}) \end{aligned} \tag{4.62}$$

Then the reflectance and transmittance can be obtained.

$$\begin{aligned} \mathbf{R} &= \mathrm{Re}\left[\frac{-\mathbf{K}_{z,ref}}{\tilde{k}_{z,inc}}\right] \cdot \left|\tilde{\mathbf{r}}\right|^2 \\ \mathbf{T} &= \mathrm{Re}\left[\frac{\mu_{r,inc}\mathbf{K}_{z,trn}}{\mu_{r,trn}\tilde{k}_{z,inc}}\right] \cdot \left|\tilde{\mathbf{t}}\right|^2 \end{aligned} \tag{4.63}$$

where

$$\begin{aligned} \left|\tilde{\mathbf{r}}\right|^2 &= \left|\tilde{\mathbf{r}}_x\right|^2 + \left|\tilde{\mathbf{r}}_y\right|^2 + \left|\tilde{\mathbf{r}}_z\right|^2 \\ \left|\tilde{\mathbf{t}}\right|^2 &= \left|\tilde{\mathbf{t}}_x\right|^2 + \left|\tilde{\mathbf{t}}_y\right|^2 + \left|\tilde{\mathbf{t}}_z\right|^2 \end{aligned} \tag{4.64}$$

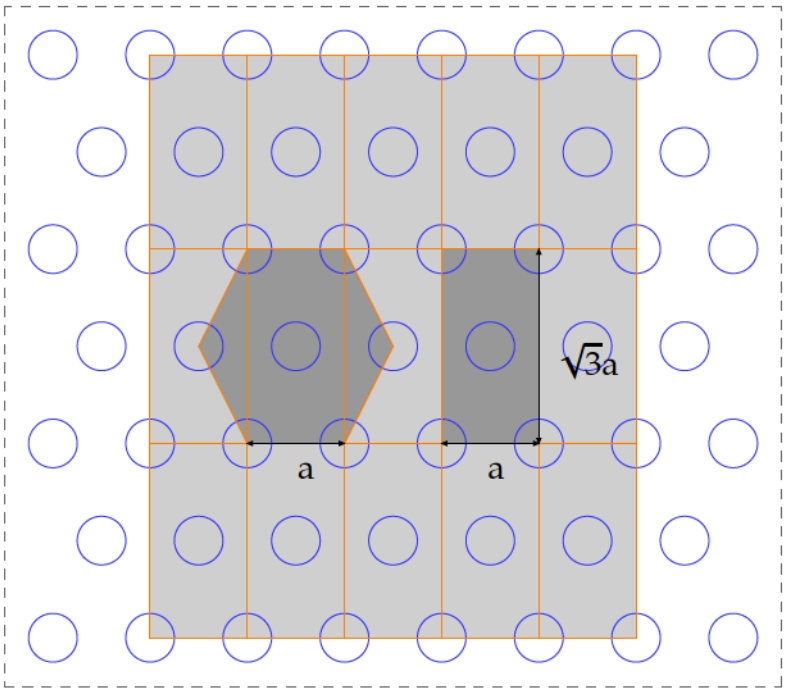

Figure 4.4: The concept of representing a hexagonal lattice with a rectangular lattice in RCWA simulation. The hexagonal lattice can be reconstructed by adding the lattices in the rectangular grey area under periodic boundary condition.

4.7 Hexagonal Lattice Approximation

The above derivations are aimed to calculate structures with rectangular lattice. New formulations have to be made to compute patterns with hexagonal lattice. However, a trick can be played to calculate the hexagonal patterns by sacrificing some computational time. As a two-dimensional hexagonal lattice pattern (infinitely extended) can be represented by a rectangular lattice, as shown in Fig. 4.4. By computing a lattice

in the rectangular dark grey area under periodic boundary condition, a hexagonal pattern is calculated. The drawback is that the computed area with rectangular lattice approximation is larger than directly computing the hexagonal lattice, which leads to longer calculation time. Note that the side length of the approximated rectangular lattice is not equal, so different numbers of Fourier components have to be used in both directions.

4.8 Code Verification and Convergence Study

The accuracy of the Fourier method is directly related to the number of Fourier coefficients used in the simulation. As the number of Fourier components increases, the dielectric structure is represented with higher accuracy. But the scale of the matrices involved in the calculation increases. Since these are full matrices, the calculation time increases dramatically. For the sake of computational time, a small number of Fourier coefficients is always preferred as long as the result is accurate enough.

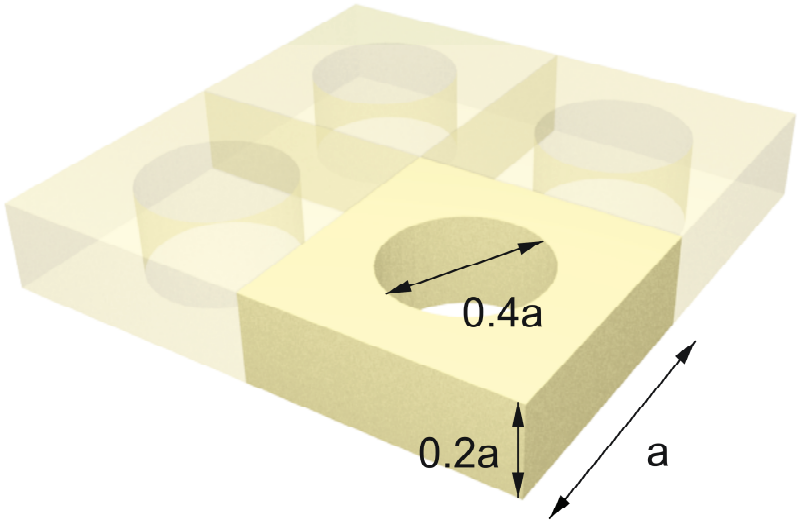

Figure 4.5: Simulated silicon photonic crystal ($\epsilon = 12$) slab consisting of a square lattice of air hole with lattice constant of a, hole radius of $0.2a$, and thickness of $0.5a$.

We benchmark our code using a dielectric structure described in reference [77] and shown in Fig. 4.5. The thickness of the slab is $0.5a$, and the radius of the air holes is $0.2a$, where a is the lattice constant. The dielectric constant of the slab is 12. Parts of

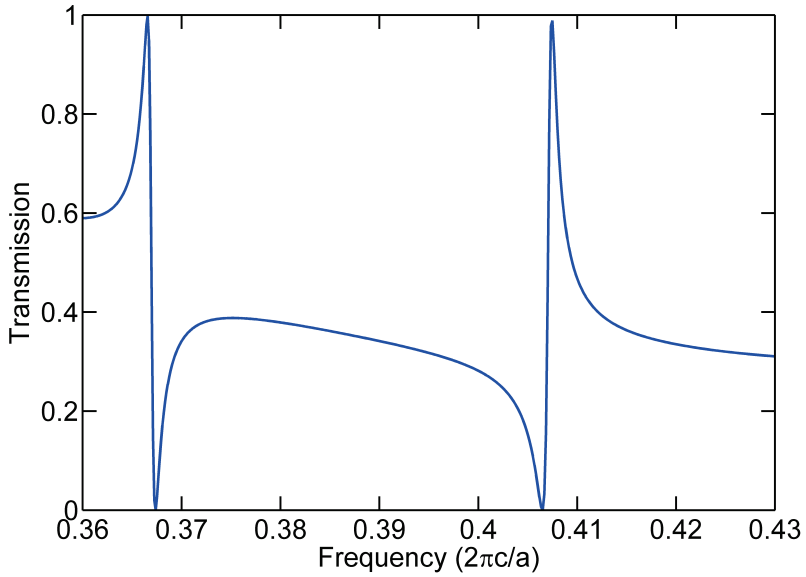

Figure 4.6: Transmission spectrum of the simulated photonic crystal slab exhibiting two transmision peaks.

the transmission spectrum are shown in Fig. 4.6. By comparing the two results, RCWA matches well with the FDTD simulation. The convergence features of the two peaks are observed for increasing Fourier components, which is shown in Fig. 4.7. As we can see, the result reaches convergence with a fair number of Fourier components for both peaks.

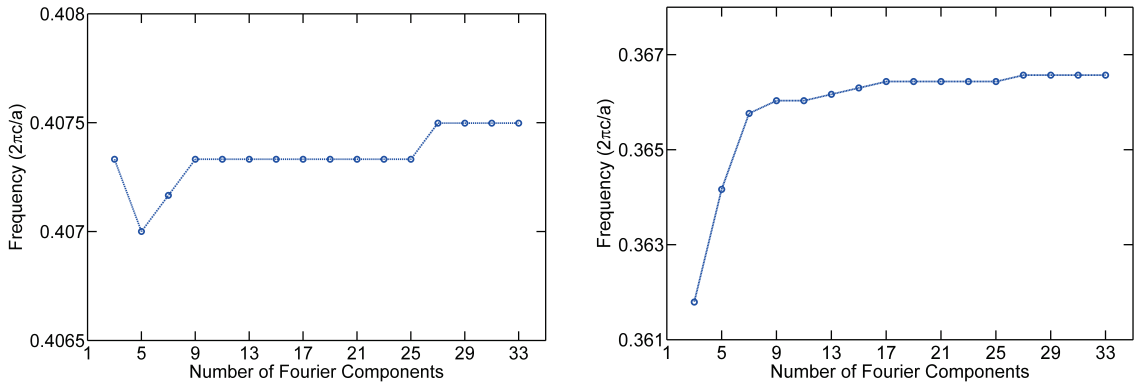

(a) peak 1 (b) peak 2

Figure 4.7: Convergence of the two peaks in Fig. 4.6

4.9 Code Implementation Remarks

At last, we pay some attention to the software engineering principles that underlies the architecture of our numerical calculation method. As we stated before, the method that we implemented right now can only handle some simulation problems (moderate reflective contrast structure). And different new techniques have been continuously developed to improve the performance and extend the functionality of this method. In addition, the code is designed to be directly used or integrated with other methods to simulate and optimize periodic structures. From these aspects, it is of importance to build a user-friendly and easy to maintain and extend modelling tool.

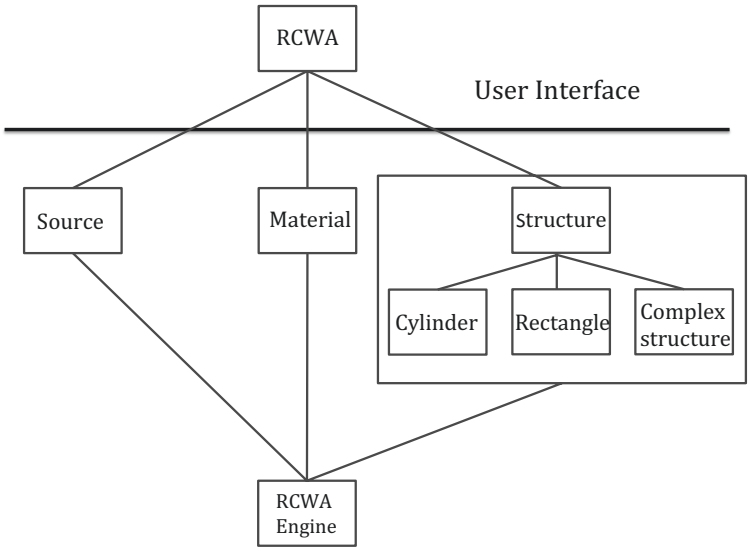

Figure 4.8: Concept diagram for the implemented RCWA code. Considering the maintenance, debugging and calculation speed, we isolate the calculation kernel and construct three objects (Source, Material and Structure) to interact with the calculation kernel. These three objects are also used to enforce the encapsulation and the user-friendly interface.

To achieve such complex requirements, we chose an object-oriented programming (OOP) paradigm instead of a procedural programming paradigm to implement the code. In OOP, data and methods of manipulating the data are kept as a single unit called an object. It can provide "services" to users, other objects or functions via the object's methods. In this way, the data and the corresponding functions that manipulate the

data are encapsulated in an entity. The change of the inner workings of an object is largely independent of other objects, which is called decoupling. By strategically following these principles, the code could be easily reused and extended. However, the software is constructed by a set of objects to realize the functionalities. The definition and separation of objects could be tricky as a poor separation of objects might lead to maintenance and debugging nightmare. Fig 4.8 shows a general view of how the objects separated and connected in our implementation. In this way, the RCWA calculation part is isolated from other parts of the program for easier extension, debugging and interaction.

The OOP approach might lead to slower execution because the abstraction mechanisms induce a certain amount of overhead. But the running time is not the only relevant figure of merit for software. Other features such as easy to debug, extend and maintain are also of importance. As such, we argue that OOP is preferable concerning these issues [78].

4.10 Conclusion

We have gone through the derivations of RCWA method in detail. An example has been included to validate the implemented code. Some final remarks were given about the code implementation. We regard the RCWA method as one of the best approaches to rigorously calculate the optical response of periodic patterns in spite of some imperfections. In the next chapter, we use this powerful tool to explore the optical performance of periodic structures.

Chapter 5

Photon Control with Periodic Structures

There has been significant interest in expanding the concept of periodicity for photon manipulation. The birth of aperiodic or pseudo-disordered structures is the result of this movement. Compared with traditional periodic structures, pseudo-disordered structures have only long-range order. The pseudo-disordered structures seem to be chaos in short range, but they are periodic based on extending unit cell. As an extension of ordered structures, pseudo-disordered structures gain increasing attention for broad-band and broad-angle applications because of these unique advantages such as higher point group symmetry and richer Fourier spectra. Even though pseudo-disordered structures enable additional design freedom for photon management, the optimization and interpretation are challenging when a large number of degrees of freedom encounters computationally intensive electromagnetic simulation methods.

In this section, we propose to apply an advanced mathematical scheme to investigate photon control in pseudo-disordered structures, with the help of the electromagnetic calculation method that we developed in the previous chapter. The proposed one-dimensional multi-periodic pattern generation method can help us squeeze the disorder design space before performing the rigorous calculations, by making use of the periodic attribute of the patterns. Consequently, thanks to the pre-filtered design space, it typically relieves us from the computational burden and enables us to 'globally' optimize

and study pseudo-disordered patterns. As an example, we show how this approach can be used to comprehensively optimize and systematically analyze generated disorder for broadband light trapping in a thin film.

5.1 Motivation

Photonic Crystal (PC) structures are well known to be able to control light propagation and possibly light-matter interaction for applications such as guided optics [79], microcavities [80], Light-Emitting Devices [81], Surface-Enhanced Raman Scattering [82]. As PC structures are highly efficient for selected wavelengths or angles, it has been proposed to resort to random [83–85], quasi-crystal [86–90], or multi-periodic [91–98] structures to control light properties over a broadband spectrum or angle. Heuristic optimization methods, such as Genetic Algorithm (GA) [99–101] and Particle Swarm Optimization (PSO) algorithm [102] that can be used to design and optimize periodic structure become of less interest for pseudo-disordered structures since the degree of freedom or number of parameters greatly increase. In order to analyze such structures one can resort to statistical study as it can be done on nanopatterned [103] or rough absorber [83].

In this section, we propose to apply to multi-periodic patterns a mathematical scheme based on a combinatorial problem named free necklace problem [104] to partially conquer the conflict between the design freedom and vast search space. The basic idea is to eliminate patterns which seem to be unique in short range, yet they are replications of other patterns in long range with periodic boundary conditions. A schematic illustration of this concept is shown in Fig. 5.1. The detailed explanation is presented in section 5.2. Then these intentionally created unrepeated disordered patterns can be used to systematically and comprehensively study the effect of short range disorder for photon management. We illustrate its usefulness with broadband light trapping in crystalline Silicon (c-Si) substrate decorated with stripe arrays, which is shown in section 5.3. Through numerical simulation, we demonstrate in section 5.4 that, by adding 'appropriate' engineered fine stripes to each long period, these so-called

multi-periodic patterns achieved high broad-band light trapping efficiency.

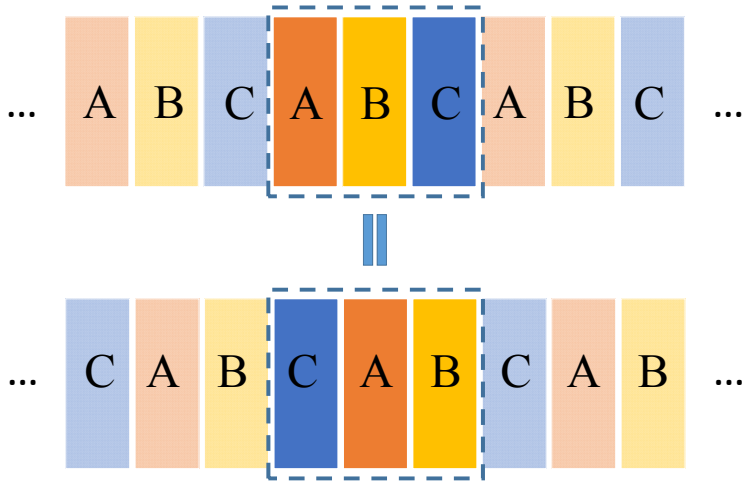

Figure 5.1: A schematic illustration of the equality of patterns with long range order and short range disorder. The unite cell that is composed of 'ABC' is equal to the unit cell 'CAB' on condition that each unit cell is infinitely repeated.

5.2 Free Necklace (or Bracelet) Problem

The pattern generation method is based on a combinatorial problem named necklace problem. It is a general method to construct unique patterns that are infinitely repeated. Specifically, we focus on the free necklace problem or bracelet problem, which means opposite orientations (mirror images) are regarded as equivalent.

Let us first consider a string of n characters where each character can take a value among k possibilities, the total number of all possible strings is:

$$S_k(n) = n^k \tag{5.1}$$

From combinatorics, if we replace the string by a necklace, thanks to rotational symmetry,

the number of possible necklaces reduces to:

$$N_k(n) = \frac{1}{n}\sum_{i=1}^{v(n)} \varphi(d_i) k^{n/d_i} \tag{5.2}$$

where d_i are the divisors of n, $v(n)$ is the number of divisors of n, and $\varphi(d_i)$ is Euler's totient function. In the case of free necklace (or bracelet), the mirror symmetry decreases this value to:

$$B_k(n) = \begin{cases} \frac{1}{2}N_k(n) + \frac{1}{4}(k+1)k^{n/2} & n \text{ even} \\ \frac{1}{2}N_k(n) + \frac{1}{2}k^{(n+1)/2} & n \text{ odd} \end{cases} \tag{5.3}$$

Let us focus on arrangements with a length of 4 digits that can take 2 different values ('0' and '1'). Table 5.1 shows all the possible strings as well as the possible bracelets. For instance, the binary quadruple {1100} is the representative of set {1100, 0110, 0011, 1001} and {1010} is the representative of set {1010, 0101}. In this case it appears that only 6 bracelets are needed, instead of 16 strings, to represent all the possibilities so 2.7 times less.

Table 5.1: Construction of strings and bracelets for a binary quadruple.

Strings	0 0 0 0	1 0 0 0 0 1 0 0 0 0 1 0 0 0 0 1	1 1 0 0 0 1 1 0 0 0 1 1 1 0 0 1	1 0 1 0 0 1 0 1	1 1 1 0 1 0 1 1 1 1 0 1 1 1 1 0	1 1 1 1
Bracelets	0 0 0 0	1 0 0 0	1 1 0 0	1 0 1 0	1 1 1 0	1 1 1 1

This method could be even powerful when it is applied to complex patterns. Table 5.2 shows arrangements with a length of 10 digits that can take different values from 2 to 5. As we can see that the reducing factor increases from 13 to around 20. It implies that at least 90% of all the strings are repetitions of the bracelets for these different cases.

The algorithm explained in reference [104] was used to efficiently generate all the possible bracelets with different lengths of code sequences (up to 20). The detailed code implementation can be found in Appendix C. Table 5.3 illustrates the comparison of

Table 5.2: Comparison of the number of strings ($S_k(10)$) and bracelets ($B_k(10)$) for different number of possible values (k).

k	$S_k(10)=k^{10}$	$B_k(10)$	$S_k(10)/B_k(10)$
2	1024	78	13.1
3	59049	3210	18.1
4	1048576	53764	19.5
5	9765625	493131	19.8

the number of strings and bracelets for different lengths of binary code sequences [105]. As we can see, the reduction factor drastically increases with the increase of the length of the binary code sequences (more than 30 for the length longer than 17 characters).

Table 5.3: Comparison of the number of strings ($S_2(N)$) and bracelets ($B_2(N)$) for different lengths of binary code sequences (N).

N	$S_2(N)=2^N$	$B_2(N)$	$S_2(N)/B_2(N)$
2	4	3	1.3
4	16	6	2.7
6	64	13	4.9
8	256	30	8.5
10	1024	78	13.1
12	4096	224	18.3
14	16384	687	23.8
15	32768	1224	26.8
16	65536	2250	29.1
17	131072	4112	31.9
18	262144	7685	34.1
20	1048576	27012	38.8

In the following we will combine the bracelet generation algorithm with binary PC. As we can simulate all the possible arrangements without losing any time due to 'multiple simulations', we argue that in contrast with heuristic algorithms (e.g. PSO and GA), our optimization process always leads to the overall optimum among all the PCs with a given width for all the binary slices. Beyond that, our approach remains very flexible, as various unrepeated patterns can be easily constructed by using the general formation (Eq. 5.3).

5.3 Multi-periodic Structures

Let us define the device that we will study. A 1 μm thick c-Si layer was chosen to study light trapping under un-polarized normal incident light. All the patterns were generated based on this single layer. No antireflective coating and back reflector were used for the sake of simplicity and clarity. In order to give a general demonstration of our approach, the simple integrated absorption (I_{abs}) in a wide wavelength range (from 300 to 1100 nm) was calculated as figure of merit. Our calculations were done using rigorous coupled wave analysis (RCWA) [20] with improvement for TM polarization [70]. Sufficient spatial harmonics were used to guarantee the accuracy and a reasonable calculation time (few minutes for a typical desktop computer).

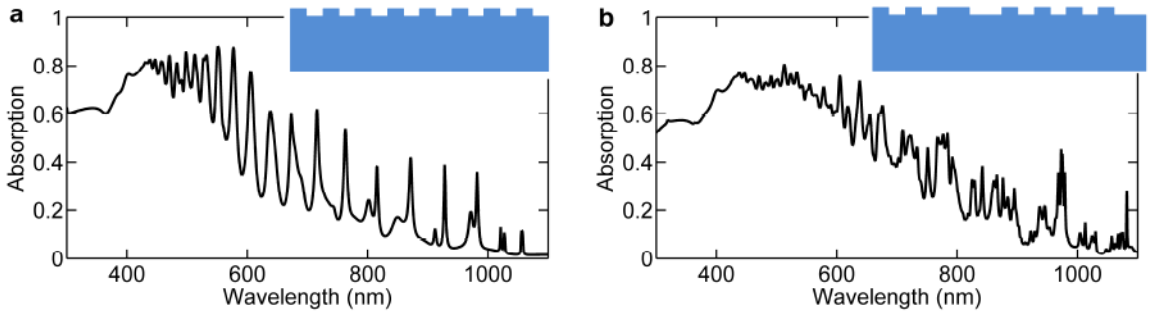

Figure 5.2: Absorption spectra of a 1 μm thick c-Si layer under un-polarized normal incident light, (a) for the optimized mono-periodic PC with lattice length of 300 nm (inset shows a typical cell) and (b) for the optimized multi-periodic PC with lattice length of 2550 nm (inset shows a typical cell).

First we employed PSO algorithm [106] to optimize the absorption of the c-Si layer by varying 3 parameters (period, groove depth and filling fraction). After the whole optimization process, the best-performed pattern (so-called mono-periodic pattern) with etching depth of 106 nm, period of 311 nm, and filling factor of 0.502 yielded an integrated absorption of 37.8%. For the sake of clarity we fixed the etching depth to 100 nm, period to 300 nm and filling factor to 0.5. It yielded an optimum integrated absorption of 37.7% (Fig. 5.2a), which is 75.3% higher than that of the bare silicon slab (I_{abs}=21.5%). Detailed explanation of the PSO optimization method that we used can be found in Appendix D.

Then the multi-periodic patterns considered in this paper were generated by setting

an identical length of ridge and groove according to the generated code sequences ('1' represents a ridge and '0' represents a groove). The etching depth was the same as the mono-periodic pattern and the length of ridges and grooves was set to be 150 nm. As the size of '1' and '0' was set, patterns represented by long code sequences ended up with long lattice length.

Table 5.4: The optimized code sequences with different lengths of binary code sequences (N). The all-zero code sequences were excluded. Patterns with lattice length of 2700 nm and 3000 nm were optimized with constraint to 50% filling fraction because of the heavy computational burden.

N	Lattice length	Code sequence	I_{abs}
2	300 nm	10	37.7%
4	600 nm	1010	37.7%
6	900 nm	101100	38.8%
8	1200 nm	10101100	39.2%
10	1500 nm	1010101100	39.7%
12	1800 nm	101001100100	40.7%
14	2100 nm	10101101100100	41.1%
15	2250 nm	110010010100100	41.7%
16	2400 nm	1010110100110100	42.1%
17	2550 nm	10101100101010100	42.2%
18	2700 nm	101010101011001100	41.8%
20	3000 nm	10101011010110010100	42.1%

5.4 Results and Discussion

In this section we study the PC obtained using the bracelet generation algorithm to optimize and analyze light trapping in the c-Si layer. All the multi-periodic patterns listed in Table 5.3 have been simulated. The code sequences of different lengths that maximize I_{abs} are listed in Table 5.4. Large I_{abs} (>40%) is achieved for patterns containing at least 12 characters. When the period of multi-periodic pattern equals 2550 nm (containing 17 characters), I_{abs} is as large as 42.2% (Fig. 5.2b), which is 11.9% higher than that of the optimized mono-periodic pattern (Fig. 5.2a).

5.4.1 Analysis in real space

To simplify the analysis and discussion, we define the number of '1's in the code sequence as number of ridges, which is directly linked to filling fraction *ff* (*ff* = number of ridges/N). It is noticeable that for all the optimal code sequences listed in Table 5.4, *ff* is close or equal to 50%. More precisely, *ff* = 50% for even values of N except for N =12 where *ff* = 5/12, and *ff* = 6/15 for N=15 and 8/17 for N=17.

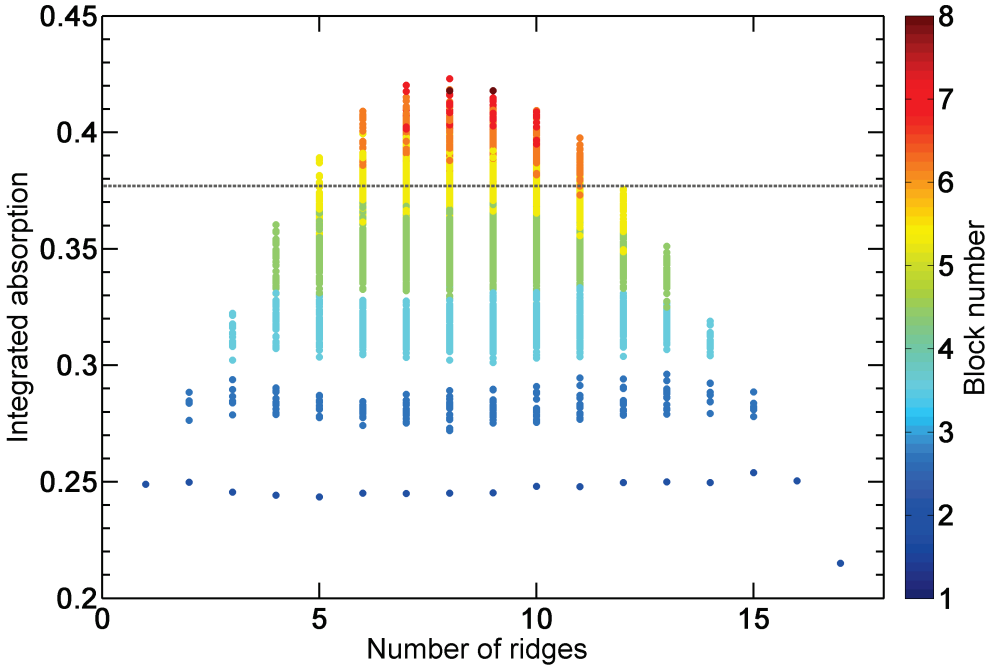

Figure 5.3: Integrated absorption achieved for all the unrepeated representations of a multi-period pattern with lattice length of 2550 nm. Block numbers are represented by different colors. The horizontal dashed line shows the I_{abs} of the optimized mono-periodic pattern under un-polarized illumination.

Then, the pattern generation method is used to comprehensively study multi-periodic pattern since each generated pattern is unique. To understand the absorption improvement, we analyze the patterns with lattice length of 2550 nm. Figure 5.3 shows the I_{abs} map of all unrepeated multi-periodic patterns. Each point in the map represents a unique design of the pattern as a function of the number of ridges. Moreover, block number (BN) is defined as the number of ridge groups in a multi-periodic pattern, which is represented by different colors in the image. Obviously, it can be noted that the performance of the optimized pattern increases and then decreases with the number

of ridges. As previously mentioned, the best-performed pattern appears in the group with approximately *ff*=50%, and patterns with similar *ff* also perform quite well (Fig. 5.3). Another overall property is the outperformed patterns appear in the patterns with relatively large BN. Associated to the moderate *ff*, it avoids the clustering of ridges, and thus enriches the diversity of the generated patterns. Similar conclusions derived from a statistical study [107].

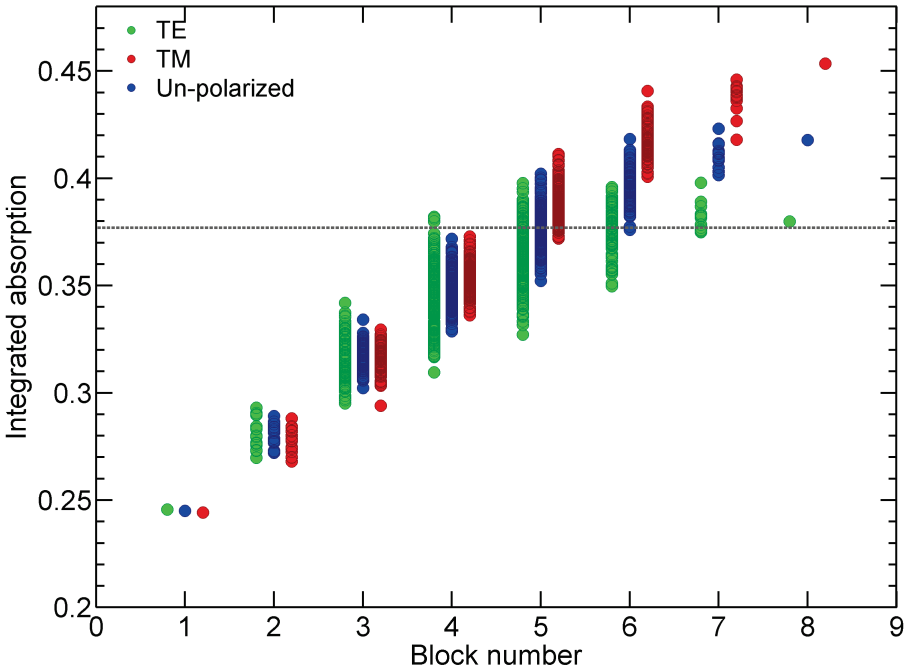

Figure 5.4: Integrated absorption for all different multi-periodic patterns with lattice length of 2550 nm and number of ridges of 8. The horizontal dashed line shows the I_{abs} of the optimized mono-periodic pattern under un-polarized illumination.

To analyze further in details, we choose patterns with the number of ridges of 8 which exhibit the highest I_{abs} for detailed discussion. Figure 5.4 shows the relation between I_{abs} and BN under TE (electric field parallel to the groove lines), TM (electric field perpendicular to the groove lines), and un-polarized illuminations. From the viewpoint of morphology, this map exhibits two features that can be correlated with large absorption enhancement.

Firstly, TE and TM modes respond differently to patterns with the same BN. As

we can see in Fig. 5.4, these points that represent I_{abs} for the TM mode with the same BN are more compact than those for the TE mode, reflecting that the first one is less sensitive to patterns with the same BN than the second one. In addition, the optical performances for TM and TE polarizations are not matched for a given pattern. As such, it is necessary to take into account the influence of the polarization. Secondly, TE and TM modes share the same tendency despite a non-perfect matching. I_{abs} grows with increasing BN then slows down or drops for large BN. The best-performed multi-periodic pattern appears in patterns with relatively large BN. We believe that this kind of spatial arrangement of stripes can efficiently couple both TE and TM modes into the pseudo-guided modes supported by the silicon slab when the reciprocal lattice vector of the grating matches the propagation constant of these modes [107].

5.4.2 Analysis in Fourier space

In reciprocal space, the relationship between the stripe arrangement and its optical performance is more profound and clear. Patterns with appropriate large BN tend to provide affluent Fourier components, and the absorption is linked with the richness of Fourier components [95, 108, 109]. Hence, Fourier transform was performed for all the patterns (represented by code sequences) illustrated in Fig. 5.4. The Fourier coefficient maps are shown in Fig. 5.5a and 5.5c. We notice a significant correlation between the position of the spatial Fourier coefficients and the absorption. Generally, patterns with their Fourier components shifted to higher orders tend to outperform other patterns in both TE and TM modes. In order to quantitatively clarify our argument, a light trapping range in Fourier space is defined. The lower boundary of the spatial frequency that is required for light trapping is defined by light line. Here, 600 nm is chosen to be the critical wavelength because at this wavelength the absorption in c-Si becomes critically weak [109]. It corresponds to a spatial frequency of 10.5 μm^{-1}. The upper limit of the spatial frequency is set to be 31.4 μm^{-1}, as for larger frequencies, the Fourier coefficients become negligible in the interested region [103]. Figure 5.5b and 5.5d show the integrated Fourier components below the lower boundary (from 0 to 10.5 μm^{-1}) and in the light trapping range (from 10.5 to 31.4 μm^{-1}) for all the generated patterns. The

outperformed patterns tend to shift the spatial frequencies into the light trapping range for both modes. As the lower spatial frequency limit is set to the critical wavelength of 600 nm, the coupling into the quasi-guided modes at longer wavelengths contributes more to the light trapping enhancement.

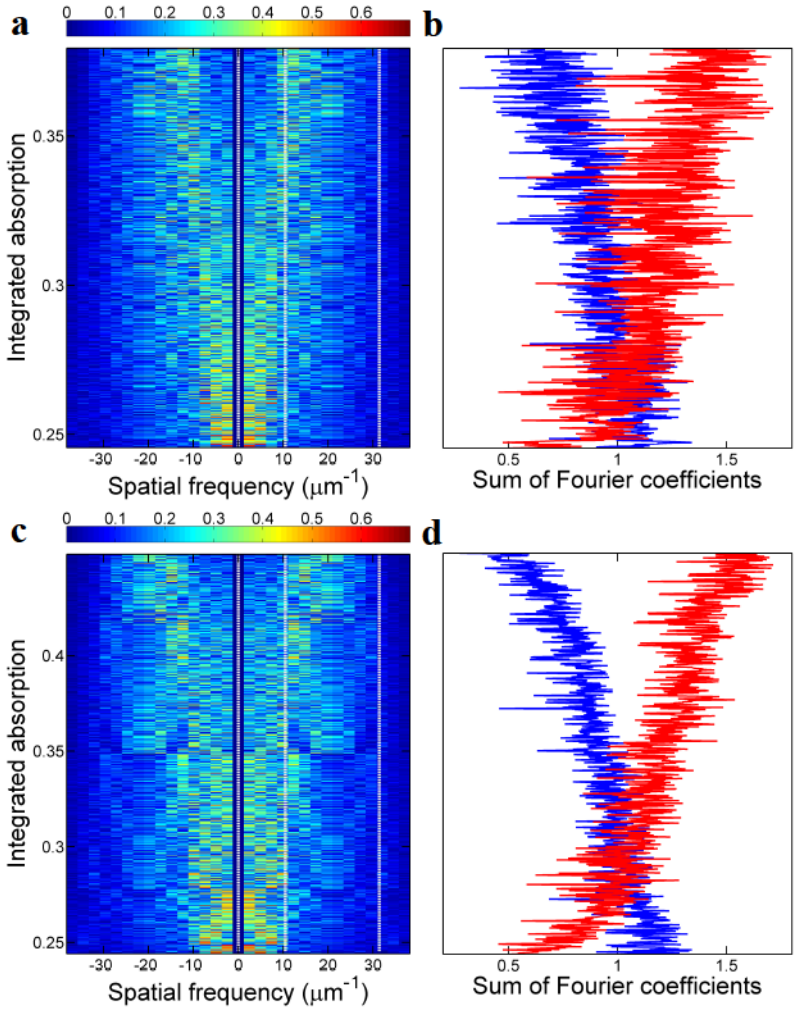

Figure 5.5: Fourier analysis of all the patterns with lattice length of 2550 nm and number of ridges of 8. Fourier transform of the PCs code sequence sorted by increasing absorption for (a) TE mode, and (c) TM mode. The magnitude of Fourier components lying in the leakage range (from 0 to 10.5 μm^{-1} in blue) and in the light trapping range (from 10.5 to 31.4 μm^{-1} in red). To compare the Fourier coefficients of different patterns, the Fourier amplitudes are normalized with respect to the constant zeroth order coefficient. High orders are not taken into account.

Previous optimization study reveals how the multi-periodic pattern can beat others. Then we focus on the absorption mechanism. Compared with mono-periodic PC, multi-

periodic PC excites a larger number of resonances, since more peaks appear in the absorption spectrum of the multi-periodic pattern (Fig. 5.2), which is the reasoning behind multi-periodic design concept. Another point is that the optimum multi-periodic pattern is non-symmetric since the non-symmetric patterns exhibit two times more modes than the symmetric ones [94]. Figure 5.6a and 5.6b show the correlation between the Fourier components of the PC code sequences and their corresponding Fourier components of the fields from 600 to 1100 nm. The optimized mono- and multi- periodic patterns diffract incident light into different orders, and each order has its corresponding Fourier components of the code sequences. In addition, the amplitudes of the Fourier components of the fields (integrated from 600 to 1100 nm) are closely related to the amplitudes of the Fourier components of code sequences [103, 109]. It becomes clear that the optimized multi-periodic pattern diffracts and couples broadband light incident into more supported modes of the beneath silicon slab.

To gain insight into how the spatial arrangement affects absorption in further detail, it is instructive to observe how the electromagnetic field distributes in the patterns for different wavelengths. Figure 5.6d and 5.6e show the field distribution in Fourier space. For the optimized mono-periodic pattern (Fig. 5.6d) the energy mainly remains in low order modes (0 and ± 1 orders) to enhance the absorption from 600 to 1100 nm. Compared with the optimized mono-periodic pattern, the optimized multi-periodic pattern (Fig. 5.6e) can couple light incident into a large amount of modes. The benefit of distributing energy into high order modes becomes obvious especially at large wavelengths. Long lattice length provides multi-periodic patterns access to a large amount of orders in reciprocal space, the structure on the surface leads the distribution of energy into different orders. Patterns that can not only couple light incident into numerous modes but also distribute the energy into various high orders outperform others. In order to illustrate that, we calculated field distribution for a large mono-periodic pattern with the same lattice length and *ff* as the optimized multi-periodic pattern (code sequence: 11111111000000000), as shown in Fig. 5.6c and 5.6f. Even though this pattern can couple incident into multiple orders, the energy is obviously mainly distributed in low orders. As such, the overall performance is not as good as the

optimized multi-periodic pattern.

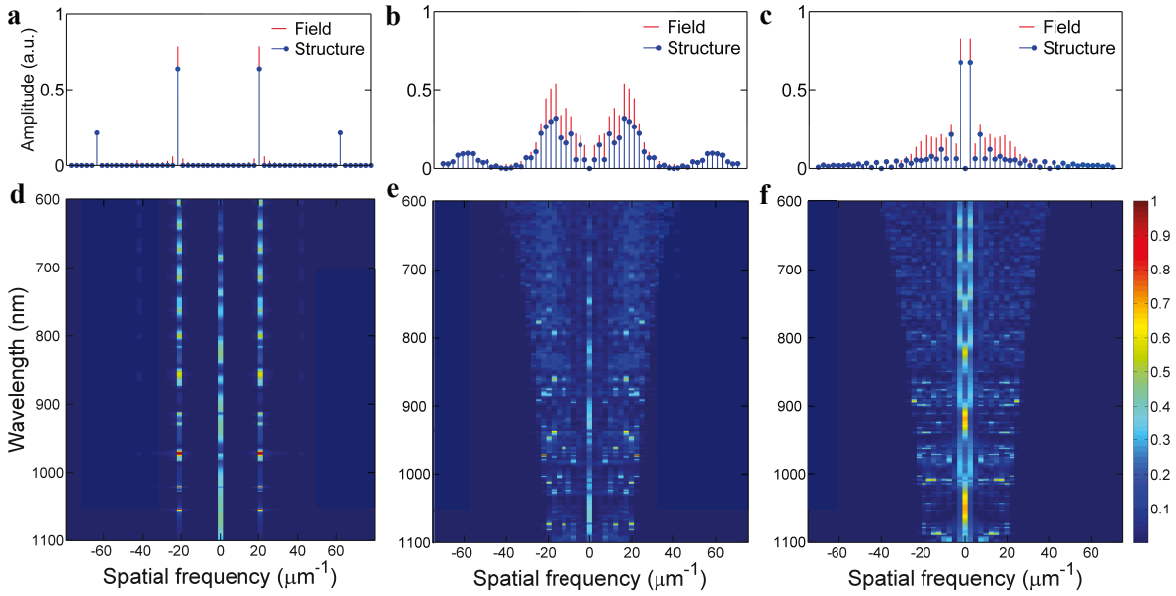

Figure 5.6: Analysis of the optical mode decomposition in Fourier space. Fourier transforms of the PC code sequences and electromagnetic fields (TE-TM averaged) for (a) the optimized mono-periodic pattern, (b) the optimized multi-periodic pattern, and (c) the mono-periodic pattern with the same lattice length and *ff* as the best-performed multi-periodic pattern (code sequence: 1111111000000000). The Fourier transforms of the electromagnetic field is calculated by integrating the Fourier components of the electromagnetic field from 600 to 1100 nm. For easier comparison, the Fourier amplitudes of the PCs code sequences and the fields are normalized according to the strength of zeroth order. As such, the zeroth order is not taken into account. Decomposition of the electromagnetic fields in Fourier space associated to the three selected structures (d, e and f) from 600 to 1100 nm.

5.4.3 Angular analysis

In light trapping, the angular performance is also a crucial criterion. Multi-periodic PCs are tolerant to different input angles because of the multi-mode absorption mechanism [110]. At a given illumination angle, the incident light can be decomposed into different orders with different prorogation angles. For each order, the propagation in the silicon slab might be constructive or destructive depending on the diffraction angle because of the Fabry-Perot phenomenon. The light trapping performance of a pattern at a given incident angle is the overall effect of all the diffraction orders. As the absorption of the optimized multi-periodic pattern at this angle depends on many diffraction orders,

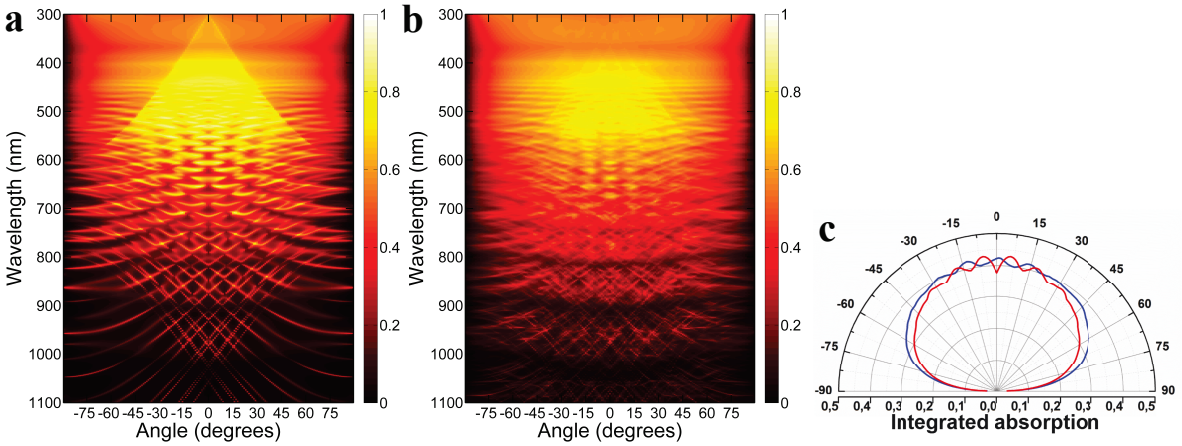

Figure 5.7: TE-TM averaged angular absorption spectra for (a) the optimized mono-periodic pattern, and (b) the optimized multi-periodic pattern. (c) Comparison of integrated absorption between the optimized mono-periodic pattern (red line) and the optimized multi-periodic pattern (blue line) for different angles of un-polarized incident light.

and it is less likely that all the diffraction orders propagate in either constructive or destructive way. Statistically speaking, distributing energy into more orders that might increase or decrease absorption stabilizes the overall absorption efficiency. Because of this, the optimized multi-periodic pattern is less sensitive to angular change. Figure 5.7a and 5.7b show the TE-TM averaged angular absorption spectra for the optimized multi- and mono-periodic patterns. Additional resonances introduced by the optimized multi-periodic pattern present at all angles, contributing to the increased absorption and angular tolerance. Note that the optimized multi-periodic pattern performs differently for positive and negative angles because of the asymmetric structural attribute. Figure 5.7c clearly shows the overall angular performance of the optimized multi- and mono-periodic patterns under the un-polarized state. The I_{abs} oscillates and then drops for the optimized mono-periodic pattern when the incident angle increases. However, the I_{abs} of the optimized multi-periodic pattern remains relatively isotropic and asymmetric for the same amount of incident angle variation. For the incident angles ranging from -75° to 75°, the average I_{abs} for the optimized multi-periodic pattern is found to be 36.9%, whereas for the optimized mono-periodic pattern it is found to be only 35.0%, which quantitatively implies the benefit of the multi-periodic pattern.

From the above discussion, it is clear that patterns with rich Fourier spectra have

more access to different modes and the distribution of energy to each mode is also of importance to enhance absorption. This phenomenon becomes even important for broadband spectrum at different illumination angles. Hence, the multi-periodic pattern benefiting from its flexible and rich Fourier spectra is desirable when broadband absorption for un-polarized incident light in different angles needs to be optimized. If this is the target, optimized multi-periodic patterns always outperform the periodic ones as they offer more flexibility to shift and balance spatial frequencies that facilitate efficient coupling for both TE and TM modes.

5.5 Conclusion

We have proposed to use free necklace or bracelet problem concept to squeeze the design space for one-dimensional multi-periodic patterns. This applicable approach partially relieved us from vast search space. As such, rigorous electromagnetic calculations can be used to comprehensive study the performance of multi-periodic structures. As an example, a thin film absorber was designed using this method to enhance the absorbance through a broadband spectrum (300 nm – 1100 nm). The results have shown that the optimized multi-periodic pattern, benefitting from engineered rich Fourier spectra, yielded the highest integrated absorption of 42.2%, which is 11.9% higher than that of the optimized mono-periodic pattern. Further, such design concept could be even more efficient for more complex binary patterns. Beyond that, given the efficiency and simplicity of the 'unique' pattern design principle, this method inspires the design and optimization of periodic patterns in different disciplines [96, 111].

Chapter 6

Conclusions and Perspectives

The periodic structures play a significant role in nanotechnology. By making use of the most important attribute of this kind of structures, namely periodicity, tailored fabrication and simulation methods were presented in this dissertation.

6.1 Conclusions

The first part of the thesis was focused on fabrication. A lab-scale and fast-prototyping experimental setup named Laser Interference Lithography (LIL) was introduced. Combining with other techniques such as dry etching, wet etching, and electrochemical etching, different kinds of periodic structures (cylindrical holes, inverted pyramids, porous silicon arrays, etc.) were realized. We highlighted that a highly homogeneous micrometer-deep porous silicon with periodicity as small as 300 nm was fabricated. It represented the state of the art of this kind of porous silicon arrays. Also, a low-cost preconcentration chip was also fabricated by combining LIL and xurography. Despite its limitation in resolution, our device could be attractive for building low-cost biomolecule preconcentration chip.

In the second part, we focused on the optical properties of periodic nanostructures. An electromagnetic simulation method named Rigorous Coupled-Wave Analysis (RCWA) was developed. We have shown the accuracy and efficiency of this tailored method for calculating the optical response of periodic structures. Besides, a novel algorithm to

comprehensively optimize and interpret multi-periodic structures for photon control was proposed. As an example, we combined this algorithm with RCWA method to investigate light trapping in low-absorbing material. It deepened our understanding of adding spatial arrangements of nanostripes in high-performance light trapping layers. Additionally, given the efficiency and simplicity of the 'unique' pattern design principle, this method inspires the design and optimization of periodic patterns in different disciplines.

6.2 Further Research

Several topics could be the subject of further work.

- We have illustrated that the porous silicon array with the period of 300 nm was not the actually limit of this technique. Further reduction of the period and pore diameter would be realized by intensive re-optimization of all process steps. As a starting point, we have shown the fabrication of inverted pyramids with the period of 200 nm in Fig. 2.13a. As such, there is no obstacle to fabricate small inverted pyramids with our current setup and process. The process optimization will be mainly focused on electrochemical etching.

- The RCWA method that we developed was not fully functional. Several improvements could be made to decrease the simulation time and, at the same time, increase the accuracy, such as fast Fourier factorization, sub-pixel averaging, etc. Besides the improvement in the numerical algorithm, efforts could also be conducted to code implementation. By adopting parallel computing, it is envisaged that the calculation efficiency can be further improved [112].

- RCWA is considered intrinsically unsuitable to tackle structured layers with high reflective index (such as metal) or slow varied structure in the z-direction, as the calculation will become very intensive or even inaccurate. To make this method omni-functional, it would be interesting to couple different existing numerical simulation methods (Finite Element Method or Finite Difference Frequency Domain method) with RCWA to improve the functionalities. [113, 114]. A feasible option

could be decomposing a complex structure to different layers and at the same time isolating the layers that can be hard to solve with RCWA. And then RCWA can be used to determine the "normal" layers, and other numerical methods (FEM or FDFD) can be used to solve the "abnormal" layers. Finally, S-matrix can be used to connect different layers to construct a global S-matrix for the whole structure.

- The one-dimensional pattern generation method that we stated in Chapter 5 could be combined with other optimization techniques such as Genetic Algorithm and Particle Swarm Optimization to pre-filter the search space. In a small size searching pool, these traditional optimization methods could be more efficient. In this way, computational intensive electromagnetic methods could be directly used to optimize rigorously the performance of structures without too much considering the calculation time.

- The one-dimensional pattern generation method could also be extended to two-dimensional problems. However considering the complexity of the two-dimensional problems and computational burden, an identical approach is impractical. A realistic way would be extending the one-dimensional pattern to two-dimensional in reciprocal space and then transform it back into real space to form a real two-dimensional lattice. Alternatively, heuristic optimization methods could be used to direction construct two-dimensional lattice in real space to match the desired Fourier coefficient distribution in Fourier space that is built directly according to the Fourier transform of the one-dimensional pattern.

Appendix A

Uniformity Determination

In this Appendix, we show the method that we used to determine the uniformity of the fabricated patterns using SEM images. This approach is based on different functionalities of ImageJ software [45]. Mainly, we use ImageJ to determine the size of the patterns by brightness contrast. Then the sizes of all the patterns in the SEM images can be easily defined, which makes statistical analysis feasible.

During the experiments, we took SEM images throughout all the processes that were needed to be carefully controlled. In our case, they were the LIL, RIE, and KOH etching. As our sample was in centimeter scale, the effect of all the processes might be different in different places. To control the quality of the SEM images, we took pictures for the same sample in approximately the same location with the same resolution. In this way, the statistical analysis of different processes would be reliable.

As an example, we demonstrate the statistical distribution analysis of an image after the RIE process. Figure A.1a shows the tailored original SEM image before defining the sizes of the holes. We can clearly tell the difference between the etched and un-etched silicon slab because of the brightness contrast. This kind of high brightness contrast image is suitable for analysis. Figure A.1b shows the software highlighted brightness contrast image in the binary form. The automatic threshold is used to avoid user-bias [115]. All the holes that are taken into account are demonstrated in Fig. A.1c. As such the area (S) of every hole can be calculated in ImageJ by counting the number of pixels that it contains. Since the shape and edge of the holes are pixelated because of

the quality of the image and the way we determine the contour, we approximate that every hole is perfect round. Then the radius can be calculated by $r = \sqrt{S/\pi}$. Figure A.1d shows the statistically analysis of the image in Fig. A.1a. As we can see, the size distribution approximately agrees with the normal distribution, which implies the reliability of our analysis. Other analyzes are the iteration of this typical process.

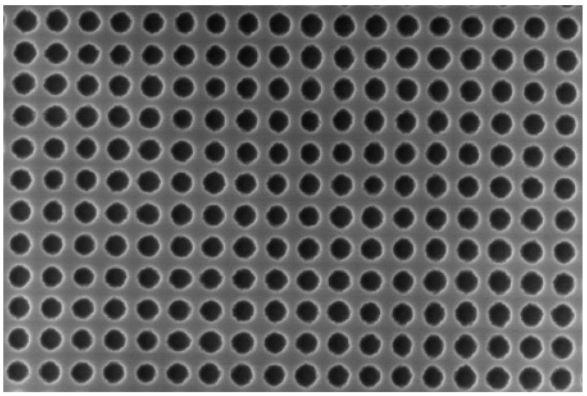

(a) Original SEM image

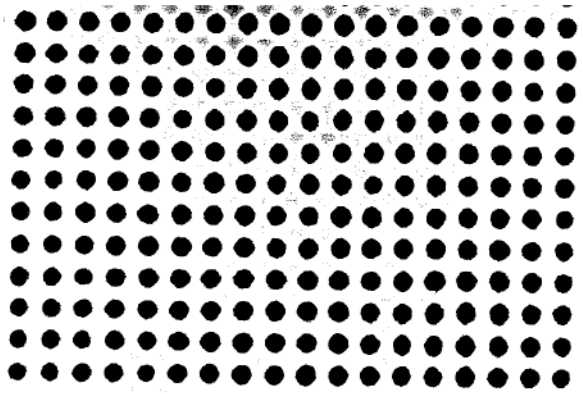

(b) Binary image

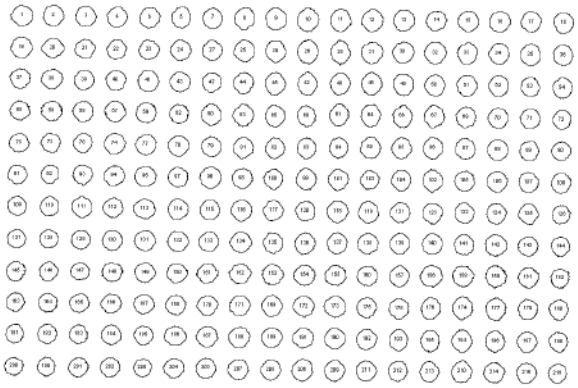

(c) Outline image

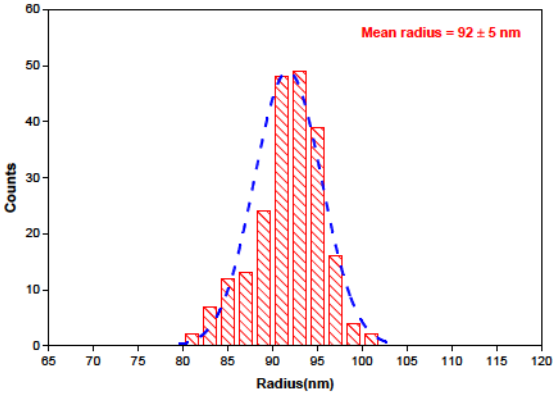

(d) Statistical analysis

Figure A.1: Processed SEM images and statistical result for uniformity analysis.

Appendix B

Convolution Matrix Operator

In this Appendix, we explain the construction of the convolution matrix operator. As in matrix algebra, it is more convenient to deal with matrix multiplication than with convolution. A convolution sum can be expressed as in Eq. B.1.

$$F(m,n) = \sum_{p=-\infty}^{\infty} \sum_{q=-\infty}^{\infty} a_{m-p,n-q} S(p,q) \tag{B.1}$$

In an actual calculation, we use truncated number (M and N) for p and q. For the sake of simplicity, we assume three harmonics p, q = -1,0,1 are used. The constructed two-dimensional matrix operator will be

$$\begin{pmatrix}
a_{0,0} & a_{-1,0} & a_{-2,0} & a_{0,-1} & a_{-1,-1} & a_{-2,-1} & a_{0,-2} & a_{-1,-2} & a_{-2,-2} \\
a_{1,0} & a_{0,0} & a_{-1,0} & a_{1,-1} & a_{0,-1} & a_{-1,-1} & a_{1,-2} & a_{0,-2} & a_{-1,-2} \\
a_{2,0} & a_{1,0} & a_{0,0} & a_{2,-1} & a_{1,-1} & a_{0,-1} & a_{2,-2} & a_{1,-2} & a_{0,-2} \\
a_{0,1} & a_{-1,1} & a_{-2,1} & a_{0,0} & a_{-1,0} & a_{-2,0} & a_{0,-1} & a_{-1,-1} & a_{-2,-1} \\
a_{1,1} & a_{0,1} & a_{-1,1} & a_{1,0} & a_{0,0} & a_{-1,0} & a_{1,-1} & a_{0,-1} & a_{-1,-1} \\
a_{2,1} & a_{1,1} & a_{0,1} & a_{2,0} & a_{1,0} & a_{0,0} & a_{2,-1} & a_{1,-1} & a_{0,-1} \\
a_{0,2} & a_{-1,2} & a_{-2,2} & a_{0,1} & a_{-1,1} & a_{-2,1} & a_{0,0} & a_{-1,0} & a_{-2,0} \\
a_{1,2} & a_{0,2} & a_{-1,2} & a_{1,1} & a_{0,1} & a_{-1,1} & a_{1,0} & a_{0,0} & a_{-1,0} \\
a_{2,2} & a_{1,2} & a_{0,2} & a_{2,1} & a_{1,1} & a_{0,1} & a_{2,0} & a_{1,0} & a_{0,0}
\end{pmatrix} \tag{B.2}$$

The matrix does not have a Toeplitz symmetry; however, we can find 3×3 Toeplitz blocks in the matrix. Furthermore, if we treat the 3×3 matrix as a block, then we can argue that it is a block Toeplitz matrix.

Appendix C

Necklace Problem

The Matlab script that we used to generate the 'necklaces' for the calculations. This Matlab code is capable of generating arbitrary length and beats of necklaces in an efficient way. The generated code sequences are then integrated with our RCWA code to comprehensively optimize the multi-periodic patterns.

```
function X = genPattern(n, k)
% This code is part of program named JSR toolbox
% created by Raphael Jungers.
% The modified version for our calculations.
% Input: n—length of necklace;
% k—different kinds of beats in the necklace
if (nargin == 1)
    k = 2;
end
w = length(n);
X = cell(w, 1);
% Brute-force generation
for cur = 1:w,
    N = n(cur);
    scaler = k.^(N-1:-1:0)';
    % Generate all k-ary N-tuples
```

```
        A = zeros(k^N, N);
        for idx = 1:N,
            w = k^(N-idx);
            for i = 0:(k^idx)-1,
                A(i*w+1:(i+1)*w, idx) = mod(i, k);
            end
        end
        % Remove all non-necklaces
        ok = true(k^N, 1);
        shifter = zeros(N-1, N);
        for i = 1:N-1,
            shifter(i, :) = [(i+1):N, 1:i];
        end
        for scan = 1:k^N,
            if ok(scan),
                base = A(scan, :);
                ok(1+base(shifter)*scaler) = 0;
                ok(scan) = 1;
            end
        end
        X{cur} = A(ok, :);

    end

    if (length(n) == 1)
        X = fliplr(X{1});
    end

    % eliminate all the mirror patterns
    Y = fliplr(X);
```

```
NumCol = numel(X(:,1));
for i = 1:n
    Y_ = circshift(Y,[0 i]);
    for j = 1:NumCol
        for k = j+1:NumCol
            if isequal(Y_(j,:),X(k,:))
                X(j,:) = 0;
            end
        end
    end
end
```

Appendix D

Particle Swarm Optimization

In a typical Particle Swarm Optimization (PSO) process, a set of randomly generated solutions (initial swarm) propagates in the design space and towards the optimal solution over a number of iterations based on a large amount of information about the design space that is assimilated and shared by all members of the swarm.

A basic PSO algorithm consists of three steps, namely, particle generation (positions and velocities), velocity update, and position update. Here, a particle refers to a point in the design space that changes its position from one move (iteration) to another based on velocity update. First, the positions, x_i^k, of the initial swarm of particles are randomly generated using upper and lower bounds on the design variables values, x_{min} and x_{max}, as expressed in Eq. D.1.

$$x_i^k = min\left(x_{max}, max\left(x_{min}, rand\left(x\left(i\right)\right)\right)\right) \tag{D.1}$$

The second step is to update the velocities of all particles at time $k+1$ using the fitness function values that are functions of the particles' current positions in the design space at time k (see Eq. D.2). In our case, the fitness function is the integrated absorption in the interested wavelength (from 300 to 1100 nm).

$$V_{i+1}^{k+1} = wV_i^k + cr_1^k(p_i^k - x_i^k) + sr_2^k(p_g^k - x_i^k) \tag{D.2}$$

- V_i^k is the velocity of the i^{th} particle at the k^{th} iteration

- p_i^k is the best solution observed by current particle (local best)
- p_g^k is the best solution observed by any particles (global best)
- w is the inertia coefficient
- c is the cognitive coefficient
- s is the social coefficient

The first part is the inertia term that controls how quickly a particle will change its direction. The second part is the cognitive term that controls the tendency of a particle to move toward the best solution observed by that particle. The third term is the social term that controls the tendency of a particle to move toward the best solution observed by any of the particles. The three weight factors (w, c and s) define the characteristic of the particles, which affects the convergence of the method. In our case, we found that the setting of the cognitive coefficient (c) and social coefficient (s) at 2.05 and a random number for inertia coefficient at the range from 0.8 to 1.2 provided the fastest convergence.

The last step is position update. The position of each particle is updated using its velocity vector as shown in Eq. D.3.

$$x_i^{k+1} = x_i^k + \chi V_i^{k+1} \tag{D.3}$$

- x_i^k is the position of i^{th} particle at k^{th} iteration
- χ is constriction factor

In our case, the constriction factor was set to be 1. These three steps are repeated for a certain generations or until the desired convergence criterion is met. The pseudo code of the procedure is as follows:

Initialization of particles
for each particle **do**
    Calculate fitness value
    if The fitness value is better than the best fitness value in history **then**

Set current value as the new local best

end if

Choose the particle with the best fitness value of all the particles as the global best

end for

for each particle **do**

Calculate particle velocity according to Eq. D.2

Update particle position according Eq. D.3

end for

After the whole optimization process, the best pattern with the etching depth of 106 nm, period of 311 nm, and the filling factor of 0.502 yielded an integrated absorption of 37.8%. For the sake of simplicity to next step optimization, we fixed the etching depth to 100 nm, period to 300 nm and filling factor to 0.5, which still gave us an integrated absorption of 37.7%. The next step optimization is based on this revised pattern.

Bibliography

[1] J. D. Joannopoulos, S. G. Johnson, J. N. Winn, and R. D. Meade. *Photonic crystals: molding the flow of light*. Princeton university press, 2011 (cit. on p. 1).

[2] B. Ziaie, A. Baldi, and M. Z. Atashbar. "Introduction to Micro/Nanofabrication". In: *Springer Handbook of Nanotechnology*. Vol. 54. Berlin, Heidelberg: Springer Berlin Heidelberg, 2004, pp. 147–184 (cit. on p. 1).

[3] C. Vieu, F. Carcenac, A. Pépin, Y. Chen, M. Mejias, A. Lebib, L. Manin-Ferlazzo, L. Couraud, and H. Launois. "Electron beam lithography: resolution limits and applications". In: *Applied Surface Science* 164.1-4 (Sept. 2000), pp. 111–117 (cit. on p. 1).

[4] L. J. Guo. "Recent progress in nanoimprint technology and its applications". In: *Journal of Physics D: Applied Physics* 37.11 (2004), R123–R141 (cit. on p. 1).

[5] M. Campbell, D. Sharp, M. Harrison, R. Denning, and A. Turberfield. "Fabrication of photonic crystals for the visible spectrum by holographic lithography". In: *Nature* 404.6773 (2000), pp. 53–56 (cit. on p. 2).

[6] M. Farhoud, J. Ferrera, A. J. Lochtefeld, T. E. Murphy, M. L. Schattenburg, J. Carter, C. A. Ross, and H. I. Smith. "Fabrication of 200 nm period nanomagnet arrays using interference lithography and a negative resist". In: *J. Vac. Sci. Technol. B* 17.6 (1999), pp. 3182–3185 (cit. on p. 2).

[7] E. F. Wassermann, M. Thielen, S. Kirsch, A. Pollmann, H. Weinforth, and A. Carl. "Fabrication of large scale periodic magnetic nanostructures". In: *Journal of Applied Physics* 83.3 (1998), p. 1753 (cit. on p. 2).

[8] Y. Wei, W. Wu, R. Guo, D. Yuan, S. Das, and Z. L. Wang. "Wafer-scale high-throughput ordered growth of vertically aligned ZnO nanowire arrays". In: *Nano Letters* 10.9 (2010), pp. 3414–3419 (cit. on p. 2).

[9] M. E. Walsh. "On the design of lithographic interferometers and their application". PhD thesis. Massachusetts Institute of Technology, 2004 (cit. on pp. 2, 5, 10).

[10] D. Xia, Z. Ku, S. C. Lee, and S. R. J. Brueck. "Nanostructures and Functional Materials Fabricated by Interferometric Lithography". In: *Advanced Materials* 23.2 (Jan. 2011), pp. 147–179 (cit. on pp. 2, 26).

[11] C. Lu and R. Lipson. "Interference lithography: a powerful tool for fabricating periodic structures". In: *Laser & Photonics Reviews* 4.4 (2010), pp. 568–580 (cit. on pp. 2, 26).

[12] C. Duan, W. Wang, and Q. Xie. "Review article: Fabrication of nanofluidic devices". In: *Biomicrofluidics* 7.2 (Mar. 2013), p. 026501 (cit. on p. 2).

[13] X. Meng, V. Depauw, G. Gomard, O. El Daif, C. Trompoukis, E. Drouard, C. Jamois, A. Fave, F. Dross, I. Gordon, and C. Seassal. "Design, fabrication and optical characterization of photonic crystal assisted thin film monocrystalline-silicon solar cells". In: *Optics Express* 20.S4 (July 2012), A465 (cit. on p. 2).

[14] A. Mavrokefalos, S. E. Han, S. Yerci, M. S. Branham, and G. Chen. "Efficient Light Trapping in Inverted Nanopyramid Thin Crystalline Silicon Membranes for Solar Cell Applications". In: *Nano Letters* 12.6 (June 2012), pp. 2792–2796 (cit. on p. 2).

[15] J.-H. Seo, J. H. Park, S.-I. Kim, B. J. Park, Z. Ma, J. Choi, and B.-K. Ju. "Nanopatterning by laser interference lithography: applications to optical devices". In: *Journal of nanoscience and nanotechnology* 14.2 (2014), pp. 1521–1532 (cit. on p. 2).

[16] A. Taflove, S. C. Hagness, et al. "Computational electrodynamics: the finite-difference time-domain method". In: *Norwood, 2nd Edition, MA: Artech House, l995* (1995) (cit. on p. 3).

[17] S. D. Gedney. *Introduction to the Finite-Difference Time-Domain (FDTD) Method for Electromagnetics*. Vol. 6. 1. 2011, pp. 1–250 (cit. on p. 3).

[18] J. B. Schneider. "Understanding the Finite-Difference Time-Domain Method". In: *Self Published* (2013) (cit. on p. 3).

[19] A. C. Polycarpou. *Introduction to the finite element method in electromagnetics*. Vol. 1. 2005, pp. 1–126 (cit. on p. 3).

[20] M. G. Moharam and T. K. Gaylord. "Three-dimensional vector coupled-wave analysis of planar-grating diffraction". In: *Journal of the Optical Society of America* 73.9 (Sept. 1983), p. 1105 (cit. on pp. 3, 63).

[21] H. Wolferen, L. Abelmann, and H. van Wolferen. "Laser interference lithography". In: *Lithography: Principles, Processes and Materials* (2011), pp. 133–148 (cit. on p. 10).

[22] I. Byun and J. Kim. "Cost-effective laser interference lithography using a 405 nm AlInGaN semiconductor laser". In: *Journal of Micromechanics and Microengineering* 20.5 (May 2010), p. 055024 (cit. on p. 11).

[23] C. A. Mack. *Field guide to optical lithography*. SPIE Press Bellingham, Washington, USA, 2006 (cit. on p. 16).

[24] R. Legtenberg. "Anisotropic Reactive Ion Etching of Silicon Using $SF_6/O_2/CHF_3$ Gas Mixtures". In: *Journal of The Electrochemical Society* 142.6 (1995), p. 2020 (cit. on p. 18).

[25] V. Lehmann, R. Stengl, and A. Luigart. "On the morphology and the electrochemical formation mechanism of mesoporous silicon". In: *Materials Science and Engineering: B* 69-70 (Jan. 2000), pp. 11–22 (cit. on p. 24).

[26] H. Föll, J. Carstensen, and S. Frey. "Porous and Nanoporous Semiconductors and Emerging Applications". In: *Journal of Nanomaterials* 2006 (2006), pp. 1–10 (cit. on p. 24).

[27] "Attenuation of optical transmission within the band gap of thin two-dimensional macroporous silicon photonic crystals". In: *Applied Physics Letters* 75.20 (1999), p. 3063 (cit. on p. 24).

[28] S. Aravamudhan, A. R. A. Rahman, and S. Bhansali. "Porous silicon based orientation independent, self-priming micro direct ethanol fuel cell". In: *Sensors and Actuators A: Physical* 123-124 (Sept. 2005), pp. 497–504 (cit. on p. 24).

[29] K. Mathwig, F. Müller, and U. Gösele. "Particle transport in asymmetrically modulated pores". In: *New Journal of Physics* 13.3 (Mar. 2011), p. 033038 (cit. on p. 24).

[30] R. van Reis and A. Zydney. "Membrane separations in biotechnology". In: *Current Opinion in Biotechnology* 12.2 (Apr. 2001), pp. 208–211 (cit. on p. 24).

[31] S. Aravamudhan, K. Luongo, P. Poddar, H. Srikanth, and S. Bhansali. "Porous silicon templates for electrodeposition of nanostructures". In: *Applied Physics A* 87.4 (Apr. 2007), pp. 773–780 (cit. on p. 24).

[32] V. Lehmann. "The physics of macroporous silicon formation". In: *Thin Solid Films* 255.1 (1995), pp. 1–4 (cit. on p. 24).

[33] P. Kleimann, J. Linnros, and S. Petersson. "Formation of wide and deep pores in silicon by electrochemical etching". In: *Materials Science and Engineering: B* 69-70 (Jan. 2000), pp. 29–33 (cit. on p. 24).

[34] G. Barillaro, A. Nannini, and M. Piotto. "Electrochemical etching in HF solution for silicon micromachining". In: *Sensors and Actuators A: Physical* 102.1-2 (Dec. 2002), pp. 195–201 (cit. on p. 24).

[35] T. Schmidt, M. Zhang, S. Yu, and J. Linnros. "Fabrication of ultra-high aspect ratio silicon nanopores by electrochemical etching". In: *Applied Physics Letters* 105.12 (Sept. 2014), p. 123111 (cit. on p. 24).

[36] S. Matthias, F. Müller, J. Schilling, and U. Gösele. "Pushing the limits of macroporous silicon etching". In: *Applied Physics A* 80.7 (2005), pp. 1391–1396 (cit. on p. 24).

[37] P. Kleimann, J. Linnros, and R. Juhasz. "Formation of three-dimensional microstructures by electrochemical etching of silicon". In: *Applied Physics Letters* 79.11 (2001), p. 1727 (cit. on p. 24).

[38] P. Kleimann, X. Badel, and J. Linnros. "Toward the formation of three-dimensional nanostructures by electrochemical etching of silicon". In: *Applied Physics Letters* 86.18 (2005), p. 183108 (cit. on pp. 24, 30).

[39] J. Schilling, A. Birner, F. Müller, R. Wehrspohn, R. Hillebrand, U. Gösele, K. Busch, S. John, S. Leonard, and H. van Driel. "Optical characterisation of 2D macroporous silicon photonic crystals with bandgaps around 3.5 and 1.3 μm". In: *Optical Materials* 17.1-2 (June 2001), pp. 7–10 (cit. on p. 24).

[40] G. Laffite, M. Roumanie, C. Gourgon, C. Perret, J. Boussey, and P. Kleimann. "Formation of Submicrometer Pore Arrays by Electrochemical Etching of Silicon and Nanoimprint Lithography". In: *Journal of The Electrochemical Society* 158.1 (2011), p. D10 (cit. on pp. 24, 26, 31).

[41] Y. Zhou, X. Y. Chen, Y. H. Fu, G. Vienne, a. I. Kuznetsov, and B. Luk'yanchuk. "Fabrication of large-area 3D optical fishnet metamaterial by laser interference lithography". In: *Applied Physics Letters* 103.12 (2013), p. 123116 (cit. on p. 26).

[42] G. Gomard, X. Meng, E. Drouard, K. E. Hajjam, E. Gerelli, R. Peretti, A. Fave, R. Orobtchouk, M. Lemiti, and C. Seassal. "Light harvesting by planar photonic crystals in solar cells: the case of amorphous silicon". In: *Journal of Optics* 14.2 (Feb. 2012), p. 024011 (cit. on p. 26).

[43] X. Meng, G. Gomard, O. El Daif, E. Drouard, R. Orobtchouk, A. Kaminski, A. Fave, M. Lemiti, A. Abramov, P. Roca i Cabarrocas, and C. Seassal. "Absorbing photonic crystals for silicon thin-film solar cells: Design, fabrication and experimental investigation". In: *Solar Energy Materials and Solar Cells* 95.SUPPL. 1 (May 2011), S32–S38 (cit. on p. 26).

[44] R. Orobtchouk, A. Koster, D. Pascal, and S. Laval. "Simple technique for fabricating limited coupler gratings by holographic method using standard thick photoresist". In: *Electronics Letters* 31.11 (May 1995), pp. 914–915 (cit. on p. 26).

[45] M. D. Abràmoff, P. J. Magalhães, and S. J. Ram. *Image processing with ImageJ*. 2004 (cit. on pp. 28, 36, 76).

[46] I. Zubel. "Silicon anisotropic etching in alkaline solutions III: On the possibility of spatial structures forming in the course of Si(100) anisotropic etching in KOH and KOH+IPA solutions". In: *Sensors and Actuators A: Physical* 84.1-2 (Aug. 2000), pp. 116–125 (cit. on p. 29).

[47] S. Matthias, F. Muller, R. Hillebrand, J. Schilling, and U. Gosele. "Three-dimensional silicon-based photonic crystals fabricated by electrochemical etching". In: *2004 10th International Workshop on Computational Electronics (IEEE Cat. No.04EX915)*. Vol. 1. IEEE, 2004, pp. 168–170 (cit. on p. 30).

[48] T. Defforge, M. Diatta, D. Valente, F. Tran-Van, and G. Gautier. "Role of Electrolyte Additives during Electrochemical Etching of Macropore Arrays in Low-Doped Silicon". In: *Journal of the Electrochemical Society* 160.4 (Feb. 2013), H247–H251 (cit. on p. 31).

[49] J. Homola. "Present and future of surface plasmon resonance biosensors". In: *Analytical and Bioanalytical Chemistry* 377.3 (Oct. 2003), pp. 528–539 (cit. on p. 32).

[50] Y.-C. Wang, A. L. Stevens, and J. Han. "Million-fold Preconcentration of Proteins and Peptides by Nanofluidic Filter". In: *Analytical Chemistry* 77.14 (July 2005), pp. 4293–4299 (cit. on p. 32).

[51] H. Jeon, H. Lee, K. H. Kang, and G. Lim. "Ion concentration polarization-based continuous separation device using electrical repulsion in the depletion region". In: *Scientific Reports* 3 (Dec. 2013), pp. 1–7 (cit. on p. 32).

[52] B. Jung, R. Bharadwaj, and J. G. Santiago. "On-Chip Millionfold Sample Stacking Using Transient Isotachophoresis". In: *Analytical Chemistry* 78.7 (Apr. 2006), pp. 2319–2327 (cit. on p. 32).

[53] C. M. Han, E. Katilius, and J. G. Santiago. "Increasing hybridization rate and sensitivity of DNA microarrays using isotachophoresis". In: *Lab on a Chip* 14.16 (June 2014), p. 2958 (cit. on p. 32).

[54] S. Song, A. K. Singh, and B. J. Kirby. "Electrophoretic Concentration of Proteins at Laser-Patterned Nanoporous Membranes in Microchips". In: *Analytical Chemistry* 76.15 (Aug. 2004), pp. 4589–4592 (cit. on p. 32).

[55] A. Plecis, R. B. Schoch, and P. Renaud. "Ionic Transport Phenomena in Nanofluidics: Experimental and Theoretical Study of the Exclusion-Enrichment Effect on a Chip". In: *Nano Letters* 5.6 (June 2005), pp. 1147–1155 (cit. on p. 32).

[56] X. Yuan, L. Renaud, M.-C. Audry, and P. Kleimann. "Electrokinetic Biomolecule Preconcentration Using Xurography-Based Micro-Nano-Micro Fluidic Devices". In: *Analytical Chemistry* 87.17 (Sept. 2015), pp. 8695–8701 (cit. on pp. 32, 36).

[57] D. Bartholomeusz, R. Boutte, and J. Andrade. "Xurography: rapid prototyping of microstructures using a cutting plotter". In: *Journal of Microelectromechanical Systems* 14.6 (Dec. 2005), pp. 1364–1374 (cit. on p. 32).

[58] A. LaCroix-Fralish, E. J. Templeton, E. D. Salin, and C. D. Skinner. "A rapid prototyping technique for valves and filters in centrifugal microfluidic devices". In: *Lab on a Chip* 9.21 (2009), p. 3151 (cit. on p. 32).

[59] V. G. Levich and C. W. Tobias. "Physicochemical Hydrodynamics". In: *Journal of The Electrochemical Society* 110.11 (1963), p. 251C (cit. on p. 36).

[60] E. V. Dydek, B. Zaltzman, I. Rubinstein, D. Deng, A. Mani, and M. Z. Bazant. "Overlimiting current in a microchannel". In: *Physical review letters* 107.11 (2011), p. 118301 (cit. on p. 36).

[61] H. Kogelnik. "Coupled Wave Theory for Thick Hologram Gratings". In: *Bell System Technical Journal* 48.9 (Nov. 1969), pp. 2909–2947 (cit. on p. 39).

[62] F. G. Kaspar. "Diffraction by thick, periodically stratified gratings with complex dielectric constant". In: *Journal of the Optical Society of America* 63.1 (Jan. 1973), p. 37 (cit. on p. 39).

[63] M. G. Moharam, D. a. Pommet, E. B. Grann, and T. K. Gaylord. "Stable implementation of the rigorous coupled-wave analysis for surface-relief gratings: enhanced transmittance matrix approach". In: *Journal of the Optical Society of America A* 12.5 (May 1995), p. 1077 (cit. on pp. 40, 48).

[64] D. M. Whittaker and I. S. Culshaw. "Scattering-matrix treatment of patterned multilayer photonic structures". In: *Physical Review B* 60.4 (July 1999), pp. 2610–2618 (cit. on pp. 40, 48).

[65] R. Bräuer and O. Bryngdahl. "Electromagnetic diffraction analysis of two-dimensional gratings". In: *Optics Communications* 100.1-4 (1993), pp. 1–5 (cit. on p. 40).

[66] P. Lalanne. "Improved formulation of the coupled-wave method for two-dimensional gratings". In: *Journal of the Optical Society of America A* 14.7 (1997), p. 1592 (cit. on p. 40).

[67] R. C. Rumpf. "Improved formulation of scattering matrices for semi-analytical methods that is consistent with convention". In: *Progress In Electromagnetics Research B* 35.August (2011), pp. 241–261 (cit. on pp. 40, 50).

[68] V. Liu and S. Fan. "S4 : A free electromagnetic solver for layered periodic structures". In: *Computer Physics Communications* 183.10 (Oct. 2012), pp. 2233–2244 (cit. on p. 40).

[69] L. Li and C. W. Haggans. "Convergence of the coupled-wave method for metallic lamellar diffraction gratings". In: *Journal of the Optical Society of America A* 10.6 (1993), p. 1184 (cit. on p. 41).

[70] P. Lalanne and G. M. Morris. "Highly improved convergence of the coupled-wave method for TM polarization". In: *J. Opt. Soc. Am. A* 13.4 (1996), pp. 779–784 (cit. on pp. 41, 63).

[71] L. Li. "Use of Fourier series in the analysis of discontinuous periodic structures". In: *Journal of the Optical Society of America A* 13.9 (Sept. 1996), p. 1870 (cit. on p. 41).

[72] E. Popov and M. Nevière. "Grating theory: new equations in Fourier space leading to fast converging results for TM polarization". In: *Journal of the Optical Society of America A* 17.10 (2000), p. 1773 (cit. on p. 41).

[73] B. Chernov, M. Nevière, and E. Popov. "Fast Fourier factorization method applied to modal analysis of slanted lamellar diffraction gratings in conical mountings". In: *Optics Communications* 194.4-6 (July 2001), pp. 289–297 (cit. on p. 41).

[74] E. Popov and M. Nevière. "Maxwell equations in Fourier space: fast-converging formulation for diffraction by arbitrary shaped, periodic, anisotropic media". In: *Journal of the Optical Society of America A* 18.11 (2001), p. 2886 (cit. on p. 41).

[75] H. Taniyama and M. Notomi. "S-matrix calculation of radiation characteristics from dipole oscillation in two-dimensional photonic crystal slabs". In: *Journal of Applied Physics* 103.8 (2008), p. 083115 (cit. on p. 48).

[76] J. Tervo, M. Kuittinen, P. Vahimaa, J. Turunen, T. Aalto, P. Heimala, and M. Leppihalme. "Efficient Bragg waveguide-grating analysis by quasi-rigorous approach based on Redheffer's star product". In: *Optics Communications* 198.4-6 (Nov. 2001), pp. 265–272 (cit. on p. 50).

[77] S. Fan and J. D. Joannopoulos. "Analysis of guided resonances in photonic crystal slabs". In: *Physical Review B* 65.23 (2002), p. 235112 (cit. on p. 54).

[78] A. F. Oskooi, D. Roundy, M. Ibanescu, P. Bermel, J. D. Joannopoulos, and S. G. Johnson. "Meep: A flexible free-software package for electromagnetic simulations by the FDTD method". In: *Computer Physics Communications* 181.3 (2010), pp. 687–702 (cit. on p. 57).

[79] A. Chutinan, M. Okano, and S. Noda. "Wider bandwidth with high transmission through waveguide bends in two-dimensional photonic crystal slabs". In: *Applied Physics Letters* 80.10 (2002), p. 1698 (cit. on p. 59).

[80] A. Yariv, Y. Xu, R. K. Lee, and A. Scherer. "Coupled-resonator optical waveguide: a proposal and analysis". In: *Optics Letters* 24.11 (June 1999), p. 711 (cit. on p. 59).

[81] A. David, H. Benisty, and C. Weisbuch. "Photonic crystal light-emitting sources". In: *Reports on Progress in Physics* 75.12 (Dec. 2012), p. 126501 (cit. on p. 59).

[82] Q. Yu, P. Guan, D. Qin, G. Golden, and P. M. Wallace. "Inverted Size-Dependence of Surface-Enhanced Raman Scattering on Gold Nanohole and Nanodisk Arrays". In: *Nano Letters* 8.7 (July 2008), pp. 1923–1928 (cit. on p. 59).

[83] P. Kowalczewski, M. Liscidini, and L. C. Andreani. "Engineering Gaussian disorder at rough interfaces for light trapping in thin-film solar cells". In: *Optics Letters* 37.23 (Dec. 2012), p. 4868 (cit. on p. 59).

[84] V. Ganapati, O. D. Miller, and E. Yablonovitch. "Light trapping textures designed by electromagnetic optimization for subwavelength thick solar cells". In: *Photovoltaics, IEEE Journal of* 4.1 (2014), pp. 175–182 (cit. on p. 59).

[85] K. Jäger, M. Fischer, R. A. van Swaaij, and M. Zeman. "Designing optimized nano textures for thin-film silicon solar cells". In: *Optics Express* 21.S4 (July 2013), A656–A668 (cit. on p. 59).

[86] Z. Vardeny, A. Nahata, and A. Agrawal. "Optics of photonic quasicrystals". In: *Nature Photonics* 7.3 (Feb. 2013), pp. 177–187 (cit. on p. 59).

[87] S. Golmohammadi, M. K. Moravvej-Farshi, A. Rostami, and A. Zarifkar. "Narrowband DWDM filters based on Fibonacci-class quasi-periodic structures". In: *Optics Express* 15.17 (2007), pp. 10520–10532 (cit. on p. 59).

[88] J. Xavier, J. Probst, F. Back, P. Wyss, D. Eisenhauer, B. Löchel, E. Rudigier-Voigt, and C. Becker. "Quasicrystalline-structured light harvesting nanophotonic silicon films on nanoimprinted glass for ultra-thin photovoltaics". In: *Optical Materials Express* 4.11 (Nov. 2014), pp. 2290–2299 (cit. on p. 59).

[89] S. Kasture, A. P. Ravishankar, V. J. Yallapragada, R. Patil, N. V. Valappil, G. Mulay, and V. G. Achanta. "Plasmonic quasicrystals with broadband transmission enhancement". In: *Scientific Reports* 4 (June 2014), p. 5257 (cit. on p. 59).

[90] S. V. Boriskina. "Quasicrystals: Making invisible materials". In: *Nature Photonics* 9.7 (June 2015), pp. 422–424 (cit. on p. 59).

[91] K. Vynck, M. Burresi, F. Riboli, and D. S. Wiersma. "Photon management in two-dimensional disordered media". In: *Nature materials* 11.12 (2012), pp. 1017–1022 (cit. on p. 59).

[92] F. Priolo, T. Gregorkiewicz, M. Galli, and T. F. Krauss. "Silicon nanostructures for photonics and photovoltaics". In: *Nature nanotechnology* 9.1 (2014), pp. 19–32 (cit. on p. 59).

[93] A. Oskooi, P. A. Favuzzi, Y. Tanaka, H. Shigeta, Y. Kawakami, and S. Noda. "Partially disordered photonic-crystal thin films for enhanced and robust photovoltaics". In: *Applied Physics Letters* 100.18 (2012), p. 181110 (cit. on p. 59).

[94] R. Peretti, G. Gomard, L. Lalouat, C. Seassal, and E. Drouard. "Absorption control in pseudodisordered photonic-crystal thin films". In: *Physical Review A* 88.5 (Nov. 2013), p. 053835 (cit. on pp. 59, 69).

[95] M.-C. van Lare and A. Polman. "Optimized Scattering Power Spectral Density of Photovoltaic Light-Trapping Patterns". In: *ACS Photonics* 2.7 (July 2015), pp. 822–831 (cit. on pp. 59, 67).

[96] C. Kluge, J. Adam, N. Barié, P.-J. Jakobs, M. Guttmann, and M. Gerken. "Multiperiodic nanostructures for photon control". In: *Optics Express* 22.S5 (Aug. 2014), A1363 (cit. on pp. 59, 72).

[97] A. Gopinath, S. V. Boriskina, B. M. Reinhard, and L. Dal Negro. "Deterministic aperiodic arrays of metal nanoparticles for surface-enhanced Raman scattering (SERS)". In: *Optics Express* 17.5 (Mar. 2009), p. 3741 (cit. on p. 59).

[98] S. Kocaman, M. S. Aras, P. Hsieh, J. F. McMillan, C. G. Biris, N. C. Panoiu, M. B. Yu, D. L. Kwong, A. Stein, and C. W. Wong. "Zero phase delay in negative-refractive-index photonic crystal superlattices". In: *Nature Photonics* 5.8 (July 2011), pp. 499–505 (cit. on p. 59).

[99] Y. K. Zhong, S. M. Fu, N. P. Ju, P. Y. Chen, and A. Lin. "Experimentally-implemented genetic algorithm (Exp-GA): toward fully optimal photovoltaics". In: *Optics Express* 23.19 (Sept. 2015), A1324 (cit. on p. 59).

[100] A. Lin and J. Phillips. "Optimization of random diffraction gratings in thin-film solar cells using genetic algorithms". In: *Solar Energy Materials and Solar Cells* 92.12 (Dec. 2008), pp. 1689–1696 (cit. on p. 59).

[101] L. Shen, Z. Ye, and S. He. "Design of two-dimensional photonic crystals with large absolute band gaps using a genetic algorithm". In: *Physical Review B* 68.3 (July 2003), p. 035109 (cit. on p. 59).

[102] C. Forestiere, M. Donelli, G. F. Walsh, E. Zeni, G. Miano, L. Dal Negro, and L. D. Negro. "Particle-swarm optimization of broadband nanoplasmonic arrays." In: *Optics Letters* 35.2 (Jan. 2010), pp. 133–135 (cit. on p. 59).

[103] A. Bozzola, M. Liscidini, and L. C. Andreani. "Broadband light trapping with disordered photonic structures in thin-film silicon solar cells". In: *Progress in Photovoltaics: Research and Applications* 20.12 (May 2013), pp. 1237–1245 (cit. on pp. 59, 67, 69).

[104] J. Sawada. "A Fast Algorithm to Generate Necklaces With Fixed Content". In: *Theoretical Computer Science* 301.1-3 (May 2003), pp. 477–489 (cit. on pp. 59, 61).

[105] OEIS Foundation Inc. "The On-Line Encyclopedia of Integer Sequences". In: (2011) (cit. on p. 62).

[106] J. Kennedy and R. Eberhart. "Particle swarm optimization". In: *Proceedings of ICNN'95 - International Conference on Neural Networks*. Vol. 4. IEEE, 1995, pp. 1942–1948 (cit. on p. 63).

[107] L. C. Andreani, A. Bozzola, P. Kowalczewski, and M. Liscidini. "Photonic light trapping and electrical transport in thin-film silicon solar cells". In: *Solar Energy Materials and Solar Cells* 135 (Apr. 2015), pp. 78–92 (cit. on pp. 66, 67).

[108] E. R. Martins, J. Li, Y. Liu, J. Zhou, and T. F. Krauss. "Engineering gratings for light trapping in photovoltaics: The supercell concept". In: *Physical Review B* 86.4 (2012), p. 041404 (cit. on p. 67).

[109] E. R. Martins, J. Li, Y. Liu, V. Depauw, Z. Chen, J. Zhou, and T. F. Krauss. "Deterministic quasi-random nanostructures for photon control". In: *Nature Communications* 4 (Oct. 2013), p. 2665 (cit. on pp. 67, 69).

[110] M. Burresi, F. Pratesi, K. Vynck, M. Prasciolu, M. Tormen, and D. S. Wiersma. "Two-dimensional disorder for broadband, omnidirectional and polarization-insensitive absorption". In: *Optics express* 21.102 (2013), A268–A275 (cit. on p. 70).

[111] C. Della Giovampaola and N. Engheta. "Digital metamaterials". In: *Nature materials* 13.12 (2014), pp. 1115–1121 (cit. on p. 72).

[112] J. Tong and S. Chen. "Computation improvement for the rigorous coupled-wave analysis with GPU". In: *Computational and Information Sciences (ICCIS), 2012 Fourth International Conference on*. IEEE. 2012, pp. 123–126 (cit. on p. 74).

[113] M. Kuloglu and R. Lee. "A hybrid finite element/rigorous coupled wave analysis for electromagnetic scattering from periodic structures". In: *Antennas and Propagation Society International Symposium, 2009. APSURSI'09. IEEE*. IEEE. 2009, pp. 1–4 (cit. on p. 74).

[114] F. Wang and R. Lee. "Fast hybrid method for modeling scattering from doubly periodic dielectric structure in 3-d". In: *Antennas and Propagation (APSURSI), 2011 IEEE International Symposium on*. IEEE. 2011, pp. 331–334 (cit. on p. 74).

[115] M. Sezgin et al. "Survey over image thresholding techniques and quantitative performance evaluation". In: *Journal of Electronic imaging* 13.1 (2004), pp. 146–168 (cit. on p. 76).

Publication list

Journals

- J. Liu, P. Kleimann, G. Laffite, C. Jamois, and R. Orobtchouk, "Formation of 300 nm period pore arrays by laser interference lithography and electrochemical etching", Applied Physics Letters (2015).

- J. Liu, L. Lalouat, E. Drouard, and R. Orobtchouk, "Binary coded patterns for photon control using necklace problem concept", Opt. Express (2016).

- C. Trompoukis, I. Abdo, R. Cariou, J. Liu, etc., "Photonic nanostructures for advanced light trapping in thin crystalline silicon solar cells", Physica Status Solidi A (2015).

- W. Chen, R. Cariou, J. Liu, etc., "Nanophotonics-based low temperature PECVD epitaxial crystalline silicon solar cells", Journal of Physics D, (2016).

Conferences

- J. Liu, Régis Orobtchouk, etc., "Simulations Optiques et Fabrication de Nanostructures Périodiques pour la Microfluidique et le Photovoltaïque", Journées Nationales du Réseau Doctoral en Micro-nanoélectronique, Bordeaux, France, 2015 (poster).

- J. Liu, E. Drouard, L. Lalouat, and R. Orobtchouk, "Light Trapping in Thin Film Silicon with Pseudo-disordered Binary Structure", GDR Ondes, Lyon, France, 2015 (poster).

- H. Ding, J. Liu, etc., "Light trapping in holes or pyramid patterns for thin film solar cells", Photovoltaic Technical Conference, Aix-en-Provence, France, 2014 (poster).

- V. Depauw, I. Abdo, R. Boukhicha, J. Liu, etc., "Nanophotonics for ultra-thin crystalline silicon photovoltaics: when photons (actually) meet electrons", EUPVSEC, 2014 (presentation).